UiT
THE ARCTIC
UNIVERSITY
OF NORWAY

Faculty of Science and Technology
Department of Physics and Technology

Optical nanoscopy of tissue sections

—

Luis VILLEGAS

FYS-3900 Master's thesis in physics 60 SP

May 2018

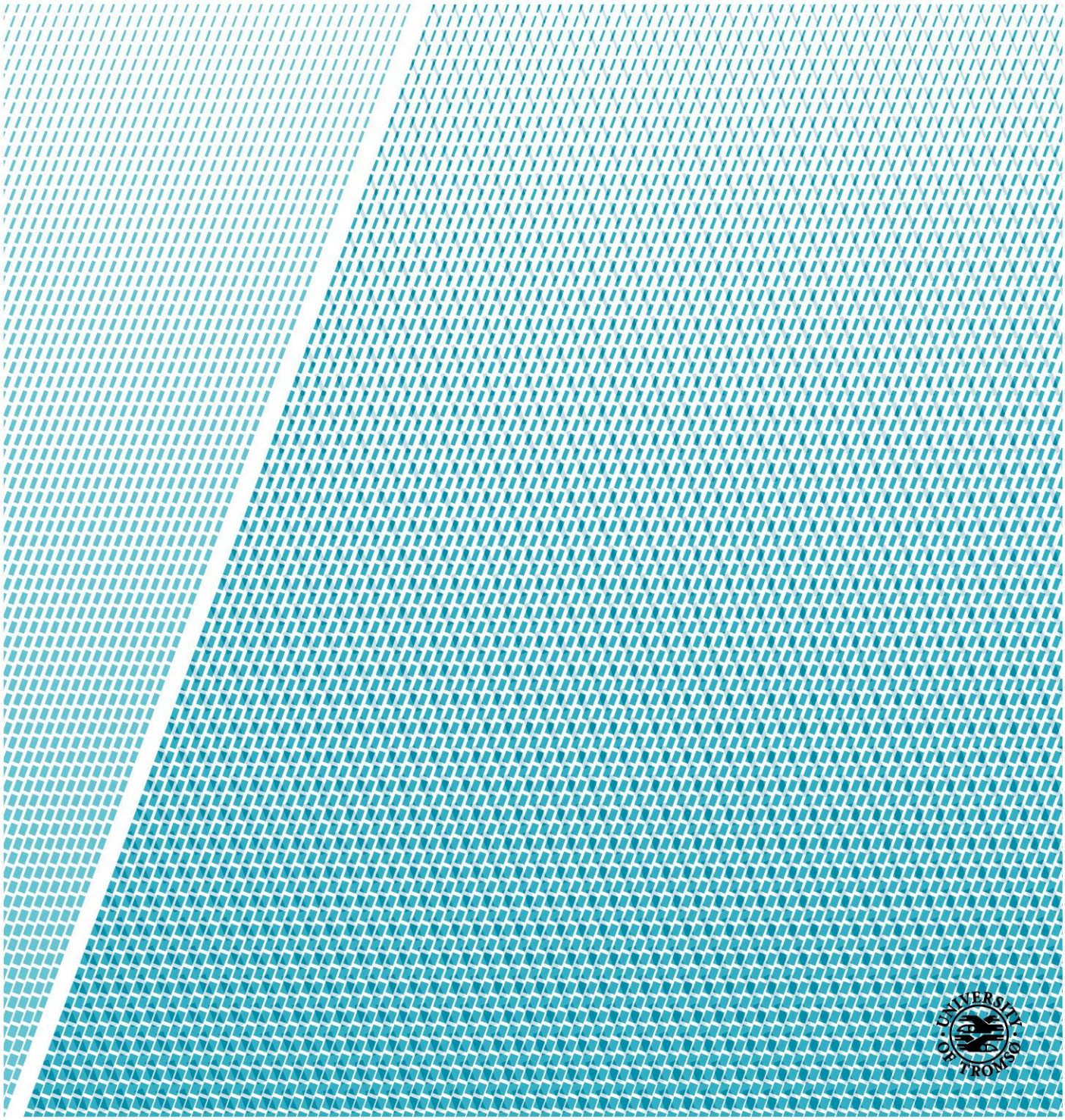

Abstract

The study of organ tissues, namely, histology, is essential for clinical medicine, as it allows the identification of a wide range of diseases. Traditionally, two major techniques, optical and electron microscopy, have been used for morphological observation of tissue sections. Optical microscopy (OM) allows for fast-acquisition high-throughput imaging, at the expense of diffraction-limited resolution (~200nm), whereas electron microscopy (EM) provides with sub-diffraction resolution at low throughput. Routine histological studies require visualization of large field-of-view (FOV) at high throughput. Pathologies such as nephrotic syndrome, brain neoplasms, neuromuscular disorders, to name just a few, require sub-diffraction resolution, placing EM as the primary technique for its clinical diagnose.

In recent years, a new discipline of super-resolution microscopy (SRM), also referred to as optical nanoscopy, has emerged, which achieves sub-diffraction resolution at a faster throughput than EM, allowing for visualization of biological processes at nanoscopic scale. To date, benefits of SRM have been exploited mainly on cellular studies, yet they remain practically unexplored for histological analysis. This master project aimed to image, for the first time, histological samples using two super-resolution optical systems at the UiT – The Arctic University of Norway, namely, the commercial OMX microscope, and the waveguide chip-based microscope setup.

Formalin-fixed paraffin-embedded (FFPE) and cryo-preserved tissue sections from human and non-human origin were fluorescently labeled and imaged on the OMX using super-resolution structure illumination microscopy (SIM) and diffraction-limited deconvolution microscopy (DV). Similarly, histological samples were imaged on the waveguide chip-based microscope setup using diffraction-limited total internal reflection fluorescent (TIRF) microscopy. Furthermore, a correlative light-light microscopy has been performed, to compare the three previously mentioned microscopy techniques.

SIM images of ultra-thin cryo-sections proved the ability of this technique to resolve structures within 120nm distance and exhibited better contrast than diffraction-limited DV images, allowing for visualization of sub-cellular structures present in the tissue. Contrarily, SIM images of FFPE sections led to reconstruction artifacts due to tissue autofluorescence, impairing the sub-diffraction resolution, yet allowing for better contrast enhancement as compared to the DV images. The results from the waveguide chip-based setup validated the feasibility of this platform for TIRF imaging of tissue sections and demonstrated the ability of this technique for high-throughput large-FOV imaging. Notably, the waveguide chip proved to be an optimal substrate for imaging cryo-sections on the OMX, providing a flat reflective-surface that allowed in-focus tile mosaic images and observation of subcellular features that were otherwise not discernible using coverslips or glass slides as substrates.

The findings of this study open a pioneering research path for the implementation of SIM in clinical studies that were traditionally governed by costly low-throughput techniques such as EM. Importantly, the results from the waveguide chip-based microscope obtained in this study set the foundations for further development of a high-throughput super-resolution imaging platform for routine diagnosis of histological sections.

Introduction

> *"Under the pathologist's microscope, life and death fight in an illuminated circle in a sort of cellular bullfight. The pathologist's job is to find the bull among the matador cells"*
>
> *Yann Martel*

With the invention of the optical microscope in the 17th century, many of the minute structures that exist in nature became observable to us. The study of microscopic organisms such as cells and bacteria has led to significant improvements in medical diagnoses and treatments. However, there is a diffraction limit [1] to which optical microscopes can resolve. For a modern optical microscope, using a state of the art oil immersion objective lens at short wavelengths, this limit is around 200 nm [2]. Yet there are multiple features and events of interest occurring at a smaller scale range in all living beings.

In the field of medicine, pathologists utilize the microscope to observe small sections of the body, known as tissues, in search for morphological anomalies associated with certain diseases. Some pathologies can be observed in a diffraction-limited optical microscope, whereas other require sub-diffraction limit capabilities. Over the past five decades, electron microscopy (EM) has served as the main tool for pathological diagnosis in the nanometer scale, despite its numerous disadvantages such as extensive sample preparation, expensive tools and equipment, and low imaging throughput.

From the 90's, a new set of sub-diffraction limit microscopy techniques emerged, under the name of optical nanoscopy, or super-resolution microscopy (SRM). These include structured illumination microscopy (SIM), stimulated emission depletion microscopy (STED) and single molecule localization microscopy (SMLM). Even though SRM shows significant improvements as compared to EM in terms of cost reduction, easiness of sample preparation, and higher image throughput, it remains practically unexplored in tissue studies. Two reasons can be attributed to this fact: the cost of tools and equipment continues to be inaccessible for most pathologists around the world, and the image throughput continues to be insufficient to obtain the large field of view (FOV) required for screening tissues in a regular basis.

The Optics Group at UiT - The Arctic University of Norway, in collaboration with, among others, the Medical Faculty and The University Hospital of North Norway (UNN), is actively exploring the application of optical nanoscopy techniques for super-resolution imaging of biological studies. Two main research lines are currently being carried out. The first one focuses on the application side of SRM and employs a commercial microscope, namely, the Deltavision OMX (GE Healthcare), capable of SIM and SMLM. The second one focuses on the development of waveguide chip-based optical nanoscopy that aims both to reduce the cost and improve the imaging throughput, facilitating researchers to access sub-diffraction resolution in places where other SRM techniques haven't reached so far.

Prior to the start of this master project, all the SRM studies performed by the Optics Group at the UiT were focused primarily on cellular studies [3-6], but none on tissues. Due to increased interest to perform SRM on tissues, it was decided to start up a research line on this topic. The master project consisted of two phases: 1) exploring and

adjusting the imaging parameters for both diffraction-limited and super-resolution imaging of tissue sections on a commercial equipment, in this case the OMX; and 2) diffraction-limited imaging of tissue sections on the waveguide chip-based microscopy setup. The main emphasis of the master project was on using the commercial equipment OMX, totaling approximately 75% of the research time, whereas the remaining 25% was employed on the chip-based setup (Figure 1). Three types of tissues both from human and non-human origin - liver, placenta and heart- were chosen for the study. The choice of samples was based on existing collaborations with the medical biologist group at UiT. Moreover, the observed samples came from one of the two most commonly used preservation techniques, namely Formalin-Fixed Paraffin-Embedding preservation (FFPE), or cryo-preservation.

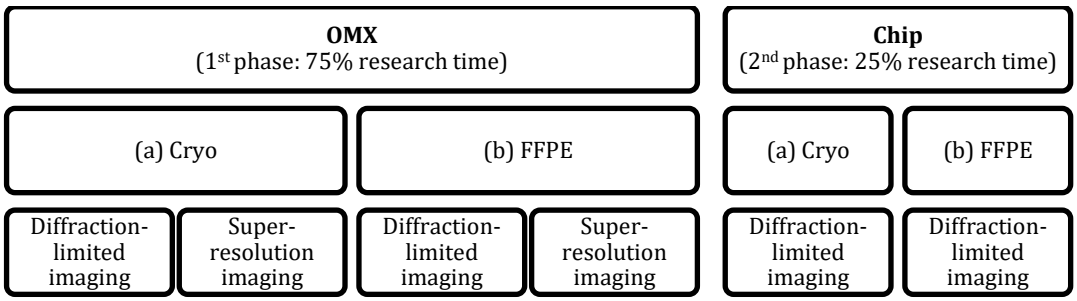

Figure 1. Experimental plan. Flowchart of the two phases of the master project.

To the best of our knowledge, no references of SRM imaging of liver or placental tissues were available in the literature. Hence, the initial effort of this master project was focused in adapting and optimizing the sample preparation protocols from existing techniques - such as confocal and EM microscopy. The results from the OMX show enhancement of contrast and resolution in SIM mode as compared to diffraction-limited microscopy, although some relevant aspects of tissue imaging were observed on this system. FFPE samples exhibited autofluorescence signal as well as imaging artifacts, and the thin cryo-preserved samples represented an imaging challenge, as they frequently became out-of-focus during the scanning acquisition necessary for large FOV imaging.

Results of the chip-based system show the viability of imaging tissues on this platform, both in diffraction-limited mode and SRM. Here, the light propagation in the platform can be compromised by the sample preparation method, which might influence the image quality of the examined tissues. Towards the end of the experimental phase of this project, it was found that using the chip instead of a cover slip as a substrate could bring excellent benefits for tissue imaging on the OMX, as its surface flatness allows for a uniform focal plane during the scanning acquisition of large FOV's.

The preliminary findings of this master project have laid the foundations for collaborations between research groups as in the field of embryology, for detection of pre-eclampsia-related proteins in placental tissues, and in the field of cardiology, for co-localization of autophagy-associated proteins in cardiac muscle tissue. The results from such studies will be shared with the scientific community in specialized conferences across 2018 and 2019. Moreover, two journal papers on a) imaging of tissues using optical waveguide platform and b) tissue imaging using OMX are under preparation.

This document aims to report all the relevant information and knowledge acquired during the master project. The first section defines biological concepts and explains the theoretical framework behind super-resolution fluorescent microscopy used in the first phase of the study, as well as an introduction to the waveguide chip-based microscopy technique used in the second phase. The second section details the materials and methods employed during the project, and the third section illustrates and discusses the results. The last section offers the conclusions and future perspectives of the SRM of tissues.

Acknowledgments

I am very grateful to all the people who supported me during this master project, in particular to my supervisors Dr. Cristina Ionica Øie, Prof. Balpreet Singh Ahluwalia and Dr. Jean-Claude Tinguely, for all the advices and the theoretical-practical knowledge they taught me.

I would like to thank my colleagues at the Optics Group in the UiT, who always shared useful tips with me and generously helped me.

My gratitude also goes to our collaborators from the Medical Biology, Clinical Medicine and UNN, both technicians and researchers, who allowed me to understand the biological relevance of my work and motivated me to go further in my research.

Last but not least, I am thankful to my wife, who encouraged me to follow the academic path, which has become a source of inspiration and joy.

Contents

Abbreviations

Ab	Antibody
AF-488	Alexa Fluor 488
AF-647	Alexa Fluor 647
Approx.	Approximately
BSA	Bovine serum albumin
CMO	Cell mask orange
DV	Deconvolution microscopy
ECM	Extracellular matrix (or intercellular matrix)
EM	Electron microscopy
FFPE	Formalin-fixed paraffin-embedding
FOV	Field of view
FWHM	Full width half maximum
HE	Hematoxylin and eosin staining
IHC	Immunohistochemistry
LSEC	Liver sinusoidal endothelial cell
MMI	Multi-mode interference
N/A	Not applicable
NA	Numerical aperture
OCT	Optimal cutting temperature
PBS	Phosphate buffered saline
PSF	Point spread function
RBC	Red blood cell
RI	Refractive index
RT	Room temperature
SIM	Structured illumination microscopy
SRM	Super-resolution microscopy (or super-resolution microscope)
TIR	Total internal reflection
TIRF	Total internal reflection fluorescence
UiT	The Arctic University of Norway
UNN	The University Hospital of North Norway

Nomenclature

Hz	Hertz (cycles per second)
h	hour
min	minute
s	second
ms	millisecond
µm	micrometer
nm	nanometer
mm2	squared millimeter
cm2	squared centimeter
rpm	revolution per minute
n	refractive index
g	gram
W	watt
mW	milliwatt

List of figures

List of tables

Chapter 1. Theoretical framework

This master project is framed within the field of histology and super-resolution microscopy. The goal of the study was to image, for the first time, histological samples in two optical systems available at Faculty of Physics and Technology at the UiT, namely, the OMX microscope and the prototype waveguide chip-based microscope. This work can be seen as an initial step towards a long-term objective of developing a waveguide chip-based microscopy technique capable of high-throughput SRM for routine diagnostics.

This section, divided in three parts, provides a theoretical introduction of concepts associated with super-resolution imaging of organ tissues. The first part explains general concepts of microscopy. The second part offers an overview of various SRM techniques, including UiT's waveguide chip-based microscopy. Finally, the third part presents details of biological terms and processing techniques related to the field in which this study was conducted.

1.1 Optical microscopy

Optical microscopy is the field of science that uses visible light and a lens system to observe objects of interest whose dimensions are too small to be seen otherwise with our bare eyes. Microscopes must fulfill two requirements: a) the object of study (e.g. biological specimen) must be visually enlarged above the resolving capability of the eye, namely 150μm [7]; and b) the enlarged image must be clear enough so that it can be interpreted and analyzed. These two parameters are defined as magnification and resolution, respectively.

1.1.1 Magnification

The magnification is a ratio that indicates how many times the apparent size of an object is being increased. It is called the 'apparent' size because what is in fact enlarged is not the physical dimensions of the structure itself, but its visual projection.

The magnification is obtained using a combination of optical lenses, each one having its own magnification value. The total magnification of an object seen through a microscope results from the multiplication of the various magnification values of its lenses. In a microscope, the total magnification M is typically given by the equation (1), where M_o and M_e are the magnifications of the objective lens and the eyepiece, respectively.

$$M = M_o \times M_e \tag{1}$$

1.1.2 Diffraction of light and optical resolution

The *resolution* is a parameter that indicates how much detail can be obtained out of an optical system. In other words, it is the minimum distance between two adjacent points at which they can still be distinguished as individual entities rather than a single-merged point. In all optical systems, including microscopes, the resolution is intrinsically dependent on the way light propagates and interacts with its elements, due to a phenomenon called *diffraction of light*.

To illustrate these two concepts, let's first consider an infinitesimally small light source (Figure 1.1). Light propagates in spherical wave fronts containing coherent point sources called wavelets [8]. When the light meets an obstacle such as an aperture, only a few wavelets from the wave front are allowed through. These wavelets behave like individual point sources, emitting light at a synchronous pace. Due to constructive and destructive interference of light, a pattern in form of dark and bright zones emerges after the aperture. In the three-dimensional space, the spot where most of the constructive interference occurs has an elongated shape that differs from the actual shape of the infinitesimally small light source. This diffraction pattern is known as the point spread function (PSF), and its projection in a plane orthogonal to the direction of the light propagation is known as Airy pattern (Figure 1.2, a).

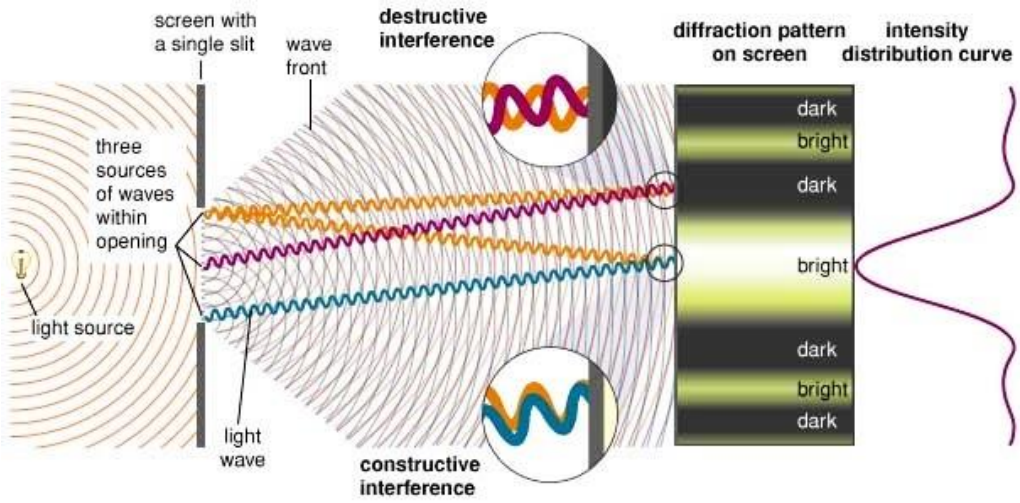

Figure 1.1 Constructive and destructive interference produced by diffraction of light [9].

To further explain the concept of resolution, let us now consider two adjacent emitting sources. If the distance between the two sources is greater than the resolution limit of the optical system, they can be distinguished as individual sources (Figure 1.2, b). However, when the distance decreases, the overlap of the two Airy disks makes it difficult to discern the two sources as individual entities (Figure 1.2, c).

In a microscope, the size of the diffraction pattern is related to the wavelength of light (λ) and the numerical aperture (NA) of the objective lens. There are two main criteria using these parameters to define the resolution limit of an optical microscope, namely, the Rayleigh criterion and the Abbe criterion. The difference between them is based on the definition that both Abbe and Rayleigh used in their derivation for what is meant by two objects being resolvable from each other. In practical terms, this difference is small. The Rayleigh criterion stablishes that the resolution limit (R_R) of an optical microscope as the distance between two emitters when the maximum of one Airy disk overlaps with the first minimum of the second [10]. Mathematically, it is expressed as in equation (2):

$$R_R = \frac{1.22\lambda}{2NA} \tag{2}$$

On the other hand, the Abbe criterion expresses the resolution limit (R_A) per the equation (3) [11]:

$$R_A = \frac{\lambda}{2NA} \tag{3}$$

In summary, the diffraction is a phenomenon present in all optical systems, which limits their resolution. Such optical systems are called *diffraction-limited*. For example, when imaging with green light ($\lambda = 550nm$) with a high NA objective lens ($NA \sim 1.4$), the resolution limit according to Abbe's criterion becomes approximately 200 nm.

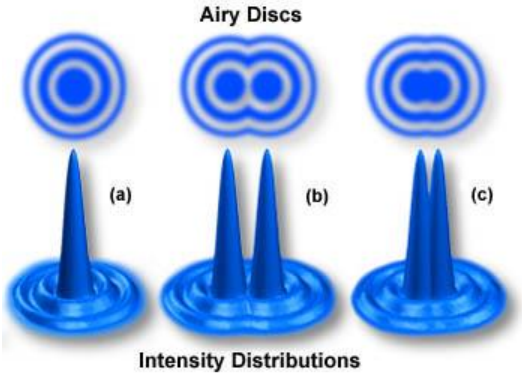

Figure 1.2. Diffraction limit and resolution. a) Airy pattern and intensity distribution curve of a point source emitter. b) two emitting sources separated by a resolvable distance. c) two emitting sources not individually resolvable [12].

1.1.3 Field of view

The field of view (FOV) number, is the diameter of the image field of an optical light microscope measured at the intermediate image plane. The general expression for the FOV is given by the equation (4), where FN is the field number, typically specified as the diaphragm size (in mm) of the microscope's eyepiece, and M_o and M_{aux} are the magnifications of the objective lens and the auxiliary lens (if any), respectively.

$$FoV = \frac{FN}{M_o \times M_{aux}} \tag{4}$$

Hence, by using a higher magnification objective lens, the microscope's field of view becomes smaller. This fact has an important implication in the imaging throughput of histological studies in SRM, as the high NA required for resolution improvement is usually available on high magnification objective lenses only. In modern microscopes, where a camera is used for imaging, the FOV is ultimately limited by the sensor size and it is commonly specified in rectangular dimensions (height and width) in millimeters. However, the idea of equation (4) still holds, meaning that higher magnification results in a smaller FOV.

1.1.4 Contrast

Contrast is an essential factor for the human vision. Our eyes perceive an object by the contrast generated in its image. Mathematically, the contrast (C) is defined as the difference in light intensity between the specimen (I_s) and the adjacent background (I_b) relative to the overall background intensity, as shown in equation (5).

$$C(\%) = \frac{I_s - I_b}{I_b} \times 100 \tag{5}$$

In general, the human eye requires a contrast value of a least two percent (2%) to distinguish differences between the image and its background [13]. Contrast is not an inherent property of the specimen, but it is subject to the interaction of the specimen with light. A majority of biological features are transparent and require a contrast

enhancement mechanism to become visible under the microscope. Hence, biological samples are commonly stained with diverse dyes to enhance their contrast properties.

The most common stain routinely used in brightfield microscopy is the *hematoxylin* and *eosin* (HE). With this method the cell nuclei are stained in blue and the cytoplasm and many extra-cellular components in shades of pink (see biological definitions in section 1.3). In histopathology many conditions can be diagnosed by examining a HE section alone, but in other cases an alternative contrast method such as fluorescent microscopy is needed (see section 1.2). Figure 1.3 illustrates a micrograph of a liver tissue section stained with HE.

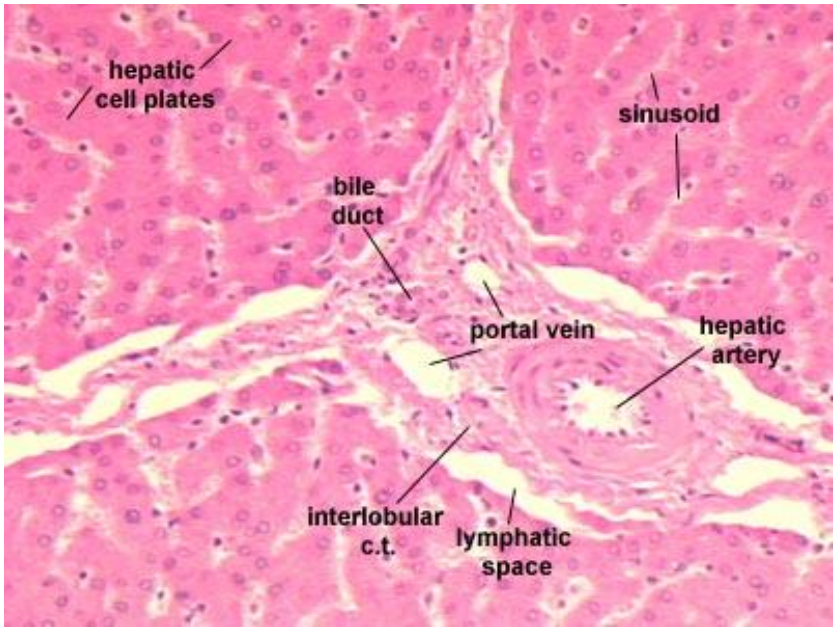

Figure 1.3. Example of liver tissue section with HE stain. Nuclei in purple and cytoplasm in pink. FOV: approx. 650 x 500 μm (width x height) [14].

1.1.5 Refractive index

The refractive index n is a ratio ≥ 1 that describes how light propagates through a medium. It is defined in equation (6), where c_0 is the speed of light in vacuum and c the speed of light in the medium [15].

$$n = \frac{c_0}{c} \tag{6}$$

The refractive index is an important concept in optics, as it defines how light behaves when transitioning from one medium to another. Phenomena such as reflection and refraction of light at the boundary between two media are dependent on their respective refractive indexes.

1.1.6 Snell's law and total internal reflection (TIR)

Snell's law stablishes the relation between the incident angle θ_1 and the refracted (bending) angle θ_2 that a light ray experiments when transitioning from a medium with

refractive index n_1 to a medium with refractive index n_2 (Figure 1.4, a). The mathematical expression of Snell's law is given by equation (7).

$$n_1 sin\theta_1 = n_2 sin\theta_2 \quad (7)$$

Equation (7) holds until the incident ray reaches a critical angle $\theta_1 = \theta_c$, where $\theta_2 = \pi/2$ (Figure 1.4, b). For an incident angle $\theta_1 > \theta_c$, the boundary of the two media acts as a perfect mirror, reflecting the ray into the medium n_1 (Figure 1.4, c). This phenomenon is known as total internal reflection (TIR), and it is the basis for several optical applications such as optical fibers, reflecting prisms and optical waveguides.

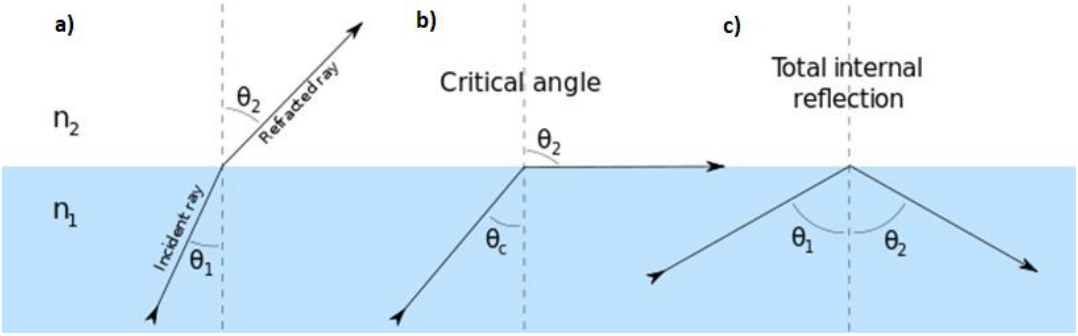

Figure 1.4. Principle of total internal reflection. (a) an incident ray at an angle θ_1 passes from a medium with refractive index n_1 to a medium with refractive index n_2 (where $n_1 > n_2$), and is refracted at an angle θ_2 according to Snell's law. (b) at a critical angle $\theta_1 = \theta_c$ the refracted angle θ_2 reaches $\pi/2$. (c) by increasing the incident angle beyond the critical angle ($\theta_1 > \theta_c$), the boundary of the two media acts as a mirror, reflecting the light inside medium n_1.

1.2 Fluorescence microscopy

Fluorescence microscopy uses fluorescent markers, also referred to as *fluorophores* or *fluorochromes*, to label specific structures of interest within the specimen, resulting in a higher contrast and specificity compared to other staining methods used in light microscopy such as, for example, HE.

Fluorophores are molecules able to absorb and emit light thanks to changes in their energy levels. Each fluorophore is sensitive to a certain incident wavelength of light (λ). Figure 1.5 shows a simplified Jablonski diagram that illustrates the changes in the energy levels of a fluorophore when it is excited by a photon. The arrow in blue color shows the transition of the fluorescent molecule from a low energy level S_0, known as ground state, to a higher energy level S_2, known as excited state. After a short relaxation time, called fluorescence lifetime, the molecules lose some energy in the form of vibration and heat and move to a lower excitation energy level S_1. Finally, the molecules transition back to the ground state level by releasing energy in the form of a photon, in a process called radiative relaxation, shown by the arrow in green color.

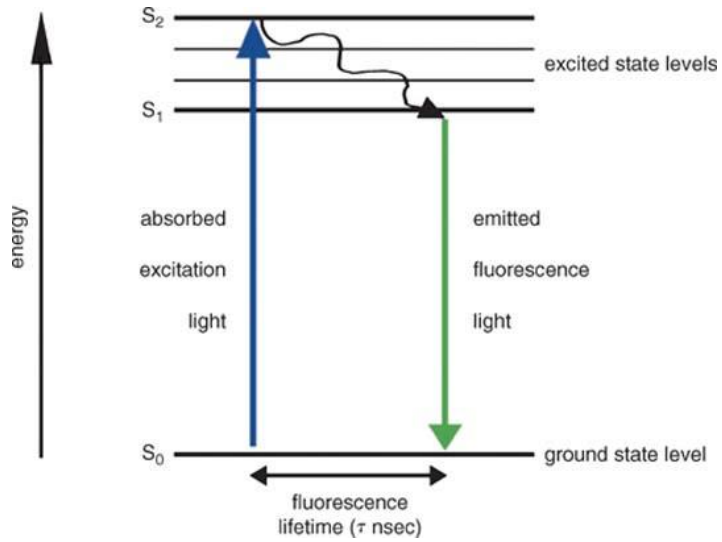

Figure 1.5. Simplified Jablonski diagram [16] .

Due to the principle of energy conservation, the emitted photon carries less energy than the absorbed excitation photon. Evaluating the Planck-Einstein relation in equation (8), where E corresponds to the photon energy, h is the Planck constant, and c is the speed of light, we obtain that - for the case of single photon excitation - the wavelength λ of the emitted light is greater than the wavelength of the excitation light.

$$E = hf = \frac{hc}{\lambda} \tag{8}$$

The difference between absorption and emission wavelengths is known as the Stokes' shift, and each fluorophore type has its own characteristic absorption-emission spectra. In practical terms, in fluorescence microscopy the sample is illuminated with a specific wavelength that matches the excitation spectra of the fluorescent stain. Then, by using a specific bandpass optical filter, the emitted fluorescence light is captured by a photo-detector for imaging. The most common excitation light sources used in fluorescence microscopy are light-emitting diodes (LEDs) and lasers.

Despite its multiple advantages compared to brightfield microscopy, fluorescence microscopy has also its own limitations. Upon illumination, the fluorophores can undergo a chemical change that makes them non-fluorescent, in a process referred to as photobleaching. The photobleaching limits the imaging duration. In addition, the interaction between light and fluorophores, and/or light and cells (particularly for shorter wavelengths), can induce changes in live specimens, in a process known as phototoxicity. Moreover, certain materials and/or subcellular structures may be autofluorescent to specific wavelength used in the experiment, potentially affecting the imaging collection by the microscope.

1.2.1 Fluorescence super-resolution optical microscopy

Fluorescence microscopy techniques such as confocal microscopy and deconvolution microscopy have greatly contributed to the understanding of biological processes at cellular and subcellular level. However, the resolution capabilities of these techniques

are limited by the diffraction of light, meaning that several processes taking place at sub-diffraction limit could not be observed under these microscopes.

From the mid 90's, a new set of sub-diffraction limit fluorescence microscopy techniques became available under the name of optical nanoscopy, or super-resolution microscopy (SRM). These include Structured Illumination Microscopy (SIM), Stimulated Emission Depletion Microscopy (STED) and Single Molecule Localization Microscopy (SMLM).

1.2.1.1 Structured Illumination Microscopy (SIM)

To describe SIM, one needs to refer to two concepts: *spatial domain* (what our eyes perceive), and *frequency domain* (its mathematical representation). The reciprocity between these two is explained by the Fourier theory, which states that any signal in the spatial domain can be expressed as a sum of a series of sinusoids in the frequency domain. In the case of imagery, the variations in brightness across the image field encode information in terms of spatial frequency, amplitude, orientation and phase, all of which can be represented in the frequency domain by performing a Fourier transform of the image (Figure 1.6). When imaging a sample under the microscope, the coarse-spacing between different structures corresponds to low spatial frequency information in the frequency domain, while fine details correspond to high spatial frequency information.

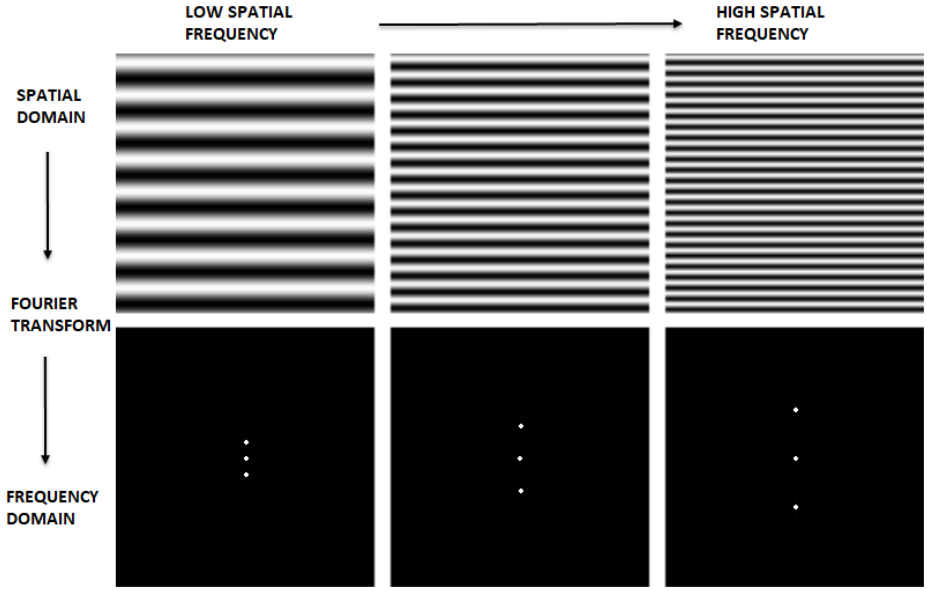

Figure 1.6. Frequency domain representation. Top row: sinusoidal stripe patterns in spatial domain. Bottom row: reciprocal images in the frequency domain. Note that the spacing between the white dots increases as the spatial frequency increases [17].

To improve the resolution of the microscope, SIM makes use of a stripe illumination pattern with a high spatial frequency for the excitation of the fluorescent markers (Figure 1.7, a). Upon illumination, the fine, unresolvable details of the sample and the illumination pattern generate coarse-spaced Moiré fringes that are resolvable by the objective lens (Figure 1.7, c). To obtain high-frequency information from the entire image field, a set up individual images (typically 15 for 3D and 9 for 2D) are taken. The illumination pattern is rotated and phase-shifted to gain an isotropic resolution

enhancement [18]. Finally, a computational algorithm processes all the images in the frequency domain and reconstructs a SIM image with sub-diffraction resolution.

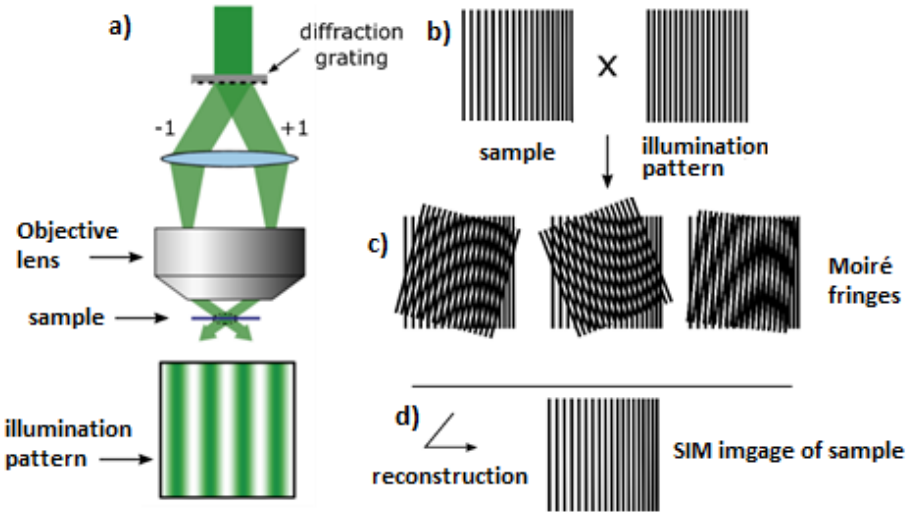

Figure 1.7. Principle of SIM. (a) the illumination pattern consists of sinusoidal stripes produced by interference of two beams exiting a diffraction grating. (b) sample is excited with the illumination pattern. Note the high spatial frequency of the sample and the illumination pattern (c) Diverse coarse Moiré fringes are generated upon rotation and phase-shifting of the illumination pattern. Typically, 3 rotation angles and 5 phase-shifts per rotation are performed. Individual images are acquired for each Moiré fringe. (d) the 15 images are processed by a computational algorithm to reconstruct the SIM image of the sample [19].

Mathematically, the resolution limit R of the microscope in the spatial domain is denoted as the cut-off frequency f_c in the frequency domain, and their relation is given by equation (9). Hence, the objective lens can be described as a low-pass filter in the frequency domain with a characteristic cut-off frequency f_c.

$$R = \frac{1}{f_c} \tag{9}$$

For SIM, the resolution limit R_{SIM} is given by the equation (10), where f_s is the spatial frequency of the illumination pattern projected onto the sample [20].

$$R_{SIM} = \frac{1}{f_c + f_s} \tag{10}$$

The question now is what is the highest spatial frequency observable in SIM? Theoretically, the resolution of this technique becomes unlimited by increasing f_c and f_s. However, in practice when using same objective lens to both generate the illumination pattern and to observe the sample, both f_c and f_s are limited by the diffraction of light. Thus, the practical resolution improvement of this technique following its standard approach is a factor of two (2X) compared to diffraction-limited microscopy, in cases where the objective lens is used both for illumination and collection of light. In practical terms, it means a resolution limit close to 100 nm.

1.2.1.2 Stimulated emission depletion microscopy (STED)

This point-scanning technique implements the concept of deterministic switching by manipulating the photo-physical properties of the fluorophores attached to the sample, so that only a small amount of them emit light at a given location and time. Two laser sources with different wavelengths are simultaneously used in this selective photo-switching process, one with a regular Gaussian beam for regular excitation of the fluorophores (ON state), and another one with a doughnut-shaped beam for stimulated emission depletion (OFF state). Stimulated emission is a radiative process to de-excite electrons, where the energy of the photons from the incident beam matches that of the energy gap of the fluorophore, forcing the excited electrons to decay by emitting photons at the same wavelength of the incoming photons. in STED, the excited fluorophores within the region of the doughnut are forced to the ground state by stimulated emission, whereas those in the very center of the doughnut are not affected by the depletion laser and undergo normal fluorescence by spontaneous emission of photons at longer wavelength than the Gaussian beam. By increasing the intensity of the depletion laser, the radius of the doughnut becomes narrower, allowing for fluorescent emission within a cross section of the sample smaller than the diffraction limit of the objective. By using an adequate emission filter, a set of precision moving mirrors and a photodetector, the sample is then point-scanned, and the image created.

The theoretical resolution of this technique is unlimited but, in practice, the resolution is determined by phototoxicity and the photo-stability of the photo-dyes. Thus, the practical resolution achieved with STED microscopy for biological samples typically goes down to approx. 25-50 nm. Figure 1.8 shows the setup of STED microscopy.

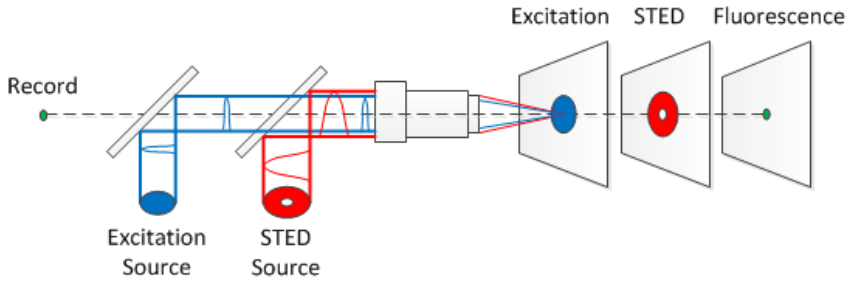

Figure 1.8. Principle of STED. A short-pulse laser (in blue) excites the fluorophores in the sample and a wide-pulse STED laser (in red) forces the fluorophores within the doughnut shape to ground state. The superposition of these two light sources shapes the area of fluorescent to an effective spot (in green) with a cross section smaller than the diffraction limit of the objective. The sample is scanned point-by-point and the fluorescent signal is recorded with a photodetector to generate a super-resolved image [21].

1.2.1.3 Single molecule localization microscopy (SMLM)

SMLM consists of a series of techniques (PALM, STORM, *d*STORM) that implements stochastic switching of fluorophores by manipulating their photo-physical properties. At a single image frame, only a few fluorophores are randomly activated while an image is collected. Then, a computer algorithm processes all the images (typically thousands) according to a predefined filter (Gaussian fit) and, ultimately, generates a super-imposed image that reveals the labeled structure.

The resolution limit of these techniques is dependent on the labeling density and the localization accuracy of the photo-dyes, which is also dependent on the photon count

of each spot of the sample over the acquisition process. Hence, by increasing the exposure time, i.e. collecting more images, it is possible to improve the localization accuracy. However, in practice, the dyes start photo-bleaching after some time, limiting the number of photons that in theory could be collected. Consequently, the practical resolution of the SMLM techniques goes from 20 nm to 30 nm. Figure 1.9 shows the principle of SMLM.

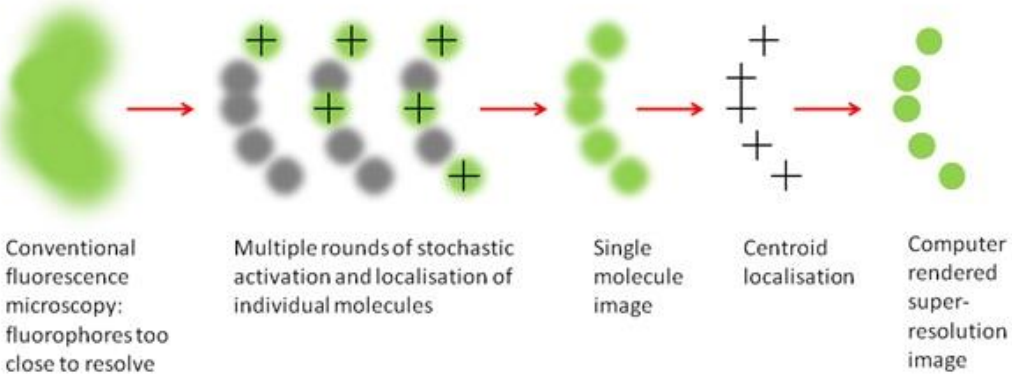

Figure 1.9. Principle of SMLM [22].

1.2.1.4 SRM at the UiT: Waveguide chip-based optical nanoscopy

Since the advent of the SRM techniques in the mid 90's, numerous efforts have been addressed to optimize existing techniques (e.g. development of more photo-stable fluorophores), as well as to create new microscopy methods capable of sub-diffraction resolution. The Optics Group at the UiT is developing a new SRM platform, referred to as waveguide chip-based optical nanoscopy, which employs a photonic chip to provide and control the illumination pattern necessary for super resolution imaging of the sample.

The chip is composed of a bottom layer of silicon (Si) followed by an intermediate substrate layer of silicon dioxide (SiO_2) and a top layer, acting as a waveguide, made of either tantalum pentoxide (Ta_2O_5) or silicon nitride (Si_3N_4) (Figure 1.10, a). The materials of the waveguide layer exhibit excellent properties for guidance of light, thanks to their high refractive indexes (n = 2.0 for Si_3N_4, and n = 2.1 for Ta_2O_5), low absorption and low autofluorescence. Detailed information about the photonic chips used in this study is available on section 2.4.

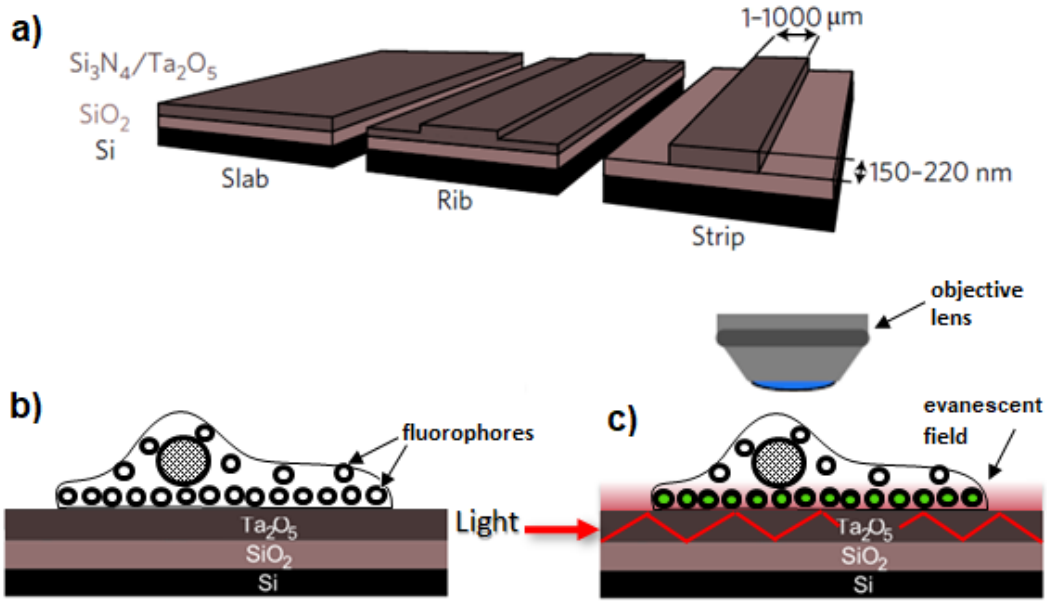

Figure 1.10. Principle of waveguide chip-based nanoscopy. (a) different configurations of the photonic chip: slab, rib, strip. (b) the fluorescent sample is placed on top of the waveguide material. (c) upon coupling at the facet of the chip, light propagates by total internal reflection through the waveguide, creating a thin evanescent field at the surface that excites the fluorophores in its proximity [3].

To acquire the images, the sample is placed in contact with the waveguide layer (Figure 1.10, a) and the edge of the waveguide structure positioned in a precision stage for optical coupling with the illumination source. When coupled, the light propagates through the waveguide material by the phenomenon of total internal reflection (see section 1.1.6), generating an evanescent field of approx. 100 - 200 nm height for the utilized geometries on the surface of the waveguide (Figure 1.10, c). The evanescent field generated on top of the waveguide surface serves as the illumination for total internal reflection fluorescence (TIRF) microscopy [5]. The fluorescent signal from the sample is then collected by the objective lens and imaged by a photodetector such as a camera. The resolution enhancement using waveguide-chip can be obtained in different manners: a) by creating an interference pattern of the beam using counter-propagating waveguides, following the concept of SIM, b) by stochastic photo activation of fluorophores using the evanescent field, following SMLM methods, and c) by performing temporal signal fluctuation-based analysis of multiple images through computational algorithms such as SOFI, ESI, 3B and MUSICAL [23].

One of the main advantages of this novel technique is the high contrast provided by TIRF, as the evanescent field excites only those fluorescent-labeled structures of the sample in close proximity with the surface of the chip, providing optical sectioning and minimizing the background signal. In addition, chip-based nanoscopy decouples the excitation and the collection light paths, supporting large FOV images by using low magnification objective lens, as opposite to conventional TIRF methods (which are often used in SMLM), where a high NA - and consequently high magnification- lens is used for illumination and collection of light, limiting the FOV down to approximately 100 × 100 µm [24]. The technique is significantly less expensive than existing SRM techniques such as SIM, STED and SMLM, as the chip can be mass-produced at low-

cost and the imaging process can be carried out in a conventional low-cost microscope with minimal adaptations for the excitation sources.

Recent studies reported resolution of 47 nm using a 60X/1.2NA objective lens, and 138 nm using a 20X/0.45NA objective lens, with the addition of a large FOV of 500 x 500 μm [3].

One disadvantage of this technique is that it does not allow for 3D imaging, since the optical section is confined within the thin space of the evanescent field. This problem can partly be solved for tissue samples, for example, it is possible to image serial sections of the specimen and reconstruct the 3D image with the aid of a computational algorithm to join several 2D images [25].

1.3 Microanatomy of the body

Cells are the basic building blocks of living organisms in nature, responsible for vital processes such as metabolism, movement and reproduction. Some organisms such as bacteria and protozoa consist of a single cell, namely, unicellular, whereas other organisms such as animals and plants consist of a group of cells that work collectively as a system, namely, multicellular.

The main components of a cell are: the *cell membrane* -also referred to as the plasma membrane- which serves as a barrier between the internal and the external environment of the cell, and the *cytoplasm*, an aqueous fluid that contains intracellular organelles, molecules and structural elements. Depending on how the organelles are contained within the cells, it is possible to classify them into two categories: eukaryotic cells and prokaryotic cells. The first contain membrane-bound organelles, such as the *nucleus*; whereas the latter do not. All species in the animal kingdom are made of eukaryotic cells. Figure 1.11 shows a sketch of a generalized eukaryotic cell, including the most relevant organelles and structures.

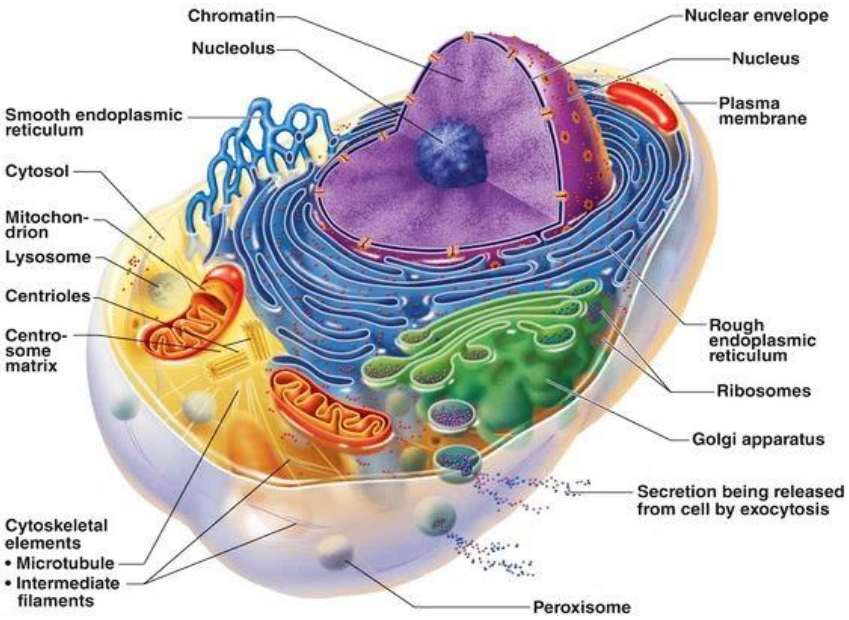

Figure 1.11. Structure of the cell [26].

There are approximately 200 distinct types of cells in the human body, characterized by their structure and size, ranging from approx. 7μm to approx. 120μm depending on the cell type [27]. Inside the cell, organelles and molecules size vary from a couple of nanometers to a few microns. To accomplish the vital activities of the organism, cells with similar structure group together in specific mesh-alike arrays, namely, *tissues*, and work jointly as a unit. The spaces between the cells of a tissue are filled with a non-living material called the extracellular -or intercellular- matrix (ECM). Depending on the tissue type, this material can be abundant in some cases and minimal in others. The ECM may contain special substances such as salts and fibers that are unique to a specific tissue and gives that tissue distinctive characteristics. Organs are made of various tissues, arranged in a particular order. Organs then become part of organ systems, which, ultimately, make up the living organisms (see Figure 1.12).

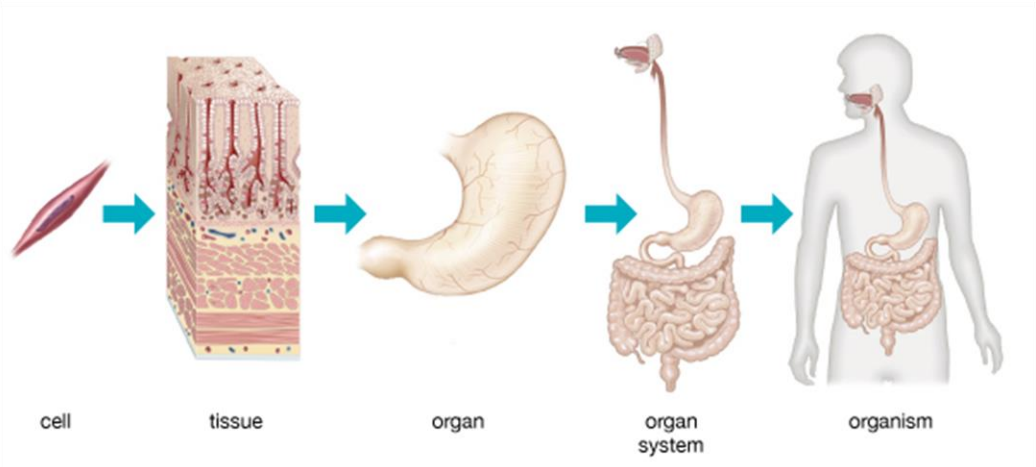

Figure 1.12. Levels of organization in a multicellular organism [28].

Four main tissue types exist in the body: *muscle tissues*, which are capable of contraction and form the body's musculature; *epithelial tissues*, which cover the body's surface and shape the internal organs, body cavities, and passageways; *nerve tissues*, which conduct electrical impulses and make up the nervous system; and *connective tissues*, which are composed of widely spaced cells and substantial amounts of ECM and which bind together various body structures. Bone and blood are considered specialized connective tissues, in which the intercellular matrix is, respectively, hard and liquid [28]. Figure 1.13 shows a sketch of the four types of tissue present in the stomach.

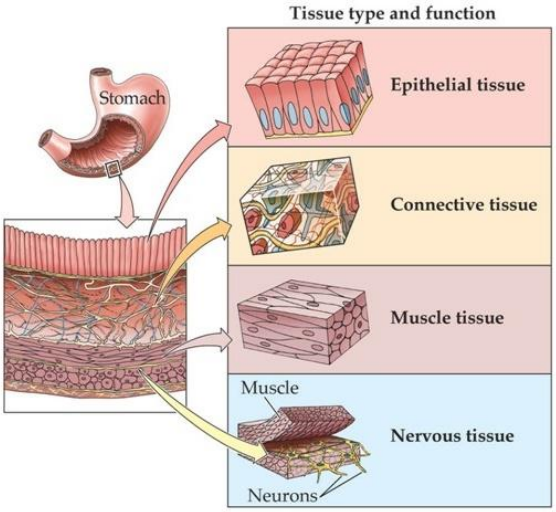

Figure 1.13. Four types of tissue in the stomach [29].

1.3.1 The histology

The study of both the cells and tissues plays a key role in the understanding of biological processes in nature. This knowledge eventually leads to discoveries in the fields of medicine and biology that help in the prevention and treatment of diseases.

Two main study fields have evolved since the invention of the microscope, namely, the cytology and the histology. The cytology deals with the structure, functioning and the chemistry of the cells, whereas the histology studies the morphology and function of the tissues in their respective organs. Within the field of histology, a discipline known as histopathology studies the diseased tissue. Accurate diagnosis of cancer and other diseases usually requires histopathological examination of a small section of the organ tissue.

To observe the microanatomy of the tissues, the sample is first prepared following a protocol, suited to the imaging modality, and then observed under the microscope. To identify the disease, the pathologist typically scans through the totality of the sections in the microscope slide(s). Depending on the specimen size, the imaging area ranges from few mm^2 to several cm^2 [30]. Hence, a common factor to assess the efficiency of a histopathological process is the imaging throughput, which can be defined in several ways, such as high-speed imaging, parallel imaging, increased FOV or multiplexing [31, 32].

The minute scale of certain pathologies requires the use of special technologies such as SRM or EM to observe them. The imaging throughput of these methods is usually low (from few nm^2 to few μm^2 range), which makes them unpractical for routine diagnosis of sub-diffraction anomalies in most pathology labs. Recent studies have improved the image throughput of histological samples by performing an automated sequential scanning SIM acquisition, although the achieved resolution ($> 1\mu m$) is insufficient for diagnosis of sub-diffraction anomalies [30, 33, 34].

Chapter 2. Materials and methods

This section offers a brief description of the three histological samples used in the experiments and a detailed explanation of the equipment, materials and methods used for their observation through the various phases of the master project.

2.1 Histological samples

Three types of histological sections, proceeding from human and non-human origin, were used in this master project, namely, liver tissue, placental tissue and cardiac muscle tissue. The selection of the samples was based primarily on specimen availability from the collaborators. The liver samples were provided by the Vascular Biology Research Group, Department of Medical Biology at the UiT; the placental tissue was provided by the Women's Health and Perinatology Research Group, Department of Clinical Medicine at the UiT; and the cardiac samples were provided by the Heart and Lung Clinic at the UNN.

2.1.1 Liver tissue

The liver is an organ responsible for essential functions such as digestion, metabolism, immunity, and the storage of nutrients. It is made of approximately 100.000 functional units known as lobules [35]. The lobules have a hexagonal shape consisting of a central vein surrounded by six portal triads, each one containing a branch of a bile duct, a hepatic portal vein and a hepatic artery. The connection between the central vein and the portal vein and hepatic artery is made by capillary-like blood vessels known as sinusoids, formed by endothelial cells -also called Liver Sinusoidal Endothelial Cells (LSECs)-. The sinusoids are underlined by the hepatocytes, forming hepatocyte cords that radiate from the central vein to the portal triads (see Figure 2.1, A). The hepatocytes are cuboidal epithelial cells that make up most of the liver tissue (approx. 60-80%) and perform most of the liver's functions. Other types of cells also present in the liver tissue are (Figure 2.1, B): the Kupffer cells (specialized macrophages), the Stellate cells (responsible for ECM production and blood flow regulation in the sinusoids), and the Cholangiocytes (lining the bile duct).

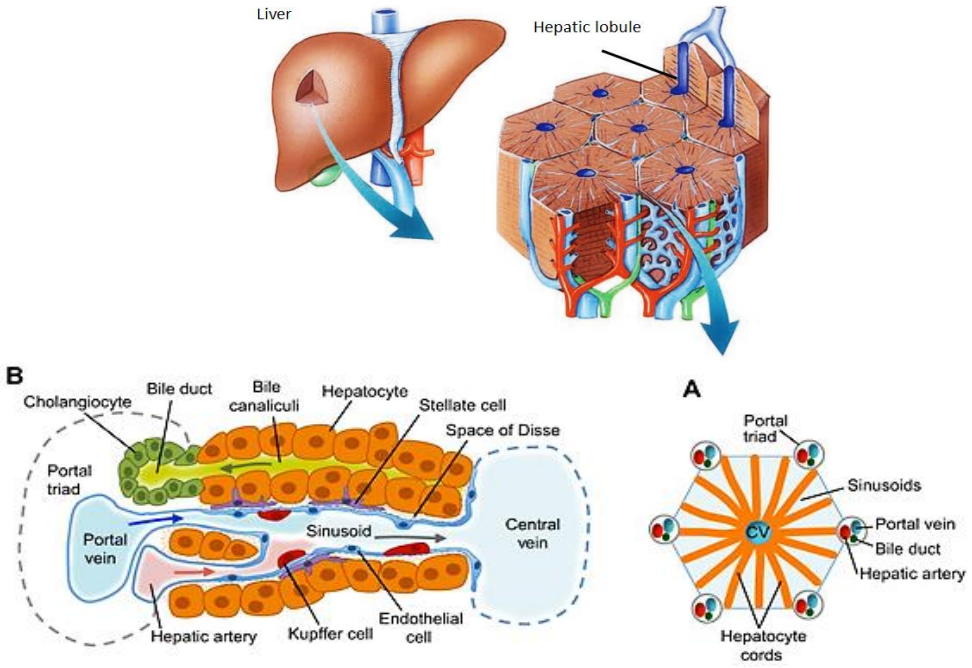

Figure 2.1. Anatomy of the liver. A) schematic of the hepatic lobule. B) parts of the liver tissue [36].

2.1.2 Placental tissue

The placenta is a pregnancy-specific organ of placental mammals, including humans, serving as a boundary between the fetus and the mother's body. It provides the fetus with nutrients, allows for gas exchange, temperature regulation and waste elimination. It also protects the fetus against pathogens and produce hormones which support pregnancy. The placental tissue evolves during the various stages of the pregnancy, but in general it is clearly divided into two components, the fetal and the maternal side. All the biochemical exchange between mother and fetus takes place at the interface between these two components. On one hand, the decidual tissue from the maternal side provides with blood from which the fetal chorionic villi, a tree-like tissue, takes in the nutrients and disposes the waste (Figure 2.2, B). The outer layer of the chorionic villous is formed by a layer of cells called syncytiotrophoblasts (SYN). To ensure proper anchoring to the endometrium and correct blood supply from the spiral arteries of the mother, the subsyncytial cytotrophoblasts (sCTB) cells break through the SYN layer and invade the decidua as extravillous cytotrophoblasts (EVT), in a process called trophoblast invasion. Inside the chorionic villi, the fetal blood circulates through the fetal capillaries, surrounded by endothelial cells (VEC).

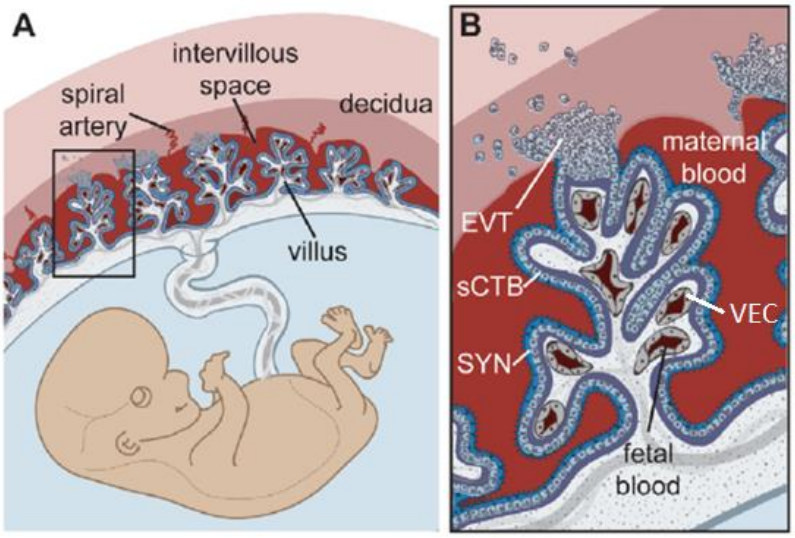

Figure 2.2. Anatomy of the human placenta. A) Schematic overview of the placenta. B) Fetal chorion villi with different trophoblast cells and fetal capillaries with endothelial cells [37].

2.1.3 Cardiac tissue

The heart is one of the most important organs of the body. It is formed by a specialized type of muscle tissue, capable of enduring periodic contractions throughout an entire lifetime without rest. The muscle tissue is made up primarily by muscle cells, also known as cardiomyocytes, which exhibit dark-light striations made of highly organized unites, called sarcomeres, associated with the muscle contractions, and a high mitochondrial density that allows quick production of the cell's energy to avoid fatigue. Moreover, cardiomyocytes have a branched shape so that each cell is in contact with three of four other cardiac muscle cells, through tight junctions called intercalated disks. A second type of cell in the cardiac muscle tissue is the cardiac pacemaker cells, which delivers the electrical impulses that control the heart rate.

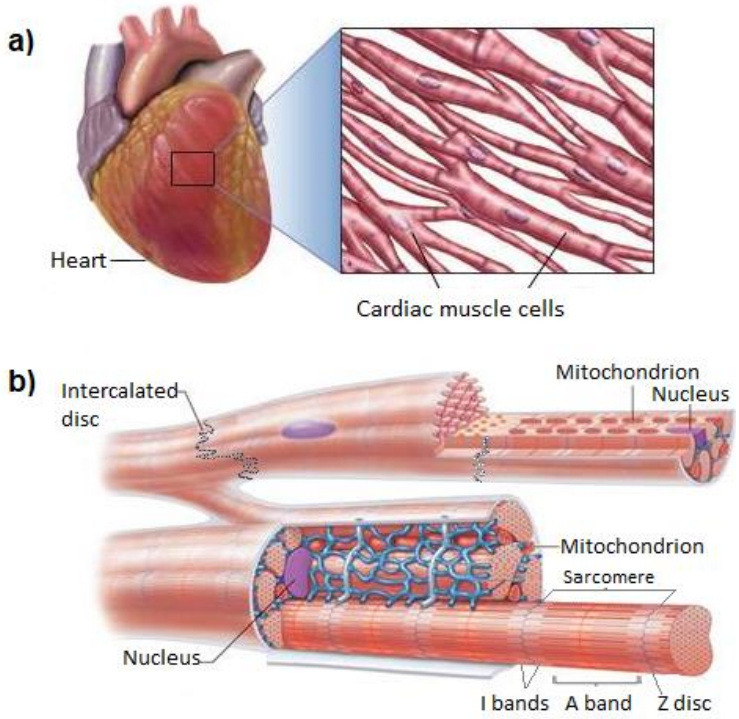

Figure 2.3. Anatomy of the cardiac muscle tissue. (a) Cardiomyocytes have a branched shape and striations associated with the contractile functions. (b) internal anatomy of a cardiomyocyte. Note the high concentration of mitochondria [38].

2.2 Sample preparation steps for fluorescence microscopy

Generally, the histological studies consist of removing, fixing and sectioning a part of an organ, followed by staining and observation under the microscope. Histological stains are of a significant importance, as they allow physicians to visualize and differentiate microscopic structures which serve in the diagnosis of diseases.

Sample thickness, particularly on tissues, plays a significant role in many microscopy techniques, as the out-of-focus information of the background can be captured by the microscope, reducing the contrast properties of the image. Therefore, for most microscopy techniques, it is relevant to ensure thin sections are placed on the slide before imaging.

To preserve the morphology and provide mechanical strength while sectioning, the tissue must be prepared in a series of controlled steps. Two distinct strategies can be used for histological preparation, namely, formalin-fixed paraffin-embedded preservation and cryo-preservation. The following sections provide a general overview of these techniques, followed by a detailed explanation of the specific sample preparation protocols used in this study.

2.2.1 Formalin-fixed paraffin-embedding preservation (FFPE)

Paraffin embedding consists of a series of steps in which the specimens are infiltrated with a paraffin wax-based agent that, once solidified, provides mechanical support necessary for thin sectioning. The process, which covers fixation, grossing, processing, embedding, sectioning, de-paraffinizing, rehydrating, antigen retrieval, blocking and staining of the specimen (Figure 2.4), can take from 12 hours to 48+ hours depending on the volume of the specimen and the number of slices to prepare. Paraffin embedded specimens benefit from high stability, allowing for several years of storage at room temperature [39]. FFPE tissue specimens account for the largest number of histological samples archived around the world. Over 400 million FFPE blocks are estimated across biorepositories in United States alone [40]. Moreover, FFPE blocks have been the mainstream for pathological diagnosis for almost a century.

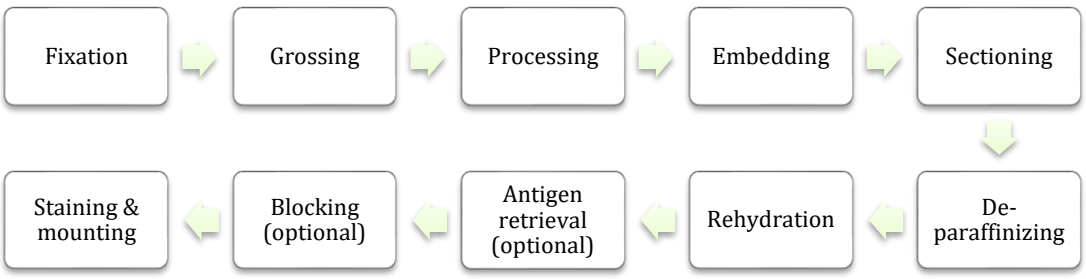

Figure 2.4. Preparation steps for FFPE samples.

2.2.1.1 Fixation

This step aims to prevent the decay (autolysis or putrefaction) of the specimen while preserving its structural characteristics. Fixation methods fall into two classes: organic solvents, such as alcohols and acetone, and cross-linking reagents, such as paraformaldehyde (PFA, polymeric formaldehyde). Cross-linkers preserve cell structure better than organic solvents but may reduce the antigenicity of some cell components.

The most popular fixative is a formaldehyde-based solution, known as *formalin*, which can be applied via vascular perfusion of the organ, or by immersion of the specimen. In the first case, the fixation process only takes minutes, while in the second case specimens must be immersed for 6 to 12 hours, depending on their size and characteristics. The sooner fixation is initiated after detachment from its blood supply, the better the result.

2.2.1.2 Grossing

Once the specimen has been fixed, a visual examination is performed. Relevant information describing the sample is noted down, including the appearance, the number of pieces and their dimensions. The tissues selected for processing are placed in small perforated baskets, commonly known as cassettes, which are loaded onto a tissue processor for processing through wax.

2.2.1.3 Dehydration

The processing consists of a series of steps in which specimens are infiltrated with a sequence of different solvents, typically ethanol and xylene, to allow for clearing and dehydration of the sample before the next step in molten paraffin wax. The duration and step details of the processing schedule will depend on the nature and size of the specimen, ranging from 1h for small specimens to 12h or more for large specimens.

2.2.1.4 Embedding

After processing, the sample is removed from the cassette and placed in a cubically shaped mold which will be filled with wax. The specimen is carefully placed to allow optimal sectioning orientation of the region of study. After solidification, the resulting specimen block provides a stable base for clamping and sectioning in the microtome.

2.2.1.5 Sectioning

The paraffin-embedded sample is sectioned using a microtome by means of extremely sharp blades made of steel, glass or diamond. Sample thickness plays a significant role in many microscopy techniques, as the out of focus information increases the background noise and reduces the contrast properties of the image. Thus, it is relevant to ensure thin sections for optimal imaging results. Paraffin sections are usually cut at a thickness of 3 - 5µm ensuring that only a single layer of cells makes up the section.

Right after sectioning, the sections fall in suspension in a bath of warm water and are then scooped onto a microscope slide for later staining.

2.2.1.6 Deparaffinization and rehydration

A set of steps are required to remove the paraffin and rehydrate the sample before staining. A typical process involves 3 changes of xylene for 5 minutes each, 2 changes of 100% ethanol for 5 minutes each, 2 changes of 95% ethanol for 5 minutes each, 1 change of 70% ethanol for 5 minutes and 2 changes of distilled water for 1 minute each.

2.2.1.7 Fluorescent staining

As mentioned in section 1.1.4, most types of optical microscopy techniques require staining of the sample to increase the image contrast and reveal structural details. There are three main techniques to fluorescently label biological samples, namely, the direct use of fluorescent dyes, immunolabeling, and fluorescent fusion proteins.

Fluorescent dyes are fluorophores that have been structurally modified or conjugated to certain molecules to allow them to bind to specific targets (e.g. proteins or organelles in the sample). An example of this is the Alexa Fluor 488 Phalloidin, which is a commercial green-fluorescent fluorophore dye (Alexa Fluor® 488) conjugated to a phalloidin bicyclic peptide that has high affinity to the actin filaments in the cells. The labeling protocol of fluorescent dyes is generally simpler and shorter compared to other fluorescent labeling techniques. However, there is a limited availability of fluorescent dyes that can be used as direct markers, making it necessary to use more advanced labeling methods such as immunolabeling or fluorescent fusion proteins.

Immunolabeling, also known as immunohistochemistry (IHC), refers to a series of techniques (direct immunolabeling or indirect immunolabeling) that make use of fluorophores in combination with antibodies during the staining process. Each type of antibody will only attach to a specific type of antigen, enhancing the labeling specificity and thus allowing visualization of the location and distribution of the targeted structures or molecules. In direct immunolabeling**,** the fluorophore is conjugated to a single primary antibody that binds to the protein of interest (see Figure 2.5, left). In indirect immunolabelling, the primary antibody binds to the antigen of interest but carries no fluorescent dye. A secondary antibody conjugated to a fluorophore is then employed which will bind to the primary antibody (see Figure 2.5, right). As multiple secondary antibodies can attach to primary antibodies, the fluorescent signal is enhanced compared to that of direct immunolabeling. Additionally, indirect immunolabeling allows for a wide variety of dye combinations in the design phase of the experiment, since diverse fluorophores conjugated to secondary antibodies are commercially available on the market. However, the protocols for indirect immunofluorescence are usually more complex and time consuming since a two-step staining process is needed. Since in fluorescence microscopy the fluorophore is visualized, and not the target molecule, direct immunolabeling is favored as the fluorophore is closest to the target (Figure 2.5), thus allowing for more exact measurements in SRM, especially those designed to measure colocalization, for example. Immunolabeling techniques are commonly used in fluorescent imaging of fixed cells and tissues, but not in live cell studies, since the introduction of immunoreagents can induce damage or behavioral changes inside the cells [41].

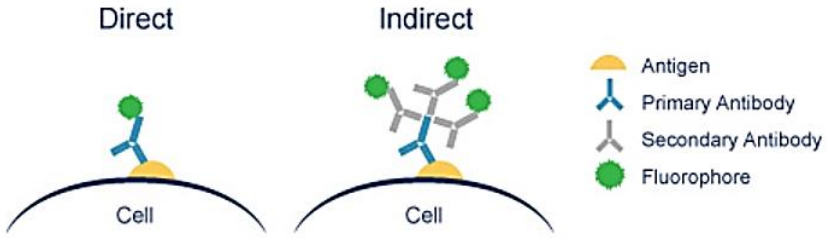

Figure 2.5. Mechanisms of direct and indirect immunolabeling [42].

Fluorescent fusion proteins are genetically modified proteins that are inserted in live host cells, which then produce the target protein with the fluorescent marker permanently attached. This powerful tool is routinely used in live cell studies, but not in histological analysis, as the fluorescent signal decreases after fixation of the specimen [43].

2.2.1.7.1 Additional steps for immunolabeling:

Two steps must be followed before immunolabeling to ensure optimal specificity, namely, antigen retrieval and blocking.

Antigen retrieval helps to break the molecular bridges formed during fixation and unmask the antigenic sites in the sample. There are two methods for antigen retrieval, namely, heat-mediated method and enzymatic method, being the first one the most commonly employed, consisting of incubation of the sample in boiling buffer for several minutes [44].

The **blocking** step masks those non-specific epitopes in the sample to avoid non-specific bindings during the immunolabeling. To carry out this step, the sample is incubated in blocking medium, typically containing bovine serum albumin (BSA), for several minutes.

After antigen retrieval and blocking, the sample can be stained with fluorescent dyes, following specific labeling protocols either for direct or indirect immunolabeling described in section 2.2.1.7.

2.2.1.8 Mounting and sealing

Certain chemical solutions, known as mounting media, can be added after the staining process to avoid photobleaching and to closely match the refractive index for the objective lens. A common aqueous mounting medium is PBS, although there is a wide variety of commercially available solutions to choose from.

The last step consists of covering the tissue with a coverslip and seal its edges, to prevent the sample from drying out and to allow for long-term storage and use. Figure 2.6 shows the mounting and sealing process of a histological sample. Typical sealants are paraffin wax or fingernail polish.

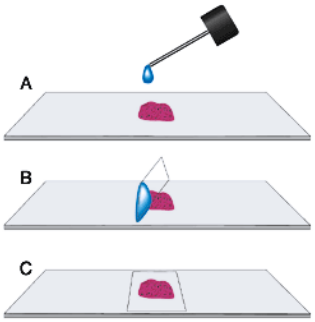

Figure 2.6. Mounting and sealing process. (A) A drop of mounting medium is applied onto the tissue section laying on a glass slide. (B) A coverslip is carefully placed on top of the sample, allowing the mounting medium to uniformly spread out. (C) the excess medium is removed, and the coverslip edges are sealed [45].

2.2.2 Cryo-preservation

This preservation method is less physically stable and with inferior morphology than the paraffin-embedding method. On the other hand, the time for sample preparation is shorter, and it offers better preservation of enzyme and antigen expression, generally allowing for superior immunolabeling. The preparation of cryo-sections does not involve the dehydration and rehydration steps necessary for FFPE samples, thus sectioning, labeling, and observation of specimens can usually be carried out in one day. Cryo-preserved samples can only be stored for up to one year at -80°C. In addition, the samples can be affected by formation of ice crystals, which can damage and distort the overall morphology and impact IHC staining.

2.2.2.1 Fixation

In line with the paraffin-embedding method, the fixation step also plays a key role in the sample preparation of the frozen sections. Two fixation methods are possible: fixation before freezing, and fixation after freezing [46]. In the first case, the sample is perfused or immersed in fixative solution (typically 4% formaldehyde) for 4h to 8h depending on the sample size. In the second case, the sample is snap-frozen after extraction from the organ (see section 2.2.2.2), and kept at -70°C until sectioning, followed by fixation at -20°C.

2.2.2.2 Freezing

To perform cryo-sectioning, the specimen must be snap-frozen in either isopentane or liquid nitrogen, to minimize ice crystal formation and morphological damage. Small samples can be placed in an inert support medium, called optimal cutting temperature (OCT) compound, before freezing.

2.2.2.3 Sectioning

Analogously to FFPE samples, cryo-preserved specimens require thin sectioning for observation using optical microscopes. Two types of instruments are used to section the tissue into thin slices, namely, cryostat microtome and ultramicrotome. In general, these instruments employ sharp steel, glass or diamond-edged knives. The cryostats achieve thin sectioning of 1 - 2 μm thickness, while the ultramicrotomes below 1 μm, and down to 40 nm. Usually 70 nm thick sections are cut for transmission electron microscopy.

To ensure morphological preservation, the sample is kept frozen while fine sections are cut.

After cutting, the cryo-sections are placed onto highly adherent microscope slides and preserved in protectant agent such as sucrose-methyl cellulose solution, until they are ready for staining. The protectant agent is introduced to prevent the biological tissue from drying out.

2.2.2.4 Fluorescent staining

The staining process of the cryo-sections is comparatively simpler with respect to those of FFPE samples. Regardless of the staining method selected, the first step consists of washing off the protectant agent with phosphate buffered saline (PBS). The sample is then ready for fluorescent staining as illustrated in section 2.2.1.7, followed by mounting and sealing per section 2.2.1.8.

2.2.3 Sample preparation protocols specific for this study

Finding the right preparation protocol was crucial for the completion of this master project. To the best of our knowledge, no references existed of super-resolution imaging of liver or placental tissues, but the few reports available of SRM-SIM on tissue sections [47-50] suggested that the samples could be prepared following similar guidelines as on techniques such as confocal microscopy and EM. A considerable amount of time during this master project was spent in learning and optimizing the sample preparation steps to obtain the best results on the two imaging systems used in the study.

Samples were obtained from existing histological specimens, being all fixed, preserved, and conveniently stored in biobanks prior commencement of this master project. Tissue sections of both FFPE and cryo-preserved samples were provided by the collaborators and required further preparation for super-resolution imaging. FFPE liver blocks were sectioned using a Microm HM440E Microtome (GMI, Ramsey, USA), while FFPE placental sections were obtained with a HM355S Microtome (Thermofischer Scientific, USA). Both microtomes were equipped with S35 stainless steel disposable microtome blades (Feather). Cryosections were obtained following Tokuyasu method [51] with a Leica EMUC6 Ultramicrotome (Leica Microsystems, Germany), equipped with glass knife. The histological samples and section thicknesses are shown in Table 1.

Tissue type	Origin species	Preservation	Thickness (nm)
Liver	Rat	Cryo	300 / 1000
Cardiac	Pig	Cryo	70 / 110 / 400
Liver	Human	FFPE	4000
Placental	Human	FFPE	4000

Table 1. Section thickness of the histological samples used in the study.

For imaging with the OMX microscope, the samples were placed and prepared directly onto three different substrates, namely, #1.5 coverslips of diverse geometries - ø13 mm, 18 × 18 mm, 22 × 22 mm- (VWR, Oslo, Norway), microscope slides and photonic chips. For imaging on the photonic setup, samples were placed and prepared directly

onto the surface of the chip. To ensure optimal adherence, both coverslips and chips were coated with poly-L-lysine (Sigma Aldrich, Oslo, Norway) prior to deposition of tissue sections.

FFPE-sections were prepared according to the steps listed in Appendix A. In short, upon sectioning, both coverslips and chips -from this point jointly referred to as *samples*- were positioned in a coverslip rack (VWR, Oslo, Norway) and placed on a heating incubator (Labolytic, Trondheim, Norway) at 60°C overnight. The samples were deparaffinized in xylene (3 × 5 min) and rehydrated in an ethanol/water gradient series: 100% (2 × 10 min), 96% (2 × 10 min), and 70% (10 min) ethanol, respectively. The rehydrated samples were immersed in a bleaching solution (30 min) to reduce autofluorescence and then washed in MilliQ water (5 min). Antigen retrieval was performed by boiling the samples in citrate buffer in a microwave (2 × 5 min), followed by cooling down at RT (20 min). The samples were washed in MilliQ water (3 × 2 min) and washed (2 min) in buffer solution (details in Appendix A) before incubation (30 min) in blocking buffer (details in Appendix A) at RT. The primary antibody was incubated with the samples overnight at 4°C in a humidified chamber, and then washed off with washing buffer (3 × 5 min). The secondary antibody was incubated for 1 hour at RT and washed with PBS (2 × 5 min) before incubation with Cell Mask Orange (CMO) (10 min) (ThermoFisher Scientific, Oslo, Norway). The samples were washed with PBS (2 × 5 min) and incubated with nuclear staining (5 min), followed by a wash with MilliQ water (2 × 5 min). Samples on coverslip were mounted with Prolong Gold (ThermoFisher Scientific, Oslo, Norway) and placed in the center of microscope slides (due to small travel range of the sample stage at OMX). After hardening of the mounting medium (30 min), the slides were sealed with nail varnish. Samples on chip were mounted with PBS, then cover slipped with 18 × 18 mm No. 1 or No. 1.5 coverslips (VWR) and sealed with picodent twinsil 22 before imaging. All samples were stored in the dark at 4°C prior to imaging. Detailed information about the stains and antibodies can be found in Table 2.

Cryo-sections were prepared according to the steps listed in Appendix B. In summary, samples were washed with PBS (3 × 7 min) at 4°C to dissolve the sucrose-methyl cellulose protectant. Following the blocking step, the samples were stained in a similar manner as the FFPE samples. Samples on coverslip were mounted identically as described for the FFPE samples. Samples on chip were mounted similarly to the FFPE samples, except for the imaging medium, which consisted of an water-based enzymatic oxygen scavenger system solution containing glucose oxidase (Sigma-Aldrich) and catalase (Sigma-Aldrich) [3] mixed with PBS and glycerol, to reduce photobleaching of the fluorophores. All samples were stored in the dark at 4°C prior to imaging. Detailed information about the stains and antibodies can be found in Table 2.

For autofluorescence studies, samples were prepared according to the above described methods, excluding antibodies and fluorescent dyes.

Whenever possible, imaging was performed within 1-2 days after staining the tissue sections to avoid decay of the dyes, although it was found out that the fluoresce properties remain acceptable after months of storage of the prepared samples.

Imaging platform	Ref. #	Tissue type	Preservation	Stain						
				Target	Ab	Name / Description	Manufacturer	Cat. No.	Stock concentration	Working concentration
OMX	1	Rat liver	Perfusion fixation	LSEC	-	Alexa Fluor 488 conjugated to formaldehyde-treated serum albumin (FSA) [52], staining via vascular perfusion prior to perfusion fixation.	N/A	N/A	N/A	N/A
				Membranes	-	Cell Mask Orange	ThermoFischer	C10045	5 mg/ml	1:2000
				Nuclei	-	DAPI	ThermoFischer	62247	1 mg/ml	1:1000
	2	Human liver	FFPE	LSEC	1st	Goat anti human mannose receptor CD206	R&D Systems	AF2534	0.2 mg/ml	1:40
					2nd	Alexa Fluor 488-donkey anti goat	ThermoFischer	A11055	2 mg/ml	1:500
				Membranes	-	Cell Mask Orange	ThermoFischer	C10045	5 mg/ml	1:2000
				Nuclei	-	DAPI	ThermoFischer	62247	1 mg/ml	1:1000
	3	Human placenta	FFPE	Membranes	-	Cell Mask Orange	ThermoFischer	C10045	5 mg/ml	1:2000
				Nuclei	-	DAPI	ThermoFischer	62247	1 mg/ml	1:1000
	4	Pig heart	Cryo	Membranes	-	Cell Mask Orange	ThermoFischer	C10045	5 mg/ml	1:2000
				Nuclei	-	DAPI	ThermoFischer	62247	1 mg/ml	1:1000
OMX & Photonic chip	5	Pig heart	Cryo	Membranes	-	Cell Mask Orange	ThermoFischer	C10045	5 mg/ml	1:2000
				Nuclei	-	Sytox Green	ThermoFischer	S33025	50 μM	1:300
	6	Human liver	FFPE	LSEC	1st	Goat anti human CD32	R&D Systems	AF1330	0.2 mg/ml	1:50
					2nd	Alexa Fluor 647 donkey anti-goat	ThermoFischer	A21447	2 mg/ml	1:500
				Membranes	-	Cell Mask Orange	ThermoFischer	C10045	5 mg/ml	1:2000
				Nuclei	-	Sytox Green	ThermoFischer	S33025	10 μM	1:60

Table 2. List of antibodies and stains used in the study.

2.3 OMX imaging

A commercial microscope was used in the first phase of the master project, the DeltaVision OMX V4 Blaze imaging system (GE Healthcare, USA) equipped with a 60X/NA1.42 oil-immersion objective (Olympus), three sCMOS cameras, four excitation lasers (405 nm, 488 nm, 568 nm, 642 nm) and four emission filters (419-465nm, 500-550 nm, 609-654 nm, 665-705 nm).

To compare results, two available modalities were used, namely, deconvolution microscopy (DV) and SIM. DV is a diffraction-limited technique used in fluorescence microscopy to enhance image contrast by removing the out of focus blur. The technique reduces the out-of-focus information via mathematical algorithms [53], and requires optimization of the PSF by matching the refractive index of the immersion oil to that of the coverslip. This is an iterative process done by changing the immersion oil and observing the PSF of single emitters in the orthogonal view of the deconvolved images, until symmetrical shapes are obtained (Figure 2.7). The PSF optimization plays a key role in the quality of SIM, since oil mismatch can introduce artifacts in the reconstructed image [54], as detailed in Appendix C.

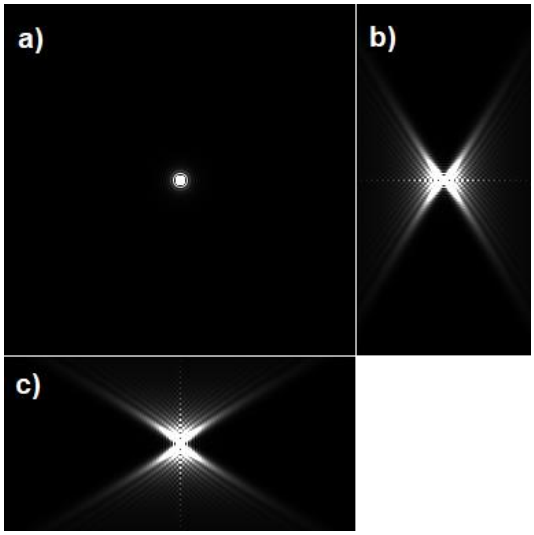

Figure 2.7. PSF of a single emitter. a) Single emitter. b) and c) Orthogonal views of the PSF [55].

After PSF optimization, DV images were acquired, followed by SIM images. Images from these two modalities consist of a projection of multiple images (z-stacks) acquired in controlled steps (z-sections, or optical sections) along the optical axis of the microscope. Following Nyquist sampling theorem, steps of 250 nm size were required for DV images of 500 nm axial resolution, and 125 nm step size for 3D-SIM images of 250 nm axial resolution. Projected SIM images are commonly referred to as 3D-SIM. In DV mode, a single 2-D frame was acquired on each z-section, while in 3D-SIM a total of 15 2D-frames were acquired for each z-section, corresponding to the three angles and five phase shifts of the illumination pattern. The thickness of the z-stack was adjusted according to the tissue section thickness by selecting the upper and lower limits of the objective where the image started to become out-of-focus. For multi-color

imaging, z-stacks of individual channels were sequentially acquired, transitioning from longer to shorter excitation wavelengths.

Imaging parameters such as illumination intensity and exposure time were optimized during the imaging process to avoid photobleaching of the dyes. The maximum intensity count was approx. 10000 for all dyes, except for DAPI, which was approx. 4000 counts. The OMX allowed for a maximum image size of 1024 × 1024 pixels for DV and 512 × 512 pixels for 3D-SIM, corresponding to a FOV of approx. 80 × 80 μm and approx. 40 × 40 μm, respectively. For large FOV, the sample was scanned at steps of 70 μm and 30 μm for DV and 3D-SIM, respectively, and the collected images were computationally stitched in tile mosaic images.

2.4 Chip-based imaging

The second phase of the master project consisted of imaging tissue sections using the prototype chip-based microscopy technique described in section 1.2.1.4. The imaging process was carried out on silicon nitride (Si_3N_4) waveguide chips manufactured at the Institute of Microelectronics Barcelona (IMB-CNM, Spain), following standard complementary metal–oxide–semiconductor (CMOS) fabrication processes [3, 24, 31]. Strip Si_3N_4 uncladded waveguide geometries with strip heights of 150 nm and various widths (200 μm, 320 μm, 400 μm, 600 μm and 1000 μm) were chosen for imaging of tissue sections (Figure 2.8).

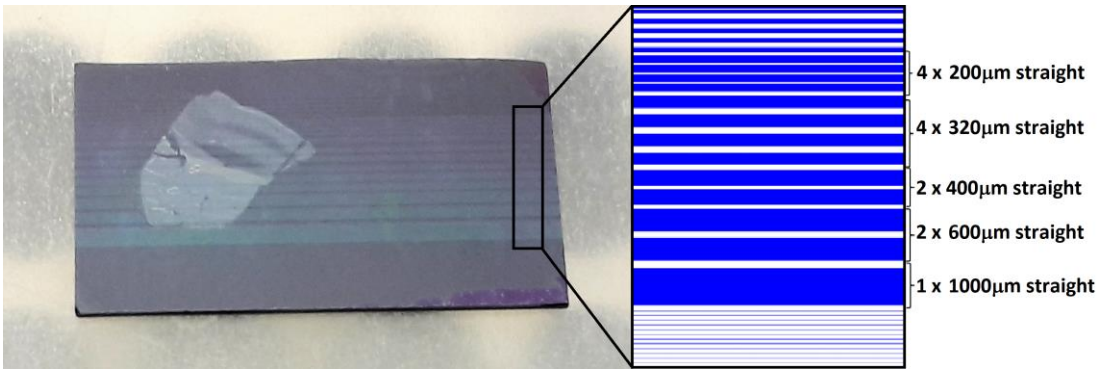

Figure 2.8. FFPE sample on a Si_3N_4 photonic chip. Inset illustrates the different waveguide widths available on the chip.

Preparation of the chip was as follows: Silicon wafers were cleaved upon reception from the manufacturer, according to individual chip designs. Chips were spin-polished at the coupling facet at 4000 rpm using diverse silicon carbide grinding papers, transitioning from thicker to thinner grit size (5 μm for 3 min, 3 μm for 5 min, 1 μm for 3 min). The remaining photoresist layer from the manufacturing process was removed by immersion in acetone for 1 min. The chip was then cleaned for 10 min in 1% Hellmanex in deionized water on a 70°C hotplate, followed by rinsing steps with isopropanol and deionized water, as well as rubbing with a cleanroom type swab. The chip was finally dried using an air blow gun with compressed nitrogen.

Image acquisition was performed in the photonic setup shown in Figure 2.9. Upon sample preparation (see section 2.2.3), the chip was positioned on a vacuum holder mounted on a translation stage. Three illumination sources (660 nm Cobolt Flamenco, 561 nm Cobolt Jive, and 488 nm Oxxious LBX 488) were expanded, collimated and aligned to the optical axis of a coupling objective (Olympus, LMPlanFL 50x/NA0.5), held by a 3-axis piezo-controllable stage (Melles Griot, 17MAX604). The light was coupled onto the waveguides by bringing the focal point of the coupling objective to the input facet of the waveguide. When coupled, the guided light generated an evanescent field of approx. 150-200 nm on top of the surface of the waveguide, which served for TIRF microscopy. The fluorescent signal was collected by an objective lens and filtered through a series of long-pass (LP) and band-pass (BP) filters according to the excitation source and emission spectra of the dyes in the sample, as illustrated in Table 3. The filtered signal was imaged using a sCMOS camera (Hamamatsu Orca flash v4). The collection components were mounted on a modular microscope body (Olympus BXFM), which rested on motorized stages (Thorlabs) for displacement over the chip surface. The waveguide widths allowed large amount of modes to propagate in multi-mode interference (MMI) patterns that lead to non-uniform excitation of the fluorophores in the sample. To obtain a uniform excitation, for each frame acquisition, the coupling objective was continuously scanned at incremental steps of 0.2 μm at 25 Hz over 30 μm travel span along the input facet of the waveguide using the piezo-controllable stage. Multiple images (typically 100) were acquired and computationally post-processed to obtain an averaged image per excitation channel. Each channel was independently acquired and computationally merged for multi-color imaging. Different collection objectives were used to obtain diverse FOVs (4x/NA0.10, 20x/NA0.45, 25x/NA0.85 water-immersion, 60x/NA1.2 water-immersion). Excitation power - at the laser - used for TIRF imaging was highly dependent on the sample type and the experimental settings. Typical values are shown in Table 9. Camera exposure times for TIRF imaging was dependent on the emission count of the camera, with typical values of 100 - 300ms. Individual adjustments of laser power and exposure time were done on a case-by-case basis to optimize image acquisition.

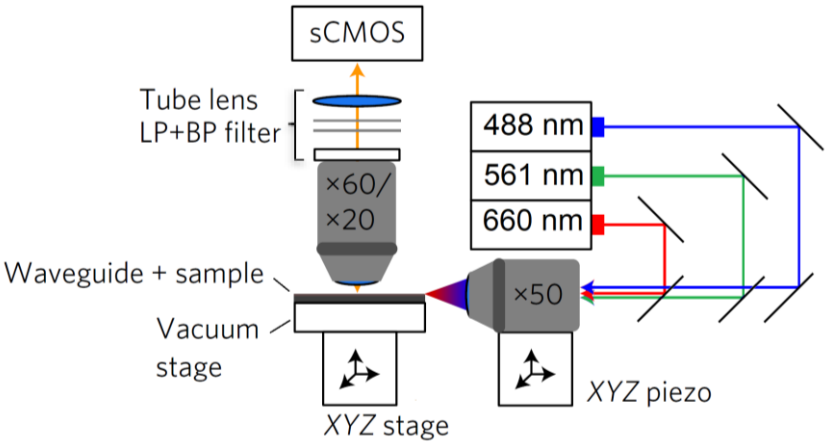

Figure 2.9. Photonic waveguide chip-based setup. Light sources of different wavelengths (488 nm, 561 nm and 660 nm) are coupled to the chip waveguide using an objective lens. The guided light creates an evanescent field that excites the fluorophores close to the surface of the chip. The fluorescence emission is collected by an objective lens and filtered by longpass (LP) and bandpass (BP) filters, before imaging with a sCMOS camera [3].

Excitation wavelength (nm)	Longpass filter (nm)	Bandpass filter (nm)
488	488	520±36
561	561	591±43
660	664	692±40

Table 3. Longpass and bandpass filters used in the photonic setup.

2.5 Image analysis

DV and SIM images were reconstructed using SoftWoRx program, supplied with GE Healthcare with the OMX.

All images were post-processed using open source software Fiji [56].

DV and SIM tile mosaic images were obtained using the grid/collection stitching plugin from FIJI [57].

Chapter 3. Results and discussion

This section shows the results obtained in the two phases of this master project (Figure 3.1), and discusses relevant findings regarding sample preparation, image acquisition and reconstruction artifacts of tissue sections in the two tested platforms, namely, the OMX, and the waveguide chip-based microscopy setup. A correlative light-light microscopy study is presented at the end of this section, offering a comparative view of the same FOV of a cryo-section in the two platforms.

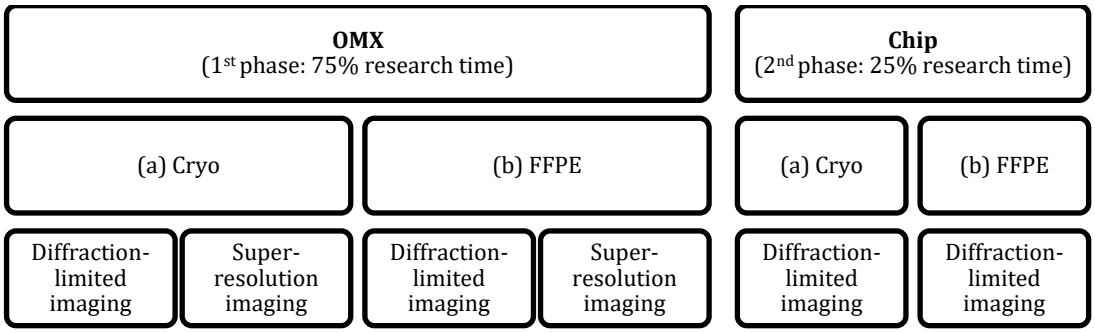

Figure 3.1. Experimental plan. Flowchart of the two phases of the master project.

3.1 Study phase 1(a): cryo-sections on the OMX

This section is divided in three parts: 3.1.1) *imaging results*, offering an explanatory view of the collected images, 3.1.2) detailing the *challenges* associated with imaging cryo-sections on the OMX, and 3.1.3) an open *discussion* of the imaging results.

3.1.1 Imaging results

Cryo-sections from two animal species were imaged on the OMX: rat liver tissue and pig heart muscle tissue. Three types of substrates were used to hold the tissues, namely, #1.5 coverslips, microscope glass slides and waveguide chips, in order to study and compare the imaging results (Table 4).

Tissue type	Origin species	Preservation	Thickness (nm)	Substrate
Liver	Rat	Cryo	300 / 1000	#1.5 coverslip
Cardiac	Pig	Cryo	70	Microscope glass slide
Cardiac	Pig	Cryo	110	Chip
Cardiac	Pig	Cryo	400	#1.5 coverslip

Table 4. Cryo-sections imaged on the OMX.

3.1.1.1 Rat liver cryo-sections

Rat liver cryo-sections of 300 nm and 1000 nm thick, mounted on #1.5 poly-L-lysine coated coverslips, were imaged on the OMX in the DV and 3D-SIM modes. The samples were stained according to ref. #1 in Table 2. Three excitation sources were used for imaging, namely, 568 nm for membranes (CMO), 488 nm for LSEC marker (AF488-FSA) and 405 nm for nuclei (DAPI).

DV and 3D-SIM images of 300 nm thick rat liver cryo-section are shown in Figure 3.2 (a)-(b), respectively. Membranes are shown in red color, nuclei in blue, and LSECs in green. Both DV and 3D-SIM images show the expected morphology of the liver tissue shown in Figure 2.1 (B), with the LSECs (L) lining the sinusoids, and hepatocytes (H) with cuboidal geometry. The lower part of the images (marked with white arrow) show a tissue fragment, most likely resulted due to cryo-sectioning. The contrast enhancement in the 3D-SIM image allows for a clearer visualization of membranes, as compared to the DV image. The intensity profiles along the yellow lines in Figure 3.2 (c)-(d) are plotted in Figure 3.2 (e)-(f), respectively. The DV image shows two maxima separated by approx. 250 nm, whereas the 3D-SIM image exhibits 4 maxima, with a distinguishable separation of the two central peaks at approx. 120 nm. The thicknesses of the z-stacks are 2,5 μm and 1,5 μm for DV and 3D-SIM, respectively.

DV and 3D-SIM images of 1000 nm thick rat liver cryo-section show similar results in terms of contrast as in the 300 nm thickness cryo-section. The 3D-SIM image, illustrated in Figure 3.3 (b) allows for visualization of organelle structures (in red), that are not distinguishable in the DV image from Figure 3.3 (a). However, it is difficult to observe fine details in the magnified sections (c) and (d), due to the multiple z-section projections forming each image. In this case, the z-stack thickness is 4 μm for DV and 2,5 μm for 3D-SIM. The resolution capabilities of each technique can be analyzed using single z-sections from both z-stacks, as shown in Figure 3.3 (e)-(f). The intensity

profiles along the yellow lines demonstrates the resolving power of SIM, with structures within 120 nm distance from one another, whereas DV shows a single structure of approx. 300 nm according to full width half maximum (FWHM).

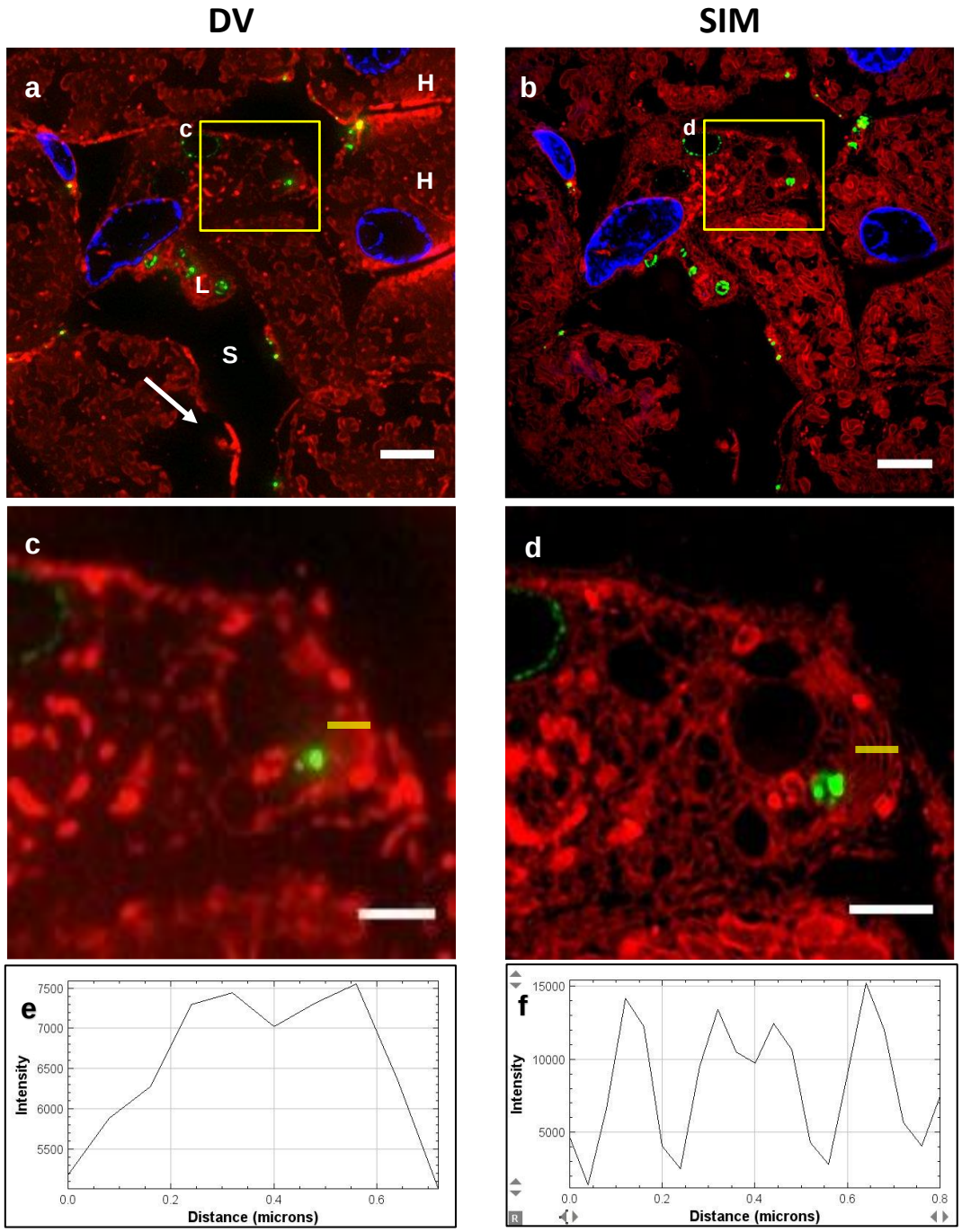

Figure 3.2. Rat liver cryo-section 300 nm thick imaged on the OMX using a #1.5 coverslip as a substrate. Membranes in red, LSECs in green and nuclei in blue. (a) DV image and (b) 3D-SIM image showing hepatocytes (H) and LSECs (L) lining the sinusoid (S). The white arrow indicates tissue morphology disrupted during sectioning. (c)-(d) Magnified sections show higher contrast in SIM compared to DV, allowing for better visualization of membranes. (e)-(f) Intensity profiles along the yellow lines in (c)-(d) show a resolution of approx. 250 nm in DV and approx. 120 nm in SIM. FOV (a)-(b) 40 × 40 μm. Scale bar (a)-(b) 5 μm, (c)-(d) 2 μm.

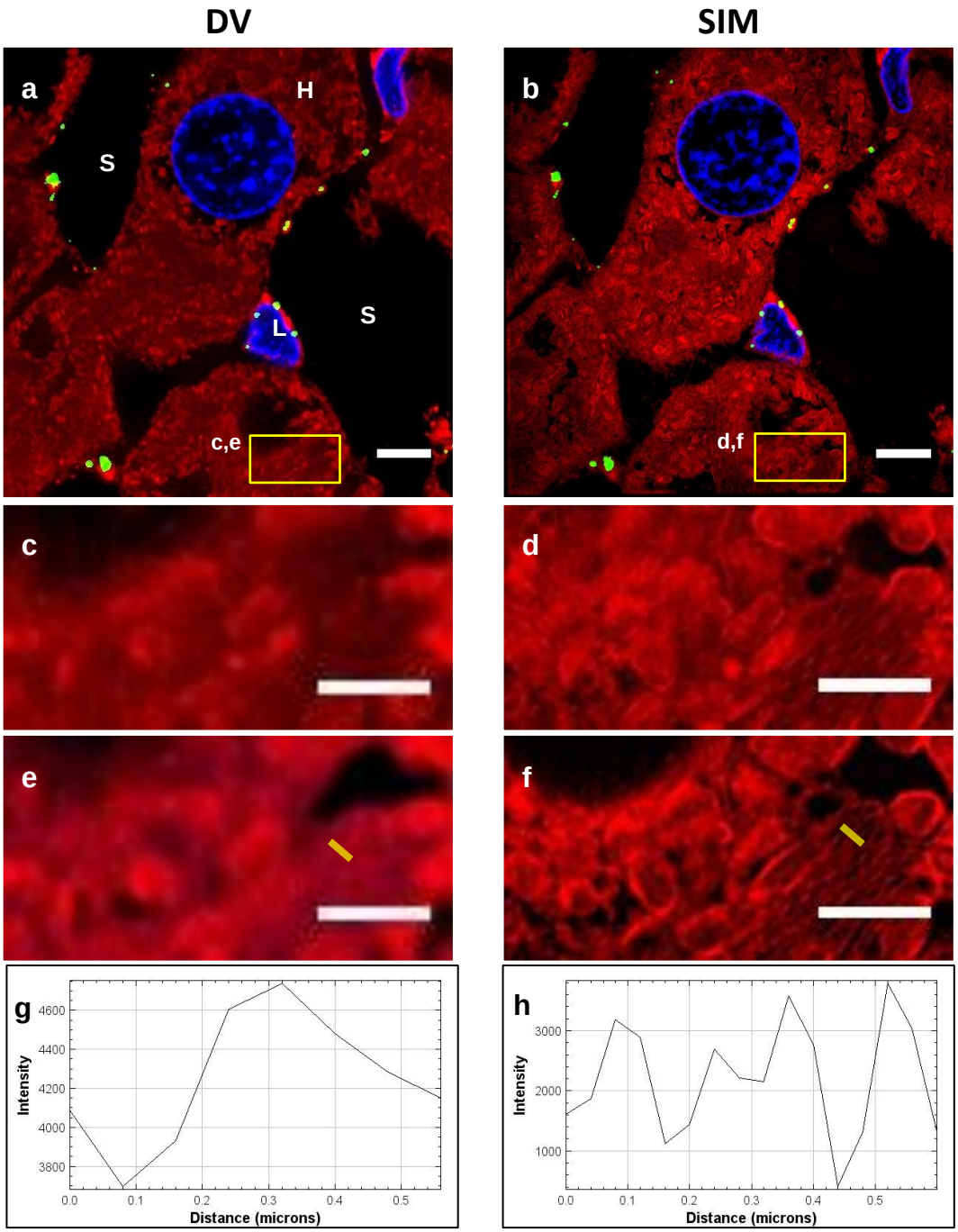

Figure 3.3. Rat liver cryo-section 1000 nm thick imaged on the OMX using a #1.5 coverslip as a substrate. Membranes in red, LSECs in green and nuclei in blue. (a) DV image and (b) 3D-SIM image show hepatocyte (H), LSEC (L) and sinusoids (S). (c)-(d) Magnified sections show higher contrast in SIM compared to DV. (e)-(f) Single z-sections allow for better visualization of morphological features in DV and SIM. (g)-(h) Intensity profiles along the yellow lines in (e)-(f) show a resolution of approx. 300 nm (FWHM) in DV and approx. 120 nm in SIM. FOV (a)-(b) 40 × 40 μm. Scale bar (a)-(b) 5 μm, (c)-(f) 2 μm.

3.1.1.2 Pig heart muscle cryo-sections

Pig heart muscle cryo-sections of various thicknesses (70 nm, 110 nm, 400 nm) were imaged on the OMX in the DV and 3D-SIM modes. To study the influence of different substrates in the imaging results, the 70 nm thick section was placed on a microscope glass slide, the 110 nm thick section on a photonic chip, and the 400 nm thick on a #1.5 coverslip. All tissue sections were stained with the dyes listed on ref. #4, Table 2. After mounting and cover-slipping, samples on chip and glass slide were uniformly pressed with 200g weight for 30 min, to reduce the gap between the coverslips and the tissue sections and allow visualization of the specimens with the high NA objective - short working distance - of the OMX. Two excitation sources were used for imaging, namely, 568 nm for membranes, and 405 nm for nuclei. To obtain large FOV, tissue sections were sequentially scanned in snake-like patterns, as illustrated in Figure 3.4, and the individual images were computationally stitched using Fiji. Imaging results are shown hereon in the following order: (1) 70 nm thick section on glass slide, (2) 400 nm thick section on #1.5 coverslip, and (3) 110 nm thick section on chip.

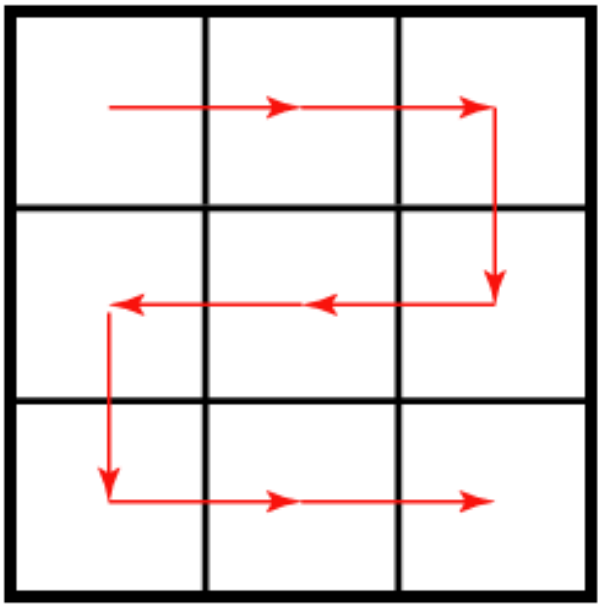

Figure 3.4. Tile mosaic composition for large FOV images on the OMX. Red arrows indicate the snake-like scanning pattern.

Figure 3.5 (a)-(b) shows a 3 × 3 tile mosaic of a 70 nm thick pig heart tissue cryo-section imaged in DV and 3D-SIM using a microscope glass slide as a substrate, resulting in a total FOV of 100 × 100 μm. Cell membranes are shown in red and nuclei in blue. Magnified sections (c)-(d) show high concentration of mitochondria (elongated features in red), matching the description of the heart muscle tissue morphology presented in section 2.1.3. The ultra-thin thickness of the tissue section (70 nm), allowed for low out-of-focus contribution in the projected z-sections, resulting in comparable images in both modalities, with subtle contrast improvement achieved by SIM as compared to DV. The intensity variations in Figure 3.5 (a)-(b) correspond to de-focused areas of the sample during the scanning acquisition as a result of imperfections in the surface of the substrate. This artifact showed more prominently in DV than in SIM.

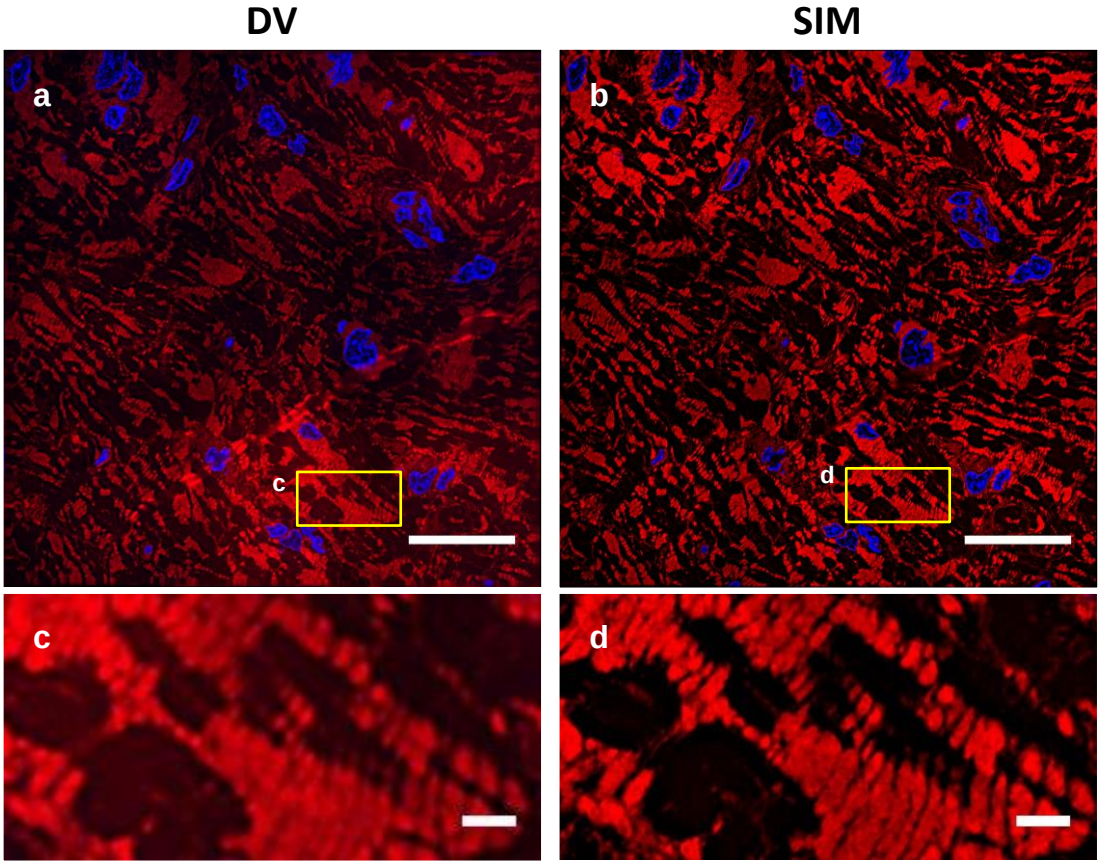

Figure 3.5. 3 × 3 tile mosaic of a 70 nm pig heart muscle cryo-section imaged on the OMX using a microscope glass slide as a substrate. Membranes in red and nuclei in blue. (a) DV image and (b) 3D-SIM image show intensity variations corresponding to de-focused regions along the scanning acquisition, more prominently in DV than in SIM. (c)-(d) Magnified sections show contrast enhancement from SIM compared to DV. FOV (a)-(b) 100 × 100 μm. Scale bar (a)-(b) 20 μm, (c)-(d) 2 μm.

Figure 3.6 (a)-(b) shows a 3 × 3 tile mosaic of a 400 nm thick pig heart tissue cryo-section imaged in DV and 3D-SIM using a #1.5 coverslip as a substrate, resulting in a total FOV of 100 × 100 μm. Imaging results are comparable to those obtained with 300 nm thick rat liver cryo-section (Figure 3.2). Morphological features such as mitochondrial array become more distinguishable in DV and SIM, compared with the previous section of 70 nm thickness. De-focus artifacts are also present in the images, more prominently in DV than in SIM mode.

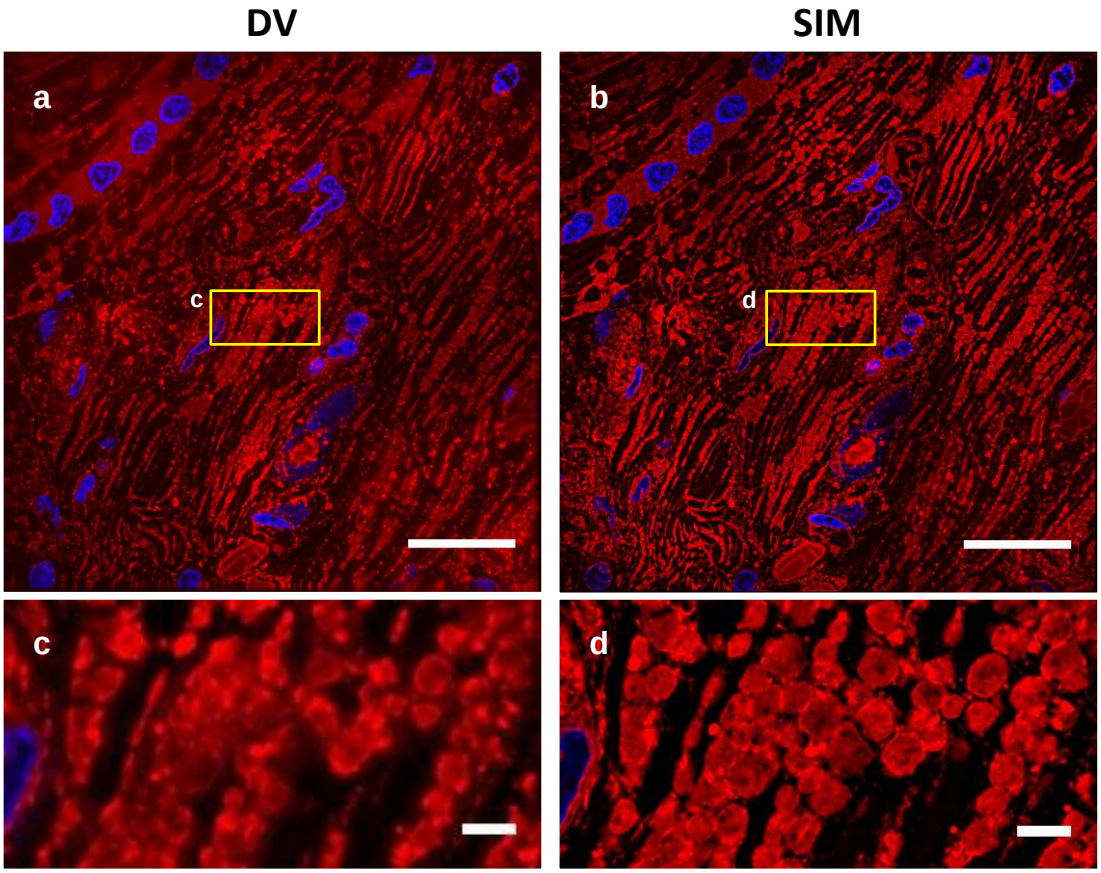

Figure 3.6. 3 × 3 tile mosaic of a 400 nm thick pig heart muscle cryo-section imaged on the OMX using a #1.5 coverslip as a substrate. Membranes in red and nuclei in blue. (a) DV image. (b) 3D-SIM image. (c)-(d) Magnified sections show contrast enhancement from SIM compared to DV. FOV (a)-(b) 100 × 100 μm. Scale bar (a)-(b) 20 μm, (c)-(d) 2 μm.

Figure 3.7 (a)-(b) shows a 5 × 5 tile mosaic of a 110 nm thick pig heart tissue cryo-section on a Si_3N_4 waveguide chip, imaged in DV and 3D-SIM, resulting in a total FOV of 150 × 150 μm. The magnified sections (c) and (d) reveal information that was not visible in the glass slide and the coverslip cases. 3D-SIM provides contrast enhancement, allowing for identification of subcellular structures such as muscle striations (S) and vesicles (V), in addition to the previously observed mitochondria (M).

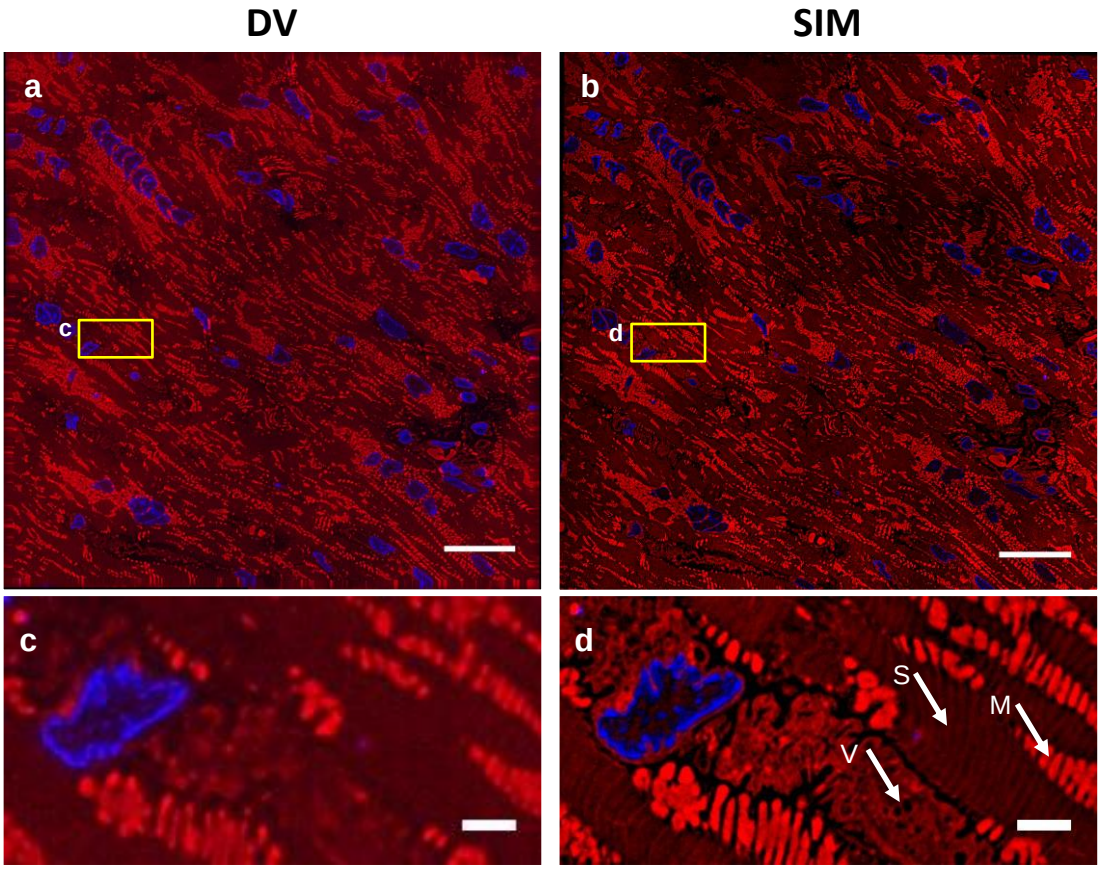

Figure 3.7. 5 × 5 tile mosaic of a 110 nm thick pig heart muscle cryo-section imaged on the OMX using a waveguide chip as a substrate. Membranes in red and nuclei in blue. (a) DV image. (b) 3D-SIM image. (c) Magnified section shows poor contrast in DV mode as compared to (d) SIM mode, which allows for identification of multiple subcellular features, including muscle striations (S), vesicles (V) and mitochondria (M). FOV (a)-(b) 150 × 150 μm. Scale bar (a)-(b) 20 μm, (c)-(d) 2 μm.

3.1.2 Challenges with imaging cryo-sections on the OMX

The main challenges associated with the successful super-resolution imaging of cryo-sections on the OMX were related to the sample preparation and the imaging conditions. This section discusses these challenges and offers practical ways to solve them.

On the sample preparation side, two problems were noticed:

1) Transparency: ultrathin cryo-sections (<500 nm) appear transparent to the human eye, making it difficult to handle them during the staining process. With few occasions the samples have detached from the substrate during the washing steps, without noticing it. The staining protocol was conveniently optimized to circumvent this problem, advising poly-L-lysine coating of the sample's substrate and the use of absorbent paper for the washing steps (see Appendix B).

2) Structural damage: tissue morphology was sometimes severely damaged during sectioning, in form of tearing, or after sectioning and laying on the substrate, in form of folds. Large FOV fluorescence images in Figure 3.8 (a)-(b) illustrate the above mentioned artifacts. To minimize these problems, the sample must be sectioned by a highly skilled technician under optimal environmental conditions. In addition, the ultramicrotome must be equipped with adequate sectioning tools (e.g. diamond knife).

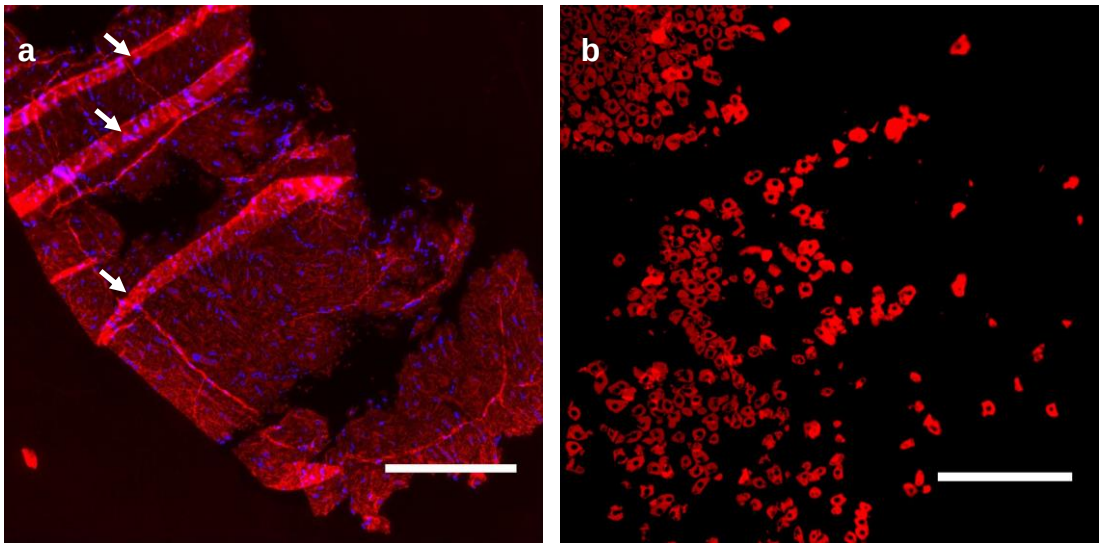

Figure 3.8. Sectioning artifacts on cryo-preserved samples. Fluorescent images with large FOV. (a) Pig heart muscle 70 nm thick cryo-section. Cell membranes in red, nuclei in blue. White arrows indicate the presence of folds during sectioning and laying on the substrate. (b) Rat liver 1000 nm thick cryo-section. Cell membranes in red. Sparse distribution of cells indicate tissue disrupture during sectioning. FOV (a)-(b) 800 × 800 μm. Scale bar (a)-(b) 200 μm.

On imaging side, four challenges were noticed, as discussed below:

1) Oil matching: no single emitters were observable in the orthogonal views of DV images, complicating the refractive index (RI) matching necessary for PSF optimization. Instead, the RI match was achieved by an iterative process of changing immersion oils until acceptable 3D-SIM images were obtained. Typical oil refractive

indexes used for SRM of cryo-sections in this study ranged from n = 1.514 to n = 1.518.

2) De-focus artifacts: tile mosaic images exhibited intensity variations along the scanned areas (e.g. Figure 3.5 and Figure 3.6). The phenomenon can be attributed to defocus of the sample induced by irregularities in the substrate (e.g. surface roughness). Two parameters play a key role in the formation of such artifact: axial resolution and sample thickness. The axial resolution of the high NA objective on the OMX is limited to approx. 500 nm. When imaging ultrathin cryo-sections, structural information from in-focus regions are collected and reconstructed as bright images, whereas slightly de-focused regions are collected and reconstructed as darker spots, resulting in tile mosaic images of non-uniform intensities. The photonic chip, made on ultra-flat silicon wafer helped to minimize this imaging artifact in two ways: (a) providing a flat surface substrate for the sample [58], and (b) serving as a reflective surface that increased the effective intensity of the excitation source, allowing for additional collection of fluorescent signal as compared to transparent substrates such as coverslips and glass slides.

3) Stitching artifacts: grid-like artifacts were observed on tile mosaic images generated by Fiji, in the form of dark bands in the overlapping regions. Figure 3.9 shows a 5 × 5 tile mosaic image of a heart muscle cryo-section containing a stitching artifact. White arrows indicate the direction of the overlapping band artifact. Further optimization of the stitching software and the overlapping steps are required to minimize this imaging artifact.

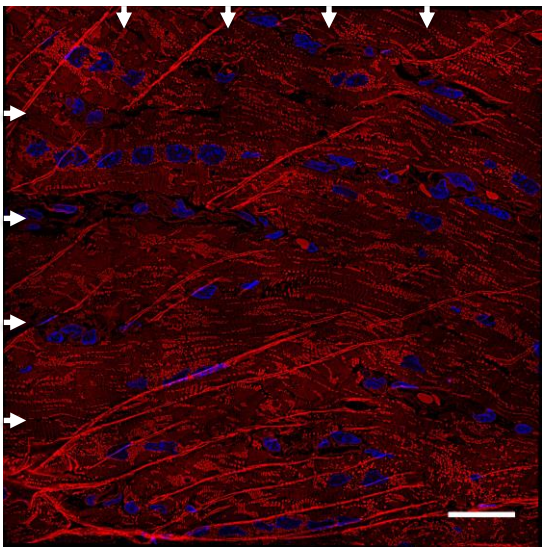

Figure 3.9. Stitching artifact. 5 × 5 tile mosaic of a 110 nm thick pig heart muscle cryo-section imaged on the OMX using a waveguide chip as a substrate. Cell membranes in red, nuclei in blue. White arrows show the direction of the grid-like stitching artifact which appears as dark bands in the image. FOV 150 × 150 μm. Scale bar 20 μm.

4) SIM artifacts: common SIM artifacts such as *hammerstroke* and *hatching* were observed in the reconstructed images of cryo-sections. Appendix C offers a brief overview of the imaging artifacts specific to SIM, as well as useful tips to avoid them.

3.1.3 Discussion: super-resolution imaging of cryo-sections

The results from the previous section show that SIM achieves super-resolution and high imaging contrast of ultrathin cryo-sections. Combined, these two properties of SIM help to visualize sub-cellular structures that are otherwise not visible using diffraction-limited techniques (e.g. DV). In addition, the sample preparation protocol of cryo-sections can be performed relatively quick, allowing for sectioning, staining and imaging within the same day. All in all, the easiness and rapidness to prepare and image cryo-sections to a resolution of approx. 120 nm gives SIM a temporal resolution advantage compared to traditional techniques used for similar resolution (e.g. EM), where the sample preparation alone can take up to two weeks.

Observation of projected SIM images shows that thinner samples (e.g. 70 nm, 110 nm) exhibit better contrast and resolution that those of thicker tissue sections (e.g. 300 nm, 400 nm, 1000 nm). However, the analysis of single 2D images from z-stacks of the latter allows for similar contrast and resolution results as for thin sections. This fact suggests the possibility of using z-stacks of thick cryo-sections (e.g. > 1000 nm) to create three-dimensional animations of the tissue, which can be used, for example, in the diagnosis of diseases or visualization of molecular expression. An example of a 3-D animation is shown in Appendix E.

The sample's substrate seems to play a significant role in the imaging results of cryosections. A comparison between Figure 3.10 (a)-(b)-(c) show that the waveguide chip allows for visualization of cardiac striations and vesicles that are otherwise not visible using microscope glass slide and coverslips as sample substrates. A possible explanation for this phenomenon is that the reflective surface of the chip increases the effective intensity of the excitation source, allowing for additional collection of fluorescent signal as compared to transparent substrates such as coverslips and glass slides. SIM images of the same cardiac tissue placed on two (2) microscope glass slides, five (5) #1.5 coverslips and two (2) waveguide chips validate this observation. The additional information gained using the waveguide chip as a substrate for the sample opens the door for biological studies and clinical applications. For example, the observation of vesicles in Figure 3.10 (c) allows for research of autophagy process in cardiac tissue.

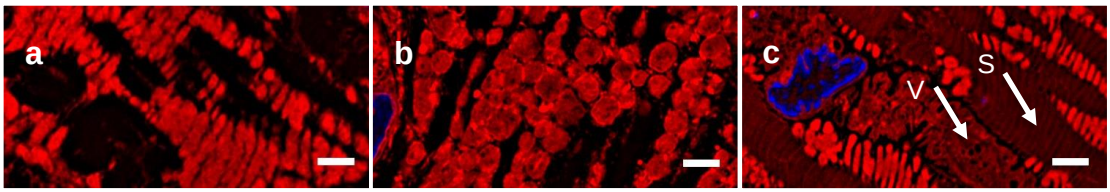

Figure 3.10. Magnified sections of 3D-SIM images of pig heart muscle cryo-sections imaged on the OMX using various substrates: (a) microscope glass slide. (b) #1.5 coverslip. (c) waveguide chip. Note that the waveguide chip allows for visualization of cardiac striations and vesicles that are otherwise not visible using microscope glass slide and coverslips as substrates. Scale bar (a)-(b)-(c) 2 μm.

Moreover, the flatness of the chip provides with better imaging results [58] in in cases where a series of images are required to compose a large FOV. Tile mosaic images show that the surface roughness of glass slides and coverslips, respectively, induce de-

focus artifacts, whereas the flatness of the chip allows for more uniform intensity across the tile mosaic images, as shown in Figure 3.7 and in Figure 3.29 (section 3.4.1).

The main drawback of imaging cryosections is the structural damage observed in almost all the samples, which makes it difficult for routine pathological studies, where observation of large FOV is required. Usual FOVs achievable on these samples is approx. 300 × 300 μm.

3.2 Study phase 1(b): FFPE sections on the OMX

This section is divided in three parts: 3.2.1) *imaging results*, offering an explanatory view of the collected images, 3.2.2) detailing the *challenges* associated with imaging FFPE sections on the OMX, and 3.2.3) an open *discussion* of the imaging results.

3.2.1 Imaging results

FFPE sections from human origin were imaged on the OMX: liver tissue and placental tissue. For convenience, the sample substrate chosen for these experiments was #1.5 coverslips. Table 5 offers a summary of the tissue sections and the substrates used this phase of the study.

Tissue type	Origin species	Preservation	Thickness (μm)	Substrate
Liver	Human	FFPE	4	#1.5 coverslip
Placenta	Human	FFPE	4	#1.5 coverslip

Table 5. FFPE sections imaged on the OMX.

3.2.1.1 FFPE human liver tissue sections

Human liver FFPE sections of 4 μm thickness, mounted on #1.5 poly-L-lysine coated coverslips, were imaged on the OMX in the DV and 3D-SIM modes. The samples were stained according to ref. #2 in Table 2. Three excitation sources were used for imaging, namely, 568 nm for membranes (CMO), 488 nm for LSEC marker (AF488) and 405 nm for nuclei (DAPI).

Figure 3.11 (a)-(b) show a 4 μm thick human liver tissue imaged in DV and SIM modes, respectively. Images correspond to 1.5 μm thick z-stack projections. Membranes are shown in red color, nuclei in blue, and LSECs in green. Both DV and 3D-SIM images show the expected morphology of the liver tissue shown in Figure 2.1 (B), with the LSECs (L) lining the sinusoids (S), and hepatocytes (H) with cuboidal geometry. In addition, the images show a red blood cell (RBC) inside the sinusoid. Both imaging modalities exhibit autofluorescent signal, although more prominently in DV than in SIM. White arrows on Figure 3.11 (a)-(c) show the presence of autofluorescent structures in the tissue, including a red blood cell (RCB). Two types of artifacts are found in the reconstructed SIM image. White arrows on Figure 3.11 (b)-(d) show haloing and hammerstroke artifacts, respectively. An explanation of these artifacts can be found in Appendix C. Further discussion of these imaging artifacts is offered in section 3.2.3.

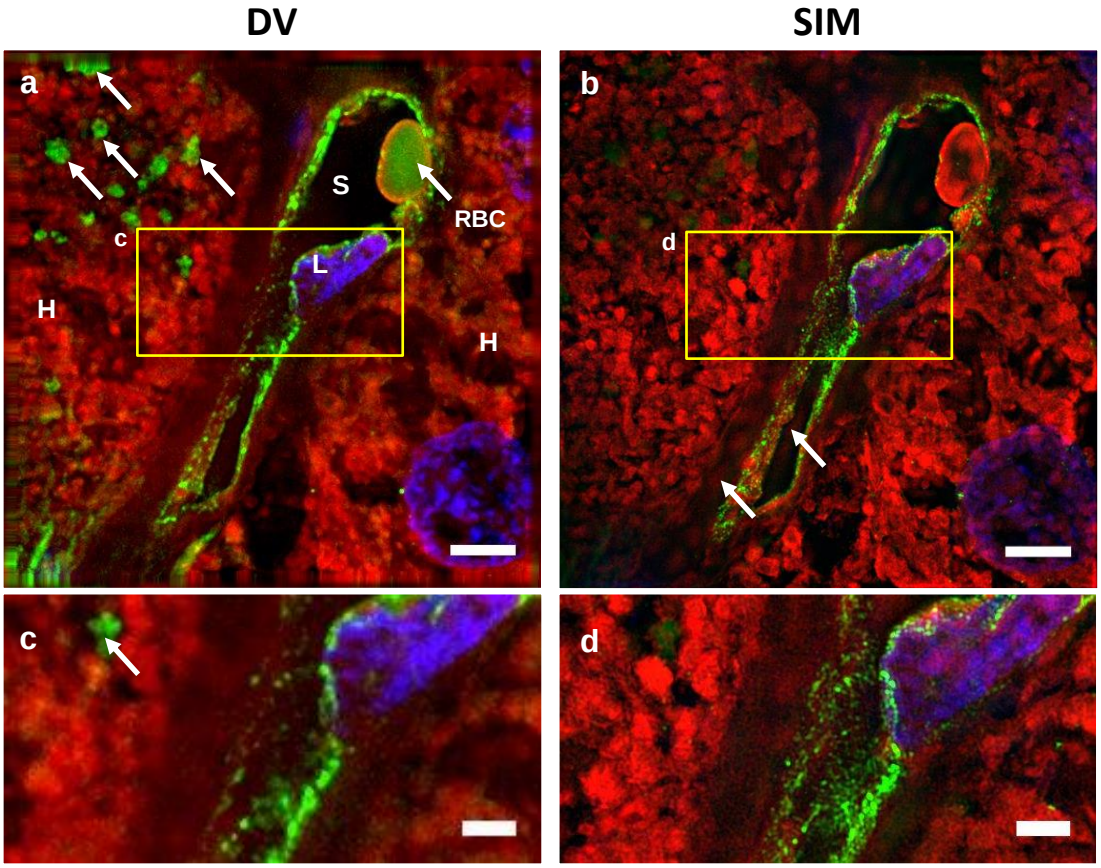

Figure 3.11. Human liver FFPE section 4 μm thick imaged on the OMX using a #1.5 coverslip as a substrate. Membranes in red, LSECs in green, and nuclei in blue. (a)-(b) 1.5 μm thick z-stack projected DV and SIM images, respectively, showing a LSEC (L) lining a sinusoid (S) that contains a red blood cell (RBC). Hepatocytes (H) surround the sinusoid. (c)-(d) Magnified sections show poor contrast in DV mode compared to 3D-SIM mode. White arrows on (a)-(c) show autofluorescent structures in the tissue, including the red blood cell (RCB), which are more prominent in DV than in SIM. White arrows on (b) show haloing and hammerstroke artifacts in the reconstructed SIM image. FOV (a)-(b) 40 × 40 μm. Scale bar (a)-(b) 5 μm, (c)-(d) 2 μm.

Figure 3.12 shows single z-sections views from the same z-stack of Figure 3.11. The contrast enhancement achieved by SIM (b)-(d) allows for observation of subcellular features that are not seen in the DV image (a)-(c).

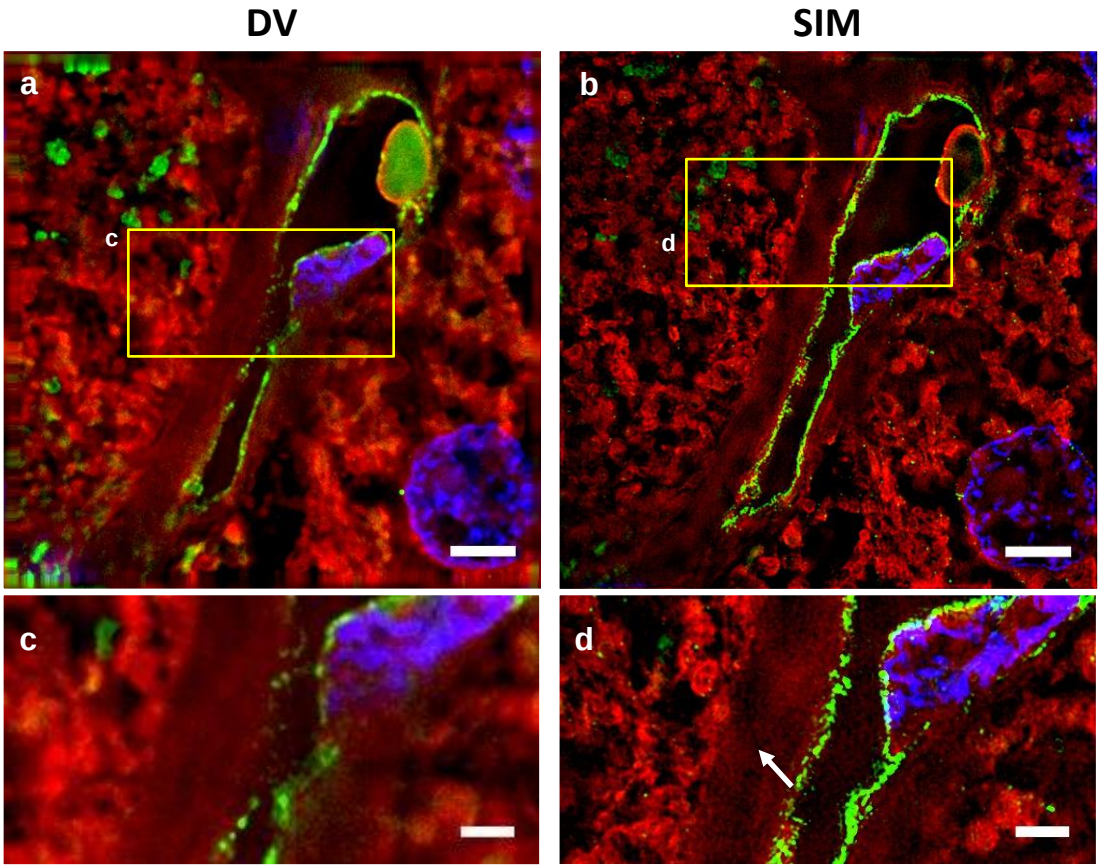

Figure 3.12. Human liver FFPE section 4 μm thick imaged on the OMX using a #1.5 coverslip as a substrate. Membranes in red, LSECs in green and nuclei in blue. (a)-(b) single z-section DV and SIM images, respectively. (c)-(d) Magnified sections show better contrast in SIM mode compared to DV. White arrow on (b) indicates the presence of hammerstroke artifacts. FOV (a)-(b) 40 × 40 μm. Scale bar (a)-(b) 5 μm, (c)-(d) 2 μm.

3.2.1.2 FFPE human placental tissue section

FFPE human placental sections of 4 μm thickness, mounted on #1.5 poly-L-lysine coated coverslips, were imaged on the OMX in the DV and 3D-SIM modes. The samples were stained according to ref. #3 in Table 2. Two excitation sources were used for imaging, namely, 568 nm for membranes (CMO) and 405 nm for nuclei (DAPI).

Figure 3.13 (a)-(b) shows a 5 × 3 tile mosaic of a 4 μm thick human placental tissue imaged in DV and SIM modes, respectively, with a total FOV of 100 × 160 μm (height × width). Images correspond to 1 μm thick z-stack projections. Membranes are shown in red and nuclei in blue. The arrangement of syncytiotrophoblasts (SYN) form a chorionic villus, which contain fetal red blood cells (f-RBC) within a fetal capillary. Maternal red blood cells (m-RBC) are found outside the chorionic villi. These observations correspond to the anatomy of the placenta presented in Figure 2.2 (B).

Magnified views in Figure 3.13 show contrast and resolution improvement in 3D-SIM (d) compared to DV (c). Magnified views in Figure 3.13 (e)-(f) show single z-section images from the z-stack, allowing for observation of morphological features in the tissue sample.

Common reconstruction artifacts observed when imaging FFPE placental tissues in SIM mode include honeycomb, hammerstroke and haloing, although significantly less prominent than in FFPE liver tissue, for the two excitation wavelengths used in the experiment. However, FFPE placental tissue exhibited strong autofluorescence upon excitation with blue light (λ = 488 nm). Next section offers an overview of the autofluorescence behavior of FFPE tissue sections.

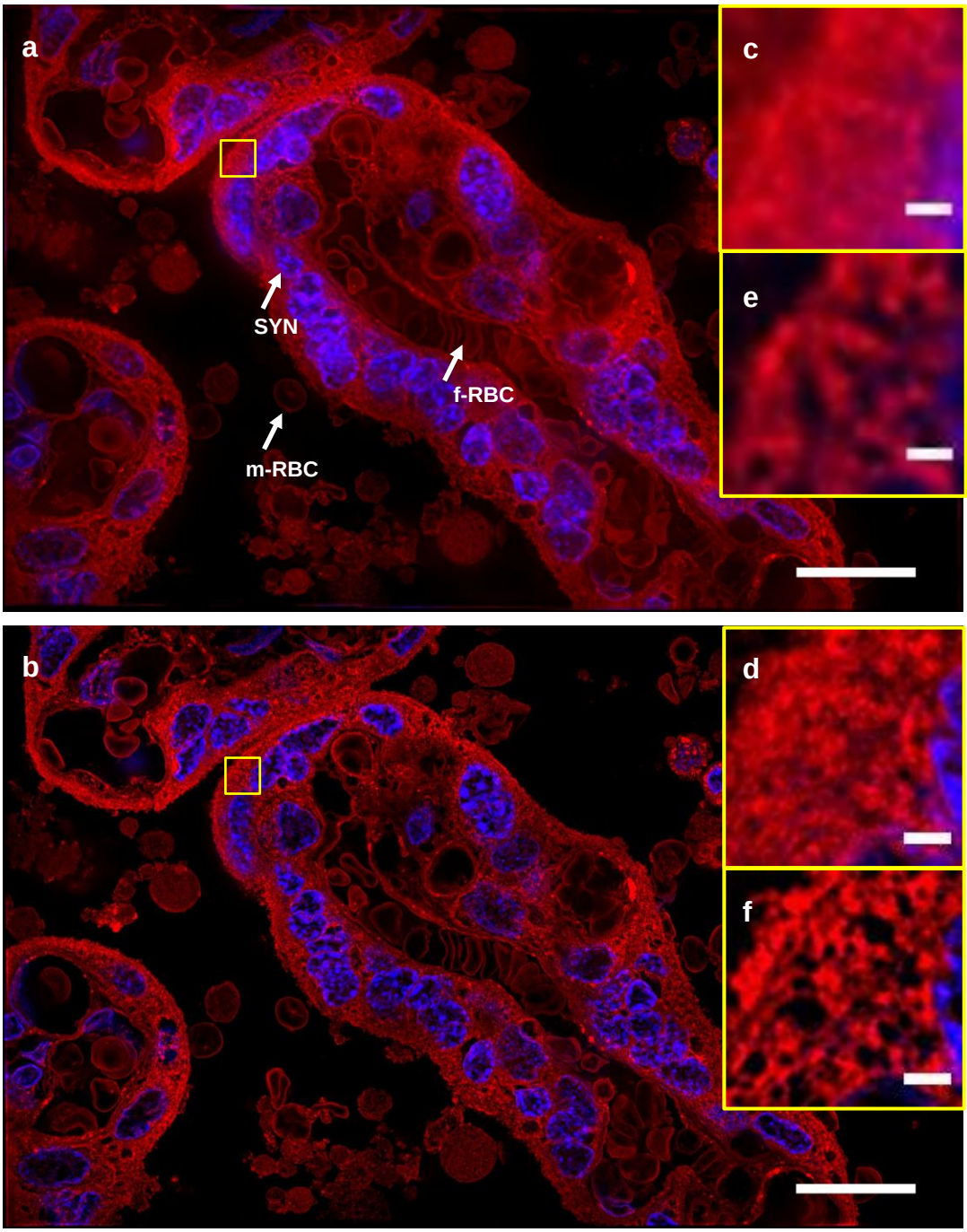

Figure 3.13. 5 × 3 tile mosaic image of a 4 μm thick human placental FFPE tissue imaged on the OMX using a #1.5 coverslip as a substrate. Membranes in red and nuclei in blue. (a) DV image. (b) 3D-SIM image. (c)-(d) Magnified sections show better contrast in SIM mode compared to DV. (e)-(f) single z-section images from the z-stack allow for visualization of morphological features in the tissue section. FOV (a)-(b) 100×160 μm (H × W). Scale bar (a)-(b) 20 μm, (c)-(d)-(e)-(f) 1 μm.

3.2.2 Challenges with imaging FFPE-sections on the OMX

A significant amount of time was spent during this master project to optimize the sample preparation methods to solve the below listed challenges:

1) Autofluorescence: the main challenge on this phase of the master project was autofluorescence, a phenomenon that refers to the ability of certain structures to fluoresce by natural means or by chemical changes induced through fixation. Autofluorescent particles exhibit a broad emission spectrum, making it difficult to separate their signal from that of fluorescent dyes in the experiment. Signal contribution from autofluorescence leads to reconstruction artifacts in SIM such as haloing and high-frequency noise (explained in Appendix C), hampering the resolution capabilities of this technique. The effect is more prominent in conventional fluorescence microscopy (e.g. DV), as illustrated in section 3.2.1.1. Diverse methods exist to reduce autofluorescence of histological samples, ranging from irradiation of light [59], to a series of chemical treatments [60-63]. The chosen method for autofluorescence reduction in this master project consisted of a 30 min incubation step in 150mM glycine solution after rehydration of the tissue sections. For autofluorescence characterization, FFPE sections were label-free prepared and imaged in DV mode on the OMX. All channels were set to 50% excitation intensity and 50ms acquisition time. Autofluorescence response of FFPE tissue sections is illustrated on Figure 3.14 and Figure 3.15. The mean and maximum gray values on Table 6 and Table 7 show broad autofluorescence response in both FFPE human liver and placental tissue sections, with a peak on channel 3, corresponding to wavelength excitation λ = 488 nm. Significant autofluorescent contribution in these samples came from red blood cells (RBCs), known to contain an autofluorescent substance called hemoglobin (Figure 3.15) [64].

2) Oil matching: the second challenge faced with FFPE sections was oil matching, which was addressed by an iterative oil change process, as explained in section 3.1.2. An alternative solution for this challenge was implemented on approx. three (3) FFPE sections, which consisted of adding fluorescent beads in the vicinity of the tissue section during sample preparation and use them as single emitters for oil matching (not shown). However, this method should be used with care, as the fluorescent signal of the beads could interfere with that of the dyes on the sample, leading to false positive results interpretation.

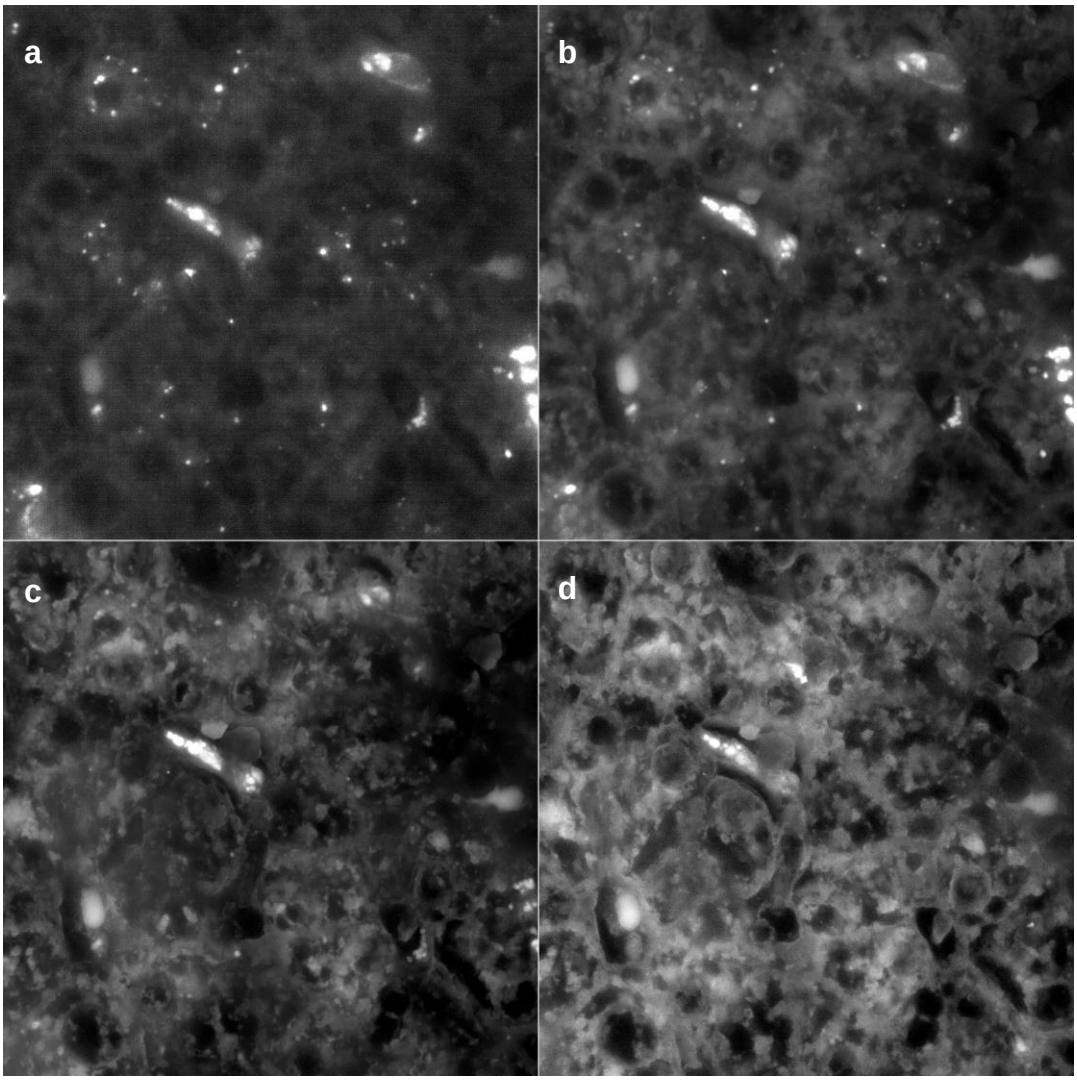

Figure 3.14. Autofluorescence of FFPE human liver tissue section. DV projection of 1 μm z-stack section. Excitation intensity 50%, exposure time 50ms. Grayscale images show autofluorescent signal upon illumination with (a) red light (λ = 642 nm), (b) green light (λ = 568 nm), (c) blue light (λ = 488 nm), and (d) violet light (λ = 405 nm). Bright areas indicate elevated autofluorescent signal. FOV (a)-(b)-(c)-(d) 80 × 80 μm.

Channel	Excitation wavelength (nm)	Intensity (%)	Exposure time (ms)	Gray value count			
				Min	Max	Mean	StdDev
CH1	642	50	50	103	1142	161	26
CH2	568	50	50	552	3152	895	143
CH3	488	50	50	3231	11022	4635	515
CH4	405	50	50	1136	3031	1691	182

Table 6. Imaging parameters and autofluorescence values of FFPE human liver tissue section.

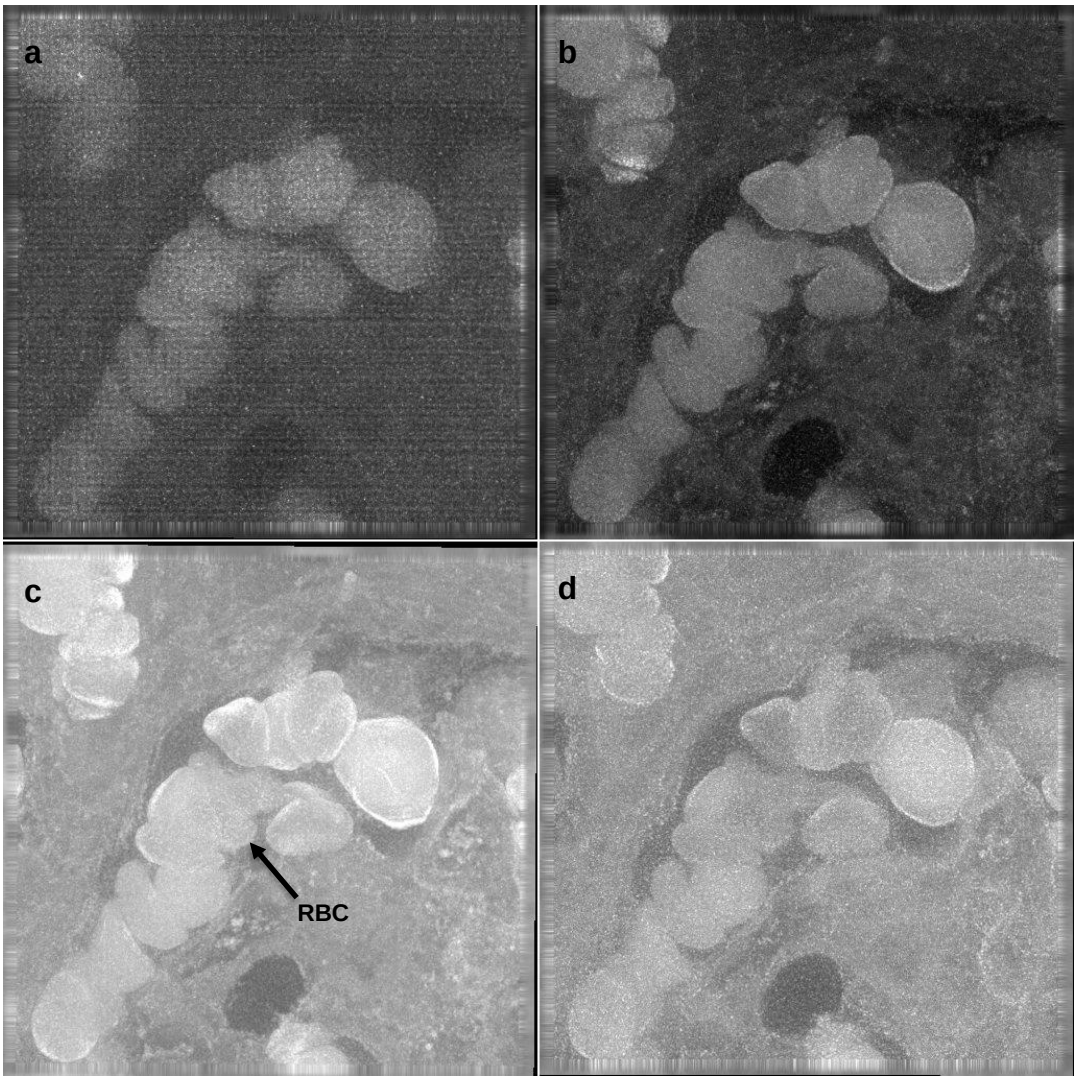

Figure 3.15. Autofluorescence of FFPE human placental tissue section. DV projection of 1 μm z-stack section. Excitation intensity 50%, exposure time 50ms. Grayscale images show autofluorescent signal upon illumination with (a) red light (λ = 642 nm), (b) green light (λ = 568 nm), (c) blue light (λ = 488 nm), and (d) violet light (λ = 405 nm). Bright areas indicate elevated autofluorescent signal, in this case corresponding to autofluorescence of RBCs. FOV (a)-(b)-(c)-(d) 80 × 80 μm.

Channel	Excitation wavelength (nm)	Intensity (%)	Exposure time (ms)	Gray value count			
				Min	Max	Mean	StdDev
CH1	642	50	50	0	647	209	58
CH2	568	50	50	437	2989	1151	299
CH3	488	50	50	0	8596	4875	901
CH4	405	50	50	0	2190	1294	165

Table 7. Imaging parameters and autofluorescence values of FFPE human placental tissue section.

3.2.3 Discussion: super-resolution imaging of FFPE sections

An important advantage of FFPE sections over cryo-preserved tissues observed in this study was the morphological preservation of the tissue upon sectioning. A comparison between imaging results in sections 3.1.1 and 3.2.1 indicates that FFPE sections could be more adequate than cryo-sections for histological studies that require observation of large FOVs. However, the autofluorescent signal observed in FFPE tissue sections induced reconstruction artifacts in the SIM images that hampered the resolution of this technique, not allowing for clear observation of sub-cellular organelles as in cryo-sections. The autofluorescent problem was more prominent in the liver tissue than in the placenta, which suggests that liver tissue cryo-sections could be a better option for super resolution imaging of this type of tissue than FFPE sections.

The imaging results in section 3.2.1 show that the main contribution of SIM on FFPE samples is not super-resolution, but contrast enhancement. This feature is particularly useful in histopathological studies that require observation of large FOVs. A recent study [50] has demonstrated the advantage of SIM for diagnosis of nephrotic syndrome (minimal change disease) using FFPE kidney tissue sections. The study indicates that SIM can achieve higher imaging throughput and better results than those of traditional diagnostic methods such as transmission electron microscopy (TEM), for a fraction of the cost, and suggests the possibility of image segmentation for automated computational analysis.

Reducing and controlling autofluorescence of FFPE liver and placental tissue sections is a challenge needed to be addressed in further studies. Meanwhile, it is convenient to avoid fluorescent dyes with excitation at 488 nm wavelength when planning experiments on such types of samples. Alternatively, SIM could be used for identification of autofluorescent structures in FFPE tissue sections, as illustrated in two recent studies of autofluorescent particles in eye retina tissue [47, 48].

Mitigating reconstructions artifacts of FFPE samples also requires further research. Despite the oil matching helped to reduce the haloing artifacts on the reconstructed SIM images, the methods used in this master project did not help to fully avoid autofluorescent-induced artifacts such as honeycomb and hammerstroke. However, these two imaging artifacts appeared imperceptible upon observation of large FOV images such as the placental tissue in Figure 3.13 (b).

3.3 Study phase 2(a-b): tissue sections on photonic chip

This section is divided in three parts: 3.3.1) *imaging results*, offering an explanatory view of the collected images, 3.3.2) detailing the *challenges* associated with imaging FFPE and cryo-sections on the waveguide chip-based setup, and 3.3.3) an open *discussion* of the imaging results.

3.3.1 Imaging results

Cryo-preserved sections and FFPE sections from human and non-human origin were imaged on the waveguide chip-based setup: pig heart muscle and human liver tissue. The sample substrate chosen for these experiments was a poly-L-lysine coated photonic chip containing 150 nm thick uncladded Si_3N_4 strip waveguides of various widths (200 μm, 320 μm, 400 μm, 600 μm and 1000 μm). Table 8 offers a summary of the tissue sections and the substrate used this phase of the study.

Tissue type	Origin species	Preservation	Thickness	Substrate
Cardiac	Pig	Cryo	110 nm	uncladded Si_3N_4 strip waveguide chip
Liver	Human	FFPE	4 μm	uncladded Si_3N_4 strip waveguide chip

Table 8. FFPE sections imaged on the OMX.

3.3.1.1 Pig heart muscle cryo-sections

Diffraction-limited TIRF mode images of 110 nm thick pig heart muscle cryo-sections were acquired the waveguide chip-based microscopy setup. After sectioning, tissue sections were placed on top of the waveguide chip as shown in Figure 3.16 (a). The samples were stained with dyes listed on ref. #5 in Table 2. After mounting, the coverslip edges were sealed with Picodent Twinsil (Figure 3.16 (b)) and pressed with a 200g weight for 30 min to reduce the gap between tissue section and coverslip (Figure 3.16 (c)). Imaging acquisition was performed in incremental magnification steps. First, a 4x/NA0.10 objective was used to localize the sample, optimize excitation source coupling, and to acquire diffraction-limited TIRF images. Then, a 25x/NA0.85 water-immersion objective was used to acquire higher resolution images. Finally, a 60x/NA1.2 water-immersion objective was used for the highest (diffraction-limited) resolution (Figure 3.19). Two excitation sources were used for imaging, namely, 561 nm for membranes and 488 nm for nuclei.

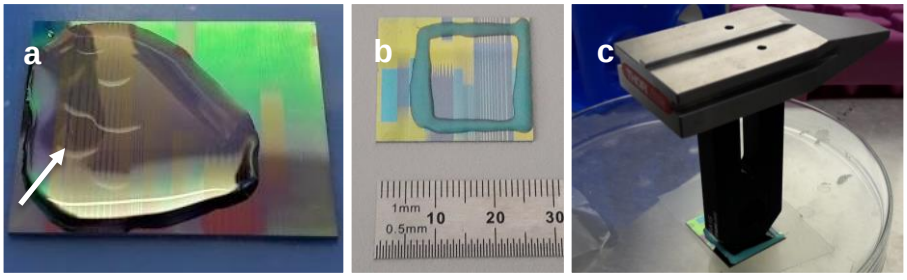

Figure 3.16. Pig heart muscle cryo-sections on top of a photonic chip. (a) White arrow indicates the location of 6 tissue sections. Straight lines on chip correspond to various waveguide widths for imaging. In this image, samples were incubated in PBS during preparation. (b) Edges of coverslip were sealed with Picodent Twinsil. (c) 200g weight was placed on top of the coverslip to reduce the gap between it and tissue sections.

Imaging results are presented as follows: Figure 3.17 shows 4x images of 2500 × 2500 µm FOV. Brightfield image (a) shows a tissue sample lying on a 320 µm wide waveguide (marked with arrowhead). Horizontally cropped TIRF image (b) reveals an intensity decay in the direction of propagation of the light, as a sign of absorption by the sample near the coupling facet of the waveguide (marked with black arrowheads). The white arrow in image (b) indicates absorption loses from residues (e.g. fluorescent dye) left on top of the waveguide chip after sample preparation. Figure 3.18 shows a 25x high-contrast TIRF image (a) that allows for visualization of the tissue section over a cropped FOV of 400 × 400 µm (usual FOV of the 25x/NA0.85 water-immersion objective lens is 500 × 500 µm). Figure 3.19 shows a 60x high-contrast TIRF image (a) with a narrow FOV of 220 × 220 µm that allows for morphological visualization of the tissue sample. Zoomed-in images correspond to same region on the sample. Figure 3.17 (c) reveals poor image resolution. Figure 3.18 (b) exhibits better contrast, but still insufficient resolution to visualize subcellular features other than nuclei (in blue). Figure 3.19 (b) provides better contrast and resolution, allowing visualization of subcellular structures such as mitochondria and muscle striations.

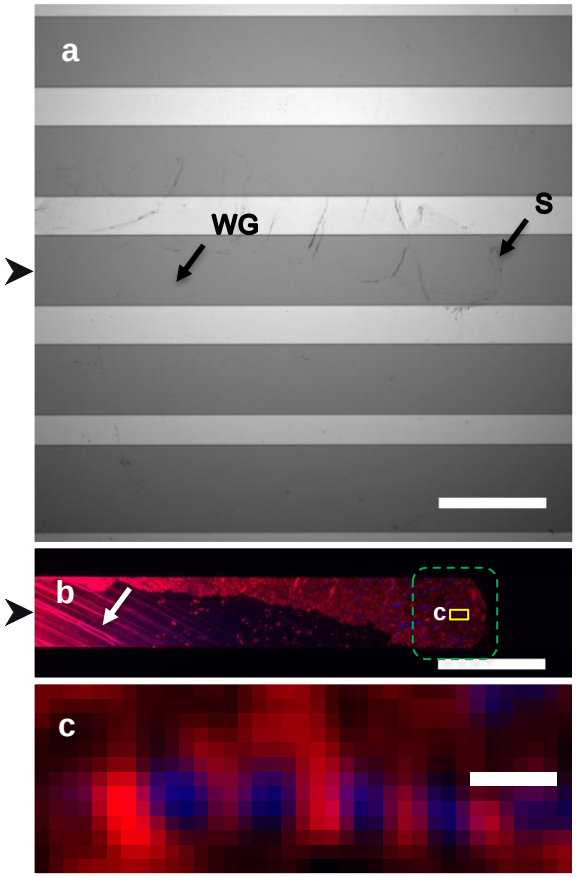

Figure 3.17. 4x magnification image of a 110 nm thick pig heart tissue cryo-section on a 320 µm width straight waveguide. (a) Brightfield image shows various strip waveguides (WG) in dark grey color and indicates the location of the semi-transparent sample (S). (b) horizontally cropped TIRF image shows membranes in red and nuclei in blue. Arrowhead indicates propagation direction of waveguides, left margin being approx. 100 µm away from the edge. Brightness variations reveal propagation losses near the coupling facet. White arrow indicates absorption loses from residues (e.g. fluorescent dye) on top of the waveguide chip after sample preparation. (c) Zoomed-in region reveals poor image contrast and resolution. Dotted line in green shows the region observed in Figure 3.18. FOV (a) 2500 × 2500 µm. Scalebar (a)-(b) 500 µm, (c) 10 µm.

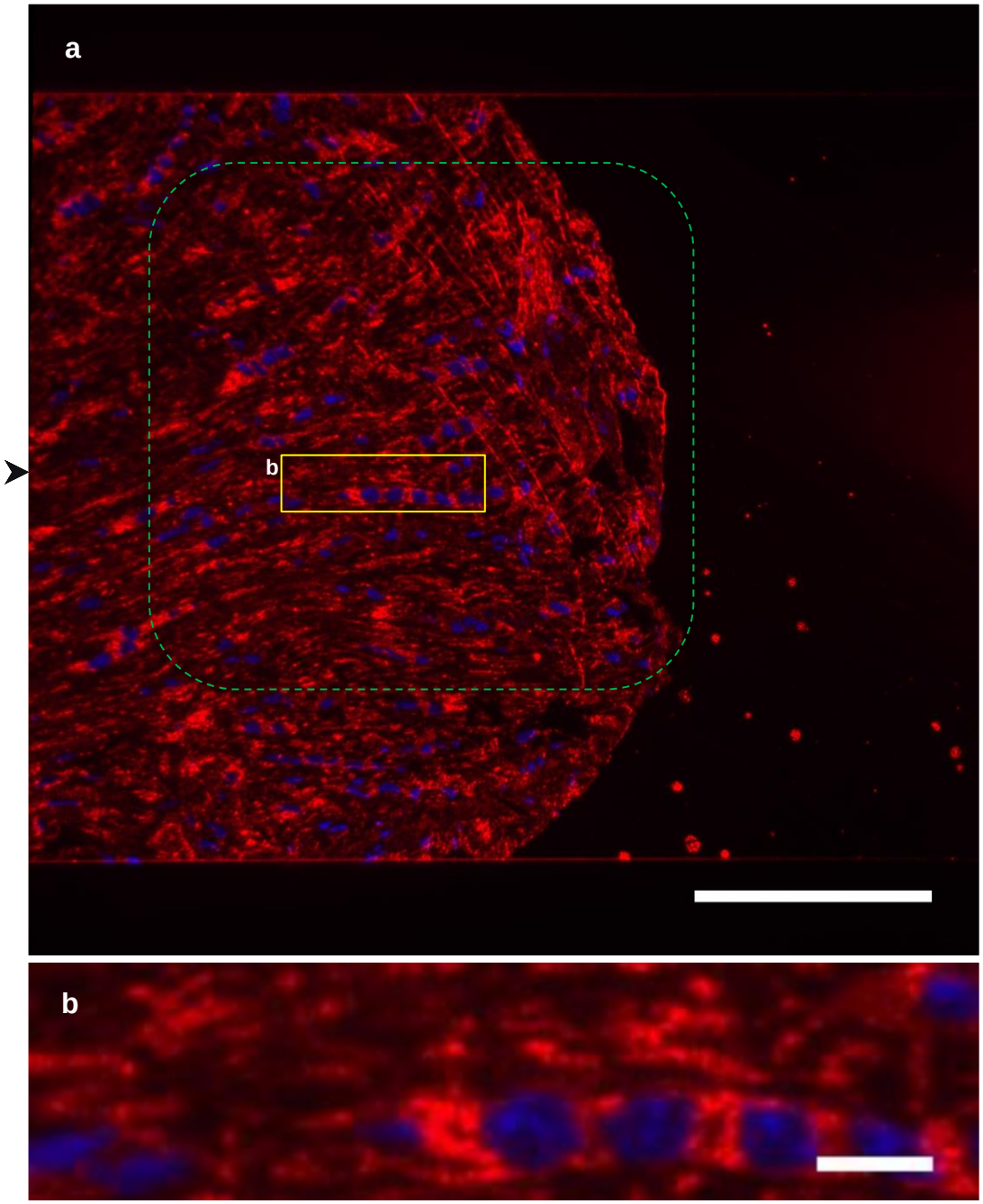

Figure 3.18. 25x magnification image of a 110 nm thick pig heart tissue cryo-section on a 320 μm width waveguide. (a) Diffraction-limited TIRF image allows for morphological visualization of the tissue section. Membranes in red and nuclei in blue. Arrowhead indicates the direction of propagation of the guided light. (b) Resolution of zoomed-in region is insufficient to distinguish subcellular features. Dotted line in green shows the region observed in Figure 3.19. FOV (a) 400 × 400 μm. Scale bar (a) 100 μm, (b) 10 μm.

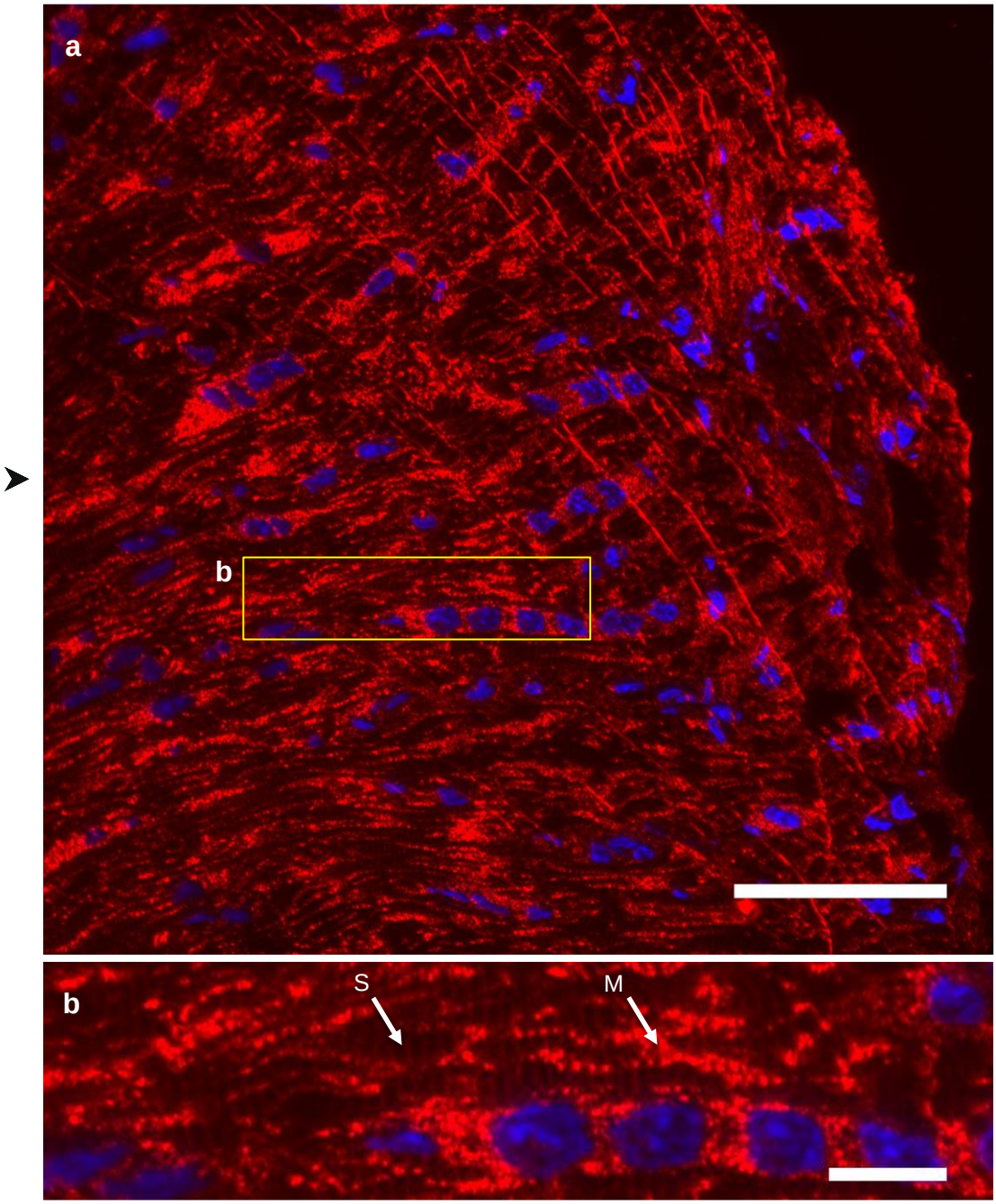

Figure 3.19. 60x magnification image of a 110 nm thick pig heart tissue cryo-section on a 320 μm wide waveguide. (a) Diffraction-limited TIRF image. Membranes in red and nuclei in blue. Arrowhead indicates the direction of propagation of the guided light. (b) Zoomed-in region reveals mitochondrial structures (M) and muscle striations (S). FOV (a) 220 × 220 μm. Scale bar (a) 50 μm, (b) 10 μm.

3.3.1.2 FFPE human liver tissue sections

Diffraction-limited TIRF mode images of 4 μm thick human liver FFPE sections were acquired on the chip-based microscopy setup. After sectioning, tissue sections were placed on top of the waveguide chip as illustrated in Figure 3.20. Samples were deparaffinized, rehydrated, bleached and stained according to the protocol in Appendix A. The stains used for the experiment are listed on ref# 6 in Table 2. The samples were mounted and sealed following the procedure explained in the previous section, including the use of the 200g weight to reduce the gap between the coverslip and the tissue section.

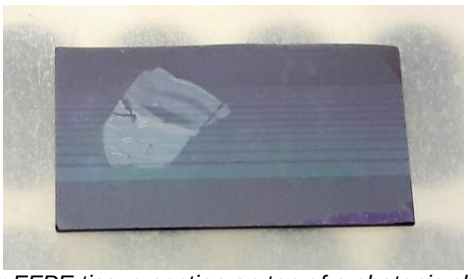

Figure 3.20. Human liver FFPE tissue section on top of a photonic chip. The straight lines on chip correspond to various waveguide widths for imaging. Chip size approx. 2.5 x 1.5 cm.

A 4x/NA0.10 objective was used to localize the sample and optimize excitation source coupling. Imaging acquisition was performed with a 20x/NA0.45 objective. Three excitation sources were used for imaging, namely 660 nm for LSECs, 561 nm for membranes and 488 nm for nuclei. Figure 3.21 (a) shows a 600 × 500 μm diffraction-limited TIRF image of the FFPE tissue section. An intensity decay is observable in the membrane signal (in red), indicating absorption losses along the direction of propagation of the light. White arrows indicate the presence of scattering spots inside the waveguide that create hotspot artifacts in the image. Low bleed-through of the three waveguides is observable at the periphery of the waveguide. Zoomed-in image (b) reveals the autofluorescence of RBCs inside the sinusoid lined by LSECs. The image matches the expected contrast enhancement for chip-based TIRF imaging. Attempts were made to image the sample with a higher NA objective lens (60x/NA1.2 water-immersion and 25x/NA0.85 water-immersion). However, sample placement close to the input edge leads to problems through the short working distance, bulky high NA imaging objectives colliding with the coupling optics.

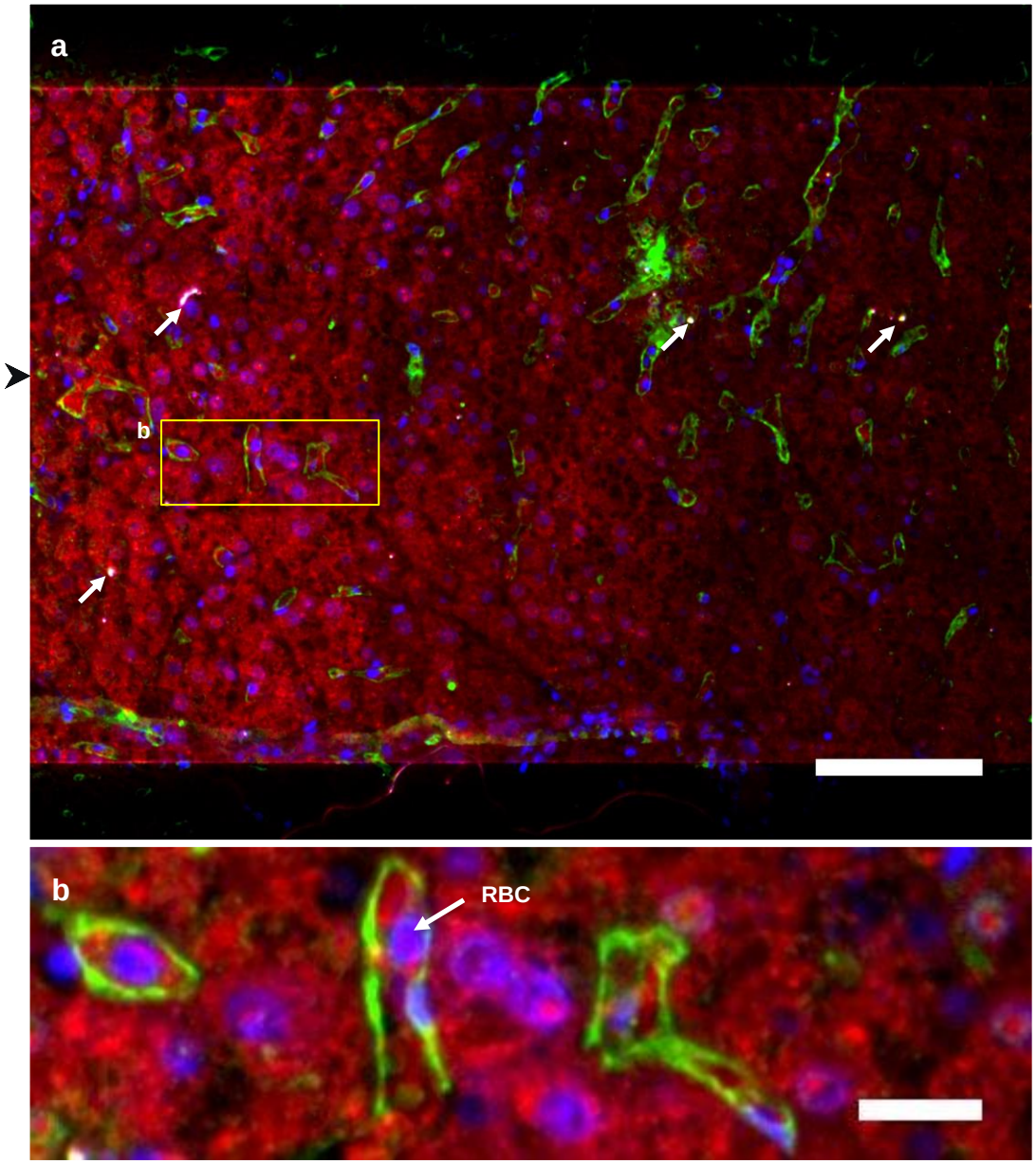

Figure 3.21. 20x magnification image of a 4 μm thick human liver tissue FFPE section on a 400 μm width waveguide. (a) Diffraction-limited TIRF image. Membranes in red, LSECs in green, and nuclei in blue. White arrows indicate scattering spots inside the waveguide. Low bleed-through of the three channels can be observed outside top and bottom limits of the waveguide. Arrowhead indicates the direction of propagation of the guided light. (b) The zoomed-in region reveals the autofluorescent signal from RBCs, intermixed with nuclei signal (in blue). FOV (a) 600 × 500 μm (W×H). Scale bar (a) 100 μm, (b) 20 μm.

3.3.2 Challenges with imaging tissue sections on chip

Both cryo-sections and FFPE sections demanded some effort for imaging in the chip-based microscopy setup. Challenges were encountered on this phase of the master project, which are presented below.

1) Light absorption: a common problem encountered on both types of samples was absorption loss near the coupling facet of the waveguides, observable as a gradual intensity decay in the direction of light propagation. In all cases, the phenomenon occurred after sample preparation, and it was significantly more prominent with the FFPE samples than with the cryo-sections. Propagation losses inherent to the waveguide occur at orders of magnitude below the ones observed after sample preparation. The latter can be attributed to fluorophores or absorption by the tissue. Certain chip configurations dispose of a top cladding layer that is present along the entire waveguide, except for the imaging area where the sample is in direct contact with the waveguide core. The uncladded topology of the chips used in this master project did not benefit from such a layer, with residues from sample preparation (e.g. fluorescent dyes, paraffin) absorbing most of the excitation light, few millimeters after the coupling facet. Once the guided light reached the tissue sample, it quickly decayed. To overcome this problem, the excitation power was increased until adequate fluorescent signal was obtained on the region of interest (ROI). Typical values are shown in Table 9. Available cladded chips were not used in this master project due to fabrication issues (excessive scattering spots in the waveguides). Future experiments will include this chip configuration for tissue imaging. Figure 3.22 illustrates a fluorescent image of residue on a chip after sample preparation of a cryo-section.

Excitation wavelength (nm)	Excitation power cryo/FFPE (mW)
488	10/80
561	70/200
660	50/300

Table 9. Wavelengths and excitation power used in the photonic setup.

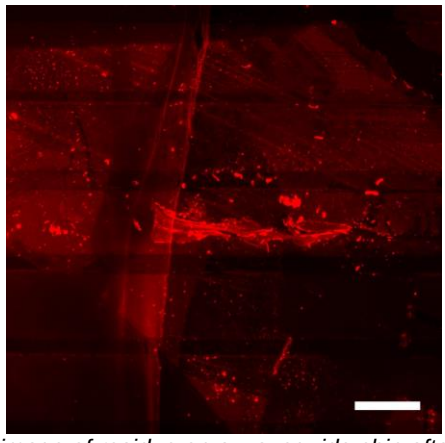

Figure 3.22. Fluorescent image of residue on a waveguide chip after sample preparation of a cryo-section. Imaging with TRITC filter sets. Scale bar 100 μm.

2) Picodent: the sealant agent used in the experiments, Picodent Twinsil, exhibited light absorption if crossing guiding waveguides. To avoid this challenge, the sealant was removed from the imaging structures.

3) Dimensional limitations: an indirect problem from light absorption by the samples was the necessity of using high NA lenses close to the input face of the chips. The emission decay occurred on the tissues made it necessary to bring the collection objective close to the coupling facet. The bulky dimensions of the high NA lenses used for collection limited this task, as they would collide with the excitation objective. Figure 3.23 illustrates this problem.

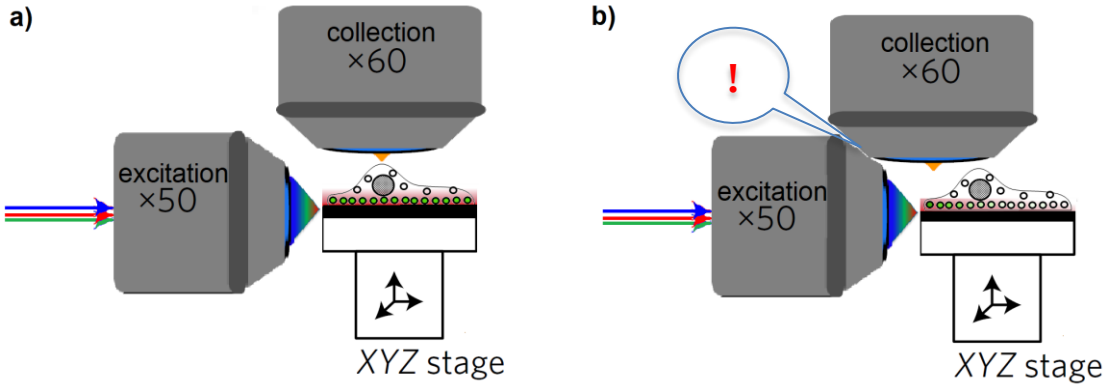

Figure 3.23. Dimensional limitations of the waveguide chip-based microscopy setup. (a) in an ideal scenario, light propagates uniformly across the waveguide creating an evanescent field that excites the fluorophores on the surface of the chip. (b) upon absorption loses, fluorescent signal of the sample can be only collected near the coupling facet of the chip. The bulky dimensions of the high NA collection objective limited this task, as it often collided with the excitation objective. Dimensions of the sample has been enlarged for illustration purposes.

4) Hotspots: Many waveguides used in this master project exhibited particles on the surface that acted as scattering spots of high fluorescence intensity, thus complicating the imaging process and introducing image artifacts. These fabrication issues were being sorted out during the duration of this master project. To ensure optimal imaging, a thorough cleaning and microscopic examination of the chip must be performed prior to the start of the experiments.

5) Bleed-through: FFPE exhibited some degree of bleed-through near the edges of the waveguides that was not observable on the cryo-sections. The phenomenon was more prominent at longer wavelengths (e.g. 660 nm, 561 nm) than at shorter ones (e.g. 488 nm). Three possible explanations can be attributed for such phenomenon:

a) Experimental error: such as unguided light hitting the sample;

b) Light coupling onto the coverslip: upon increase of the excitation power for adequate imaging, the unguided light couples onto the coverslip, generating an evanescent field on top of the sample that serves for TIRF illumination of areas of the sample in the periphery of the waveguide. This is due to the coupling beam being larger than the area of the waveguide mode. Simulations and experiments by other colleagues from the Optics Group in Tromsø have demonstrated a coupling efficiency of ca. 30% from the coupling objective to the waveguide with the components used in this work. Without careful optimization, it can be seen how the remaining light can couple onto the

coverslip. A potential solution for such problem is to place a stripe of black polydimethylsiloxane (PDMS) before the coverslip to prevent unguided light coupling.

c) Light propagation by the sample: the sample itself may propagate the light for short distance outside the periphery of the waveguide.

Due to time limitations, it was not possible to determine the exact cause of the bleed-through on FFPE tissue sections. Further studies are required to overcome this problem.

6) Autofluorescence: FFPE samples exhibited autofluorescence signal on short excitation wavelength (e.g. 488 nm), more prominently by RBCs. This is similar to the observations from the OMX.

3.3.3 Discussion: imaging tissue sections on the waveguide chip-based setup

The imaging results from section 3.3.1 demonstrate that, indeed, the waveguide chip can be used for the observation of FFPE and cryo-preserved tissue sections of various thicknesses. The possibility of TIRF illumination together with de-coupled excitation and collection light paths provides the chip-based microscopy an advantage compared to traditional TIRF microscopy setups, as different magnification objectives can be used for the collection of the fluorescent signal allowing for flexibility of FOVs of the sample, as recently demonstrated by members of the Optics Group in Tromsø [3, 31]. Histological studies could also benefit from this property, since the low-magnification wide-FOV objectives could serve for low resolution imaging of the entire sample, e.g. for the localization of histological structures, whilst the high-magnification (high NA) low-FOV objectives could be used for high resolution imaging of the ROIs. Moreover, the optical sectioning and high-contrast observed in the diffraction-limited images of tissue sections, particularly in the cryo-sections acquired on the waveguide chip-based microscopy setup, points out the possibility of performing SRM studies on these types of samples. For this purpose, three alternative methods can be explored: SMLM, fluctuation-based analysis (e.g. MUSICAL) and SIM. The first two options can be tested on the existing straight waveguide configurations, while the third option requires counter-propagating waveguide design to obtain the beam interference pattern necessary for SIM, currently under development by the Optics Group in Tromsø. Figure 3.24 shows three diffraction-limited TIRF images with different FOVs of a pig heart cryo-section imaged with different objectives.

The chosen configuration for the chips in this phase of the study was uncladded straight-waveguides of diverse widths (200 μm, 320 μm, 400 μm, 600 μm, 1000 μm). However, the wide FOV achievable with low-magnification objectives suggest the possibility of using different waveguide configurations for histological studies (e.g. 2500 μm width straight waveguides, slab waveguides). In addition, cladded configurations should be tested in the future to avoid light losses and ensure light propagation through the waveguide core until the opening containing the sample.

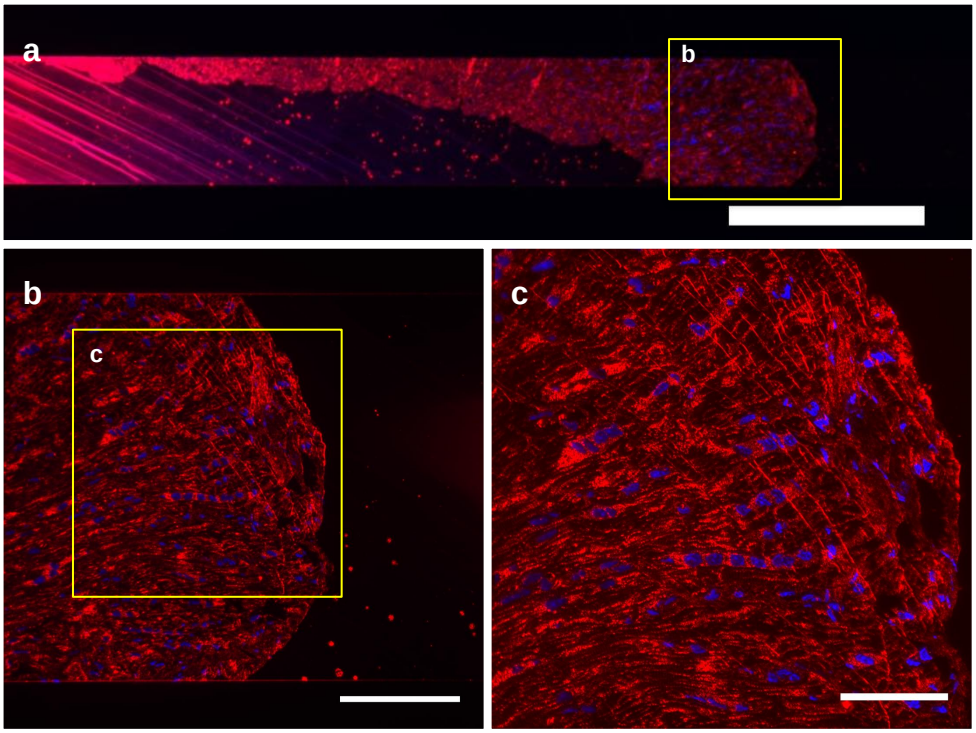

Figure 3.24. TIRF images of a 110 nm thick pig heart tissue cryo-section on a 320 μm width waveguide, collected with different magnification objectives. Membranes in red and nuclei in blue. (a) 4x objective allows for a total FOV of 2500 × 2500 μm. In this image, horizontally cropped to FOV 2500 × 500 μm (W x H). (b) 25x objective allows for FOV 500 × 500 μm. In this image, cropped to 400 × 400 μm. (c) 60x objective allows for FOV 220 × 220 μm.

Further research is necessary to avoid absorption loses on the FFPE tissue sections. One possible solution to be tested in further studies, is to prepare these samples (e.g. deparaffinize, rehydrate, bleach and stain) on a substrate such as a coverslip, and then mount them on a clean chip for imaging. Figure 3.25 illustrates this concept. A small weigh (approx. 200g) can be used to bring the sample to the surface of the chip, as required for TIRF microscopy.

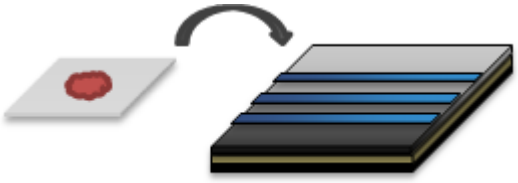

Figure 3.25. Illustration of a FFPE sample prepared in a coverslip and then mounted on a waveguide chip to avoid absorption loses during imaging.

3.4 Correlative light-light microscopy using chip and OMX

3.4.1 Cryo-sections

A complementary study was performed in this master project to observe and compare images from the two microscopy platforms of the study. A 110 nm thick pig heart muscle cryo-section was imaged on the OMX, both in DV and SIM modes, and then on the chip-based microscopy setup. Sample preparation was performed as explained on section 3.3.1, with an extra step to mount the chip on a glass slide to allow observation in the two platforms. Picodent Twinsil was used as adhesive medium for this purpose. To ensure light guiding on the waveguides, the propagating area was left uncovered of sealant, as illustrated on Figure 3.26. The stains used for sample preparation correspond to ref. #5 in Table 2. Two excitation sources were used for imaging on the OMX, namely 568 nm for membranes and 488 nm for nuclei. Similarly, excitation sources in the chip-based setup were 561 nm for membranes and 488 nm nuclei. Image acquisition was performed first on the OMX using a 60X/NA1.42 oil-immersion objective, and then on the chip-based setup with a 60X/NA1.2 water-immersion objective. Large FOV tile mosaics on the OMX were obtained by snake-like scanning and later post-processing (stitching) of the images. In total, nine (9) DV images with FOV of 80 × 80 μm were used to compose a tile mosaic DV image of 220 × 220 μm. Analogously, 25 SIM images were required for a 160 × 160 μm tile mosaic image. The large FOV provided by the chip-based setup allowed for acquisition of diffraction-limited TIRF images with FOV of approx. 220 × 220 μm. Acquisition and post-processing time required for the images was: approx. 3.5min for DV, approx. 30min for SIM, and approx. 50sec for chip.

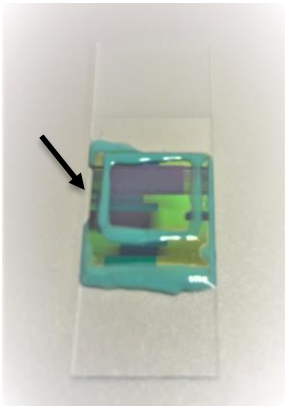

Figure 3.26. Waveguide chip mounted on a microscope glass slide for correlative imaging on the OMX and the chip-based setup. Black arrow indicates the location of the light coupling facet. Picodent crossing imaging waveguides was removed before imaging.

The imaging results are shown in the following order:

1) Diffraction-limited tile mosaic DV image (Figure 3.27)

2) Diffraction-limited TIRF image (Figure 3.28)

3) Super-resolved tile mosaic 3D-SIM image (Figure 3.29)

A comparative discussion is offered in section 3.4.2.

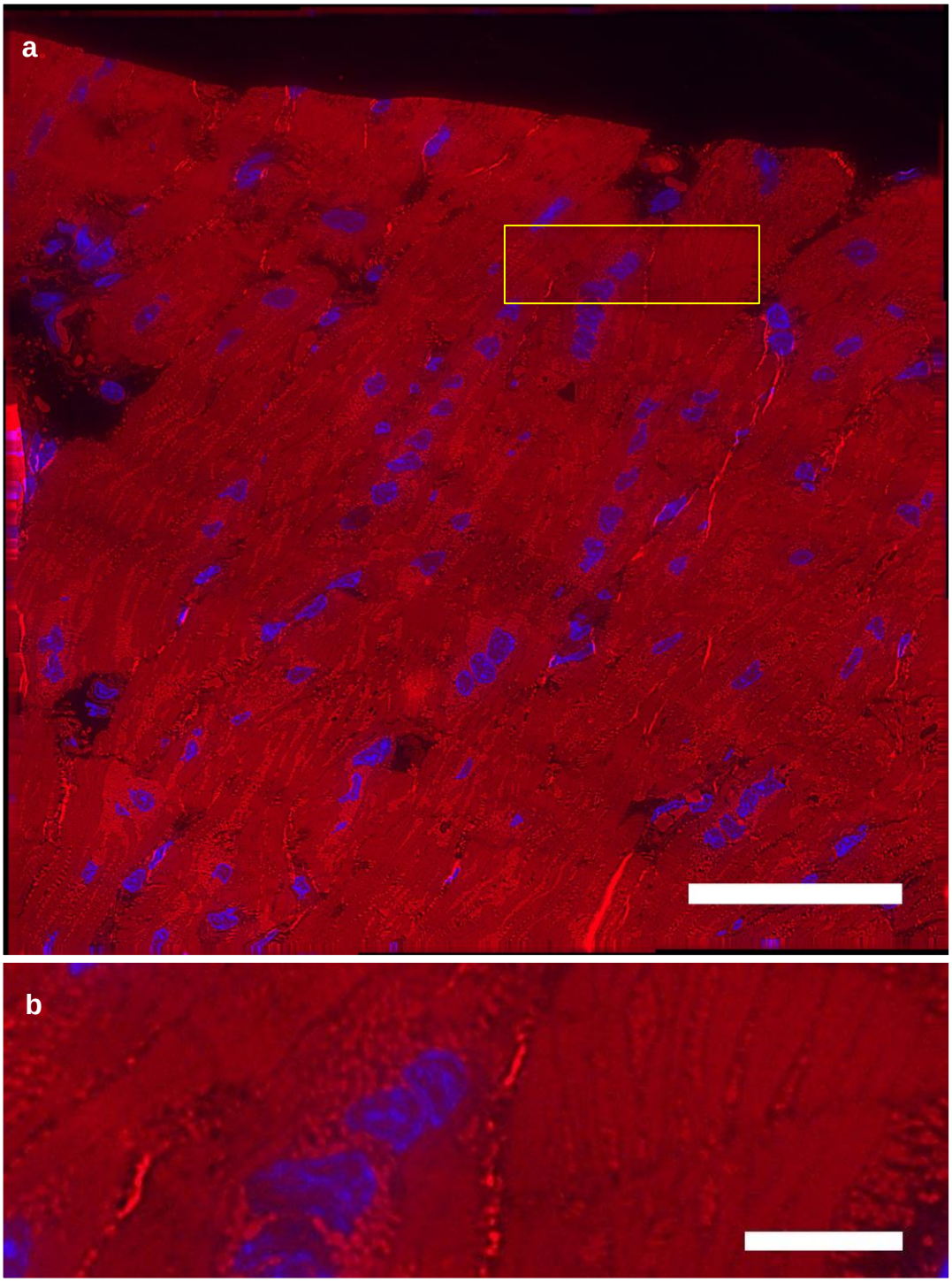

Figure 3.27. Wide FOV DV image of a 110 nm thick pig heart muscle cryo-section imaged on the OMX using a waveguide chip as a substrate. Membranes in red and nuclei in blue. (a) 9 × 9 tile mosaic DV image FOV 220 × 220 μm. (b) Zoomed-in region. Scale bar (a) 50 μm, (b) 10 μm.

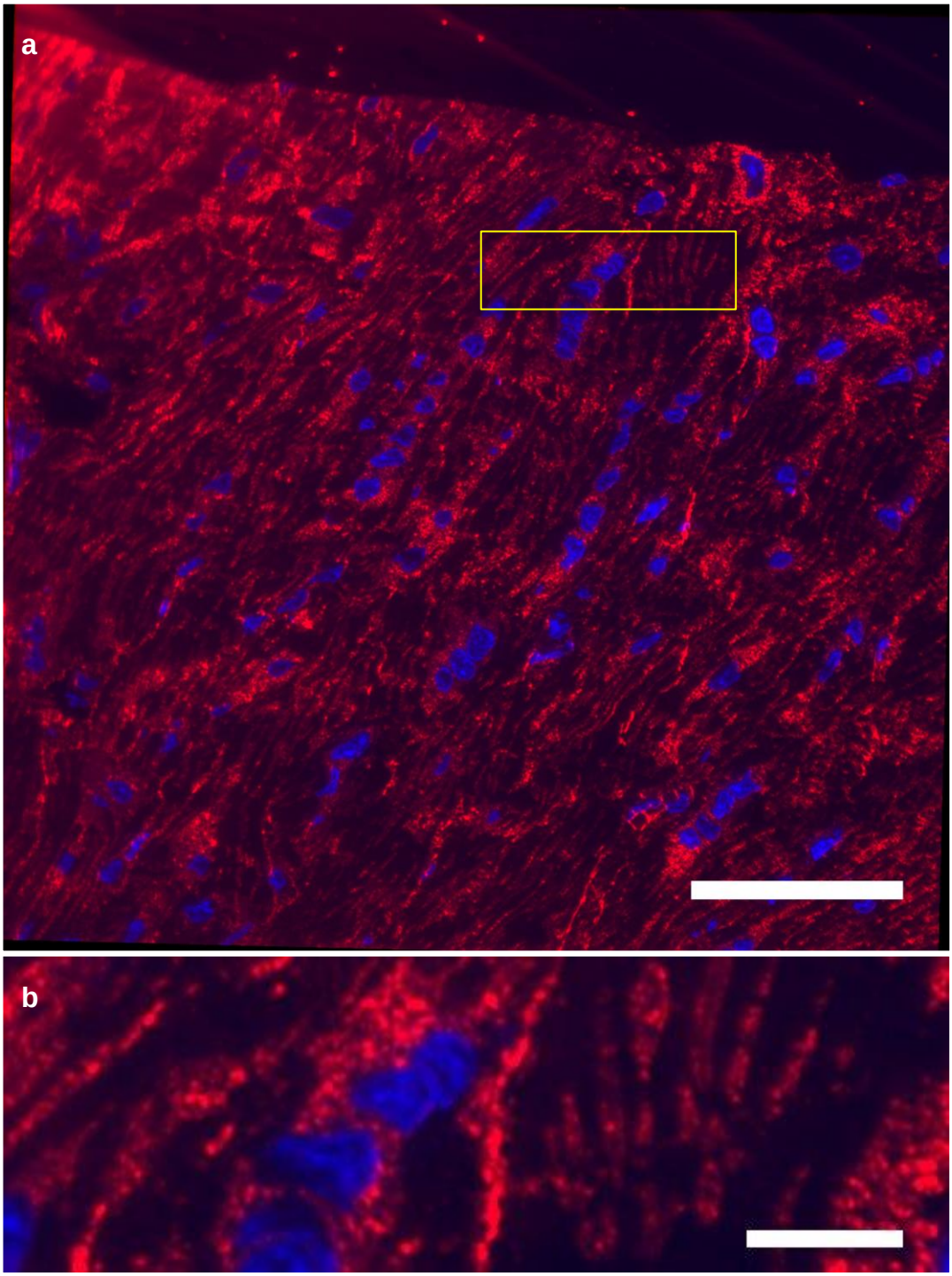

Figure 3.28. Wide FOV TIRF image of a 110 nm thick pig heart muscle cryo-section imaged on the waveguide chip-based microscopy setup using a waveguide chip as a substrate. Membranes in red and nuclei in blue. (a) TIRF image FOV 220 × 220 μm. (b) Zoomed-in region. Scale bar (a) 50 μm, (b) 10 μm.

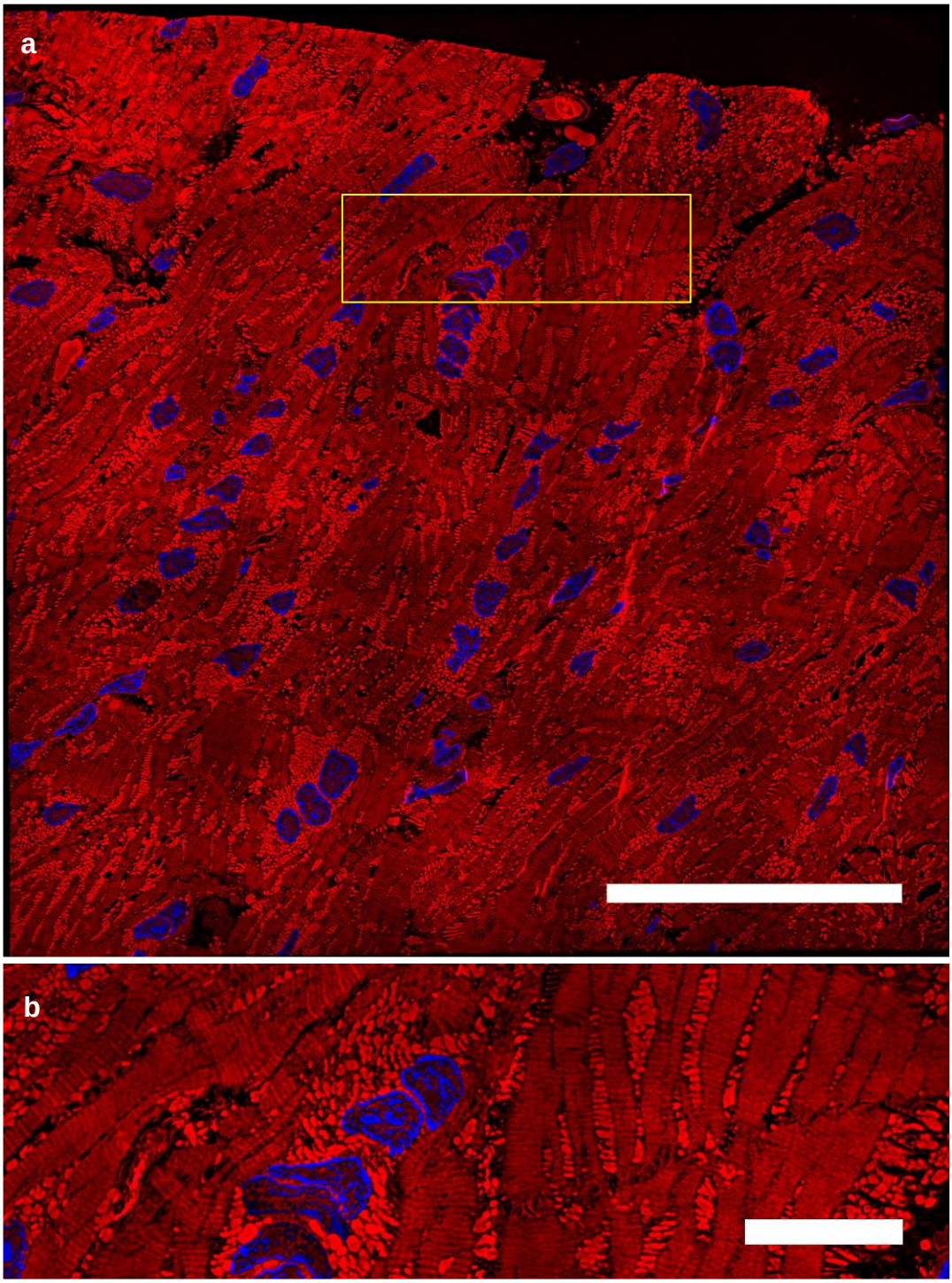

Figure 3.29. Wide FOV 3D-SIM image of a 110 nm thick pig heart muscle cryo-section imaged on the OMX using a waveguide chip as a substrate. Membranes in red and nuclei in blue. (a) 25 × 25 tile mosaic 3D-SIM image FOV 160 × 160 μm. (b) Zoomed-in region. Scale bar (a) 50 μm, (b) 10 μm.

3.4.2 Discussion correlative light-light microscopy

A comparison of the three imaging modalities used in this experiment reveals a significant difference between the TIRF image acquired on the waveguide chip-based microscope setup and the DV + 3D-SIM images acquired on the OMX microscope. In one hand, the TIRF image (Figure 3.30 (a)) exhibits high-contrast, with dark background regions close to the mitochondrial arrays (M), although it is likely that the entire sample thickness (i.e. 110 nm) was illuminated by the TIRF illumination from the waveguide-chip. On the other hand, the DV and 3D-SIM images ((Figure 3.30 (b) and Figure 3.30 (c), respectively) reveal structural information present in the same dark regions of TIRF. The structures appear unresolved in the DV image, compromising the image contrast and resolution of this technique, whereas the 3D-SIM image allows for visualization of cardiac muscle striations in these regions of the sample. A possible explanation for the appearance of such structures is that in DV and SIM modes, the chip served as a reflective surface that increased the effective excitation intensity, allowing for collection of additional fluorescent signal as compared to TIRF modality. In addition, it is also important to highlight that the TIRF image was acquired using a NA1.2 (water immersion) objective lens, whereas the DV image (and also SIM) used a NA1.42 (oil immersion) objective lens, therefore the resolution of the DV image was higher than that of the chip-based TIRF. Another reason for not imaging the cardiac muscle striations was that it might have been photo-bleached, as chip-based TIRF was performed in the last step, i.e. after acquiring SIM and DV images.

Interestingly, the TIRF image in Figure 3.30 (a) shows similar contrast view as the DV images of cryo-sections observed on the OMX using coverslips and glass slides as substrates (Figure 3.5 (c) and Figure 3.6 (c)). This observation indicates that the excitation intensity may play a role in the visualization of morphological details of cryo-sections. In fact, a closer look to Figure 3.19 (b) shows that the intensity of the evanescent field may be sufficient to image morphological structures such as the cardiac muscle striations.

This preliminary result points out that the chip-based TIRF microscopy can serve as a fast and affordable tool for routine histopathological studies. Recently, chip-based SRM has been proposed using single molecule localization microscopy [3] that open the opportunity for super-resolution imaging with high-throughput. Further studies are required to explore the feasibility of SRM imaging of tissue sections on the chip-based setup at higher imaging throughput than that of SIM technique on the OMX.

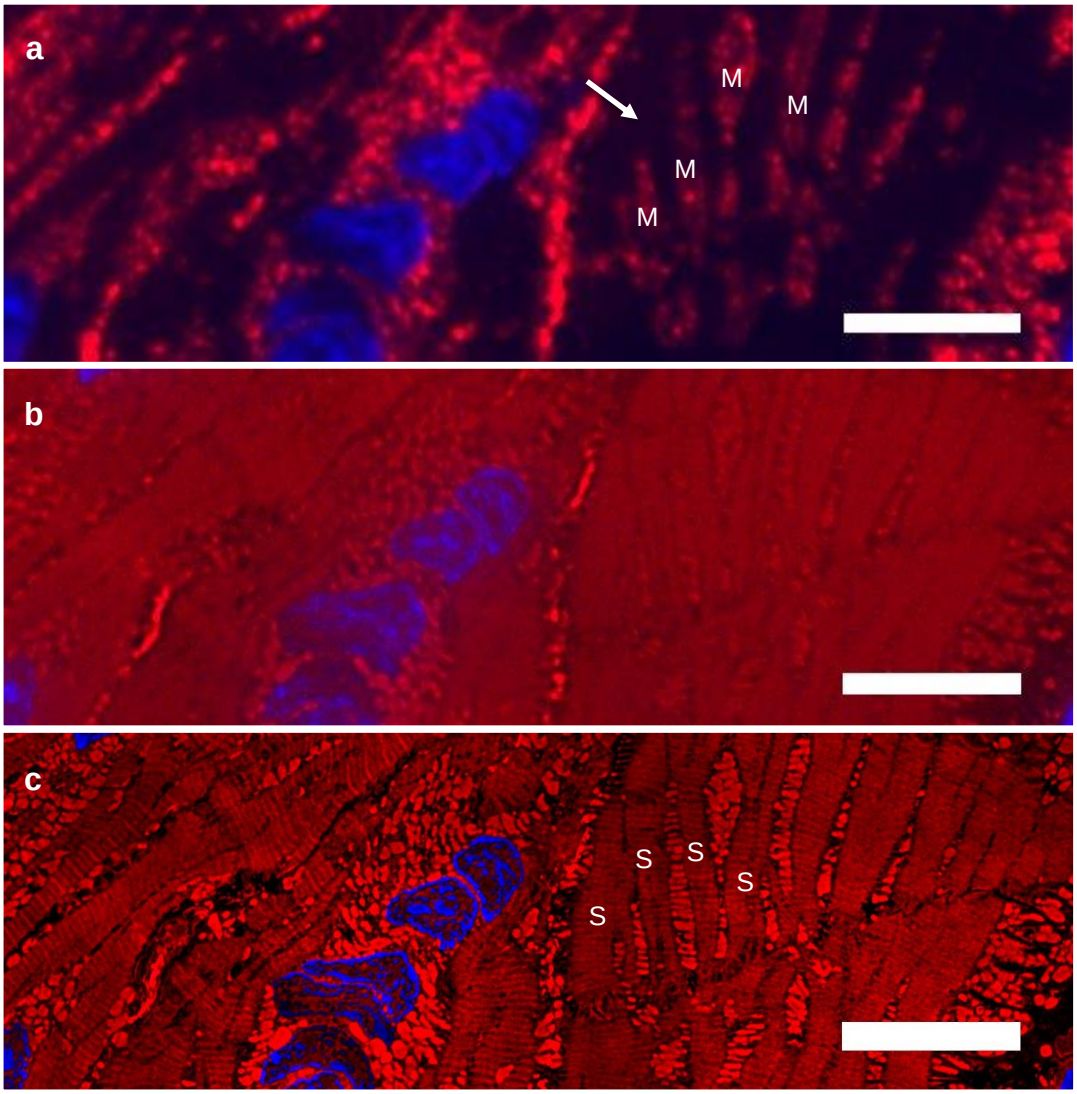

Figure 3.30. Comparison of TIRF, DV and 3D-SIM images of 100 nm thick pig heart cryo-section imaged on the waveguide chip-based microscope setup and the OMX microscope using a waveguide chip as a substrate. Membranes in red and nuclei in blue. White arrow indicates the space between the mitochondrial arrays (M). (a) TIRF image shows dark background around M. (b) DV image shows unresolved features around M. (c) 3D-SIM image reveals striations (S) around M.

Chapter 4. Conclusions and future work

This section summarizes the key findings associated with super-resolution imaging of tissue sections on the OMX and diffraction-limited TIRF imaging on the photonic chip-based microscopy setup. Relevant aspects of current and future work are also included as part of the conclusions of this master project study.

4.1 Conclusions

An extraordinary amount of information and knowledge has been gathered in the course of this master project. Perhaps the most important lesson from this study is that, indeed, it is possible to image tissue sections on both imaging platforms, the OMX and the waveguide chip-based microscopy setup. However, imaging tissue sections proved not to be an easy task. The scarcity of specialized literature in the field of super-resolution imaging of organ tissues (approx. 50 publications), posed several challenges towards sample preparation and imaging. For example, the transparency of ultrathin cryo-sections complicated the staining process, as they tended to detach from the coverslip during the washing steps, without noticing it. Gentle washing steps using absorbent paper to remove the incubation medium solved the problem, but additional difficulties were found upon observation on the microscope: cryo-sections tend to break and fold during sectioning process. This fact may not be relevant for other techniques that use ultrathin cryo-sections, such as electron microscopy, where a small FOV is required for observation of ultra-structural information in the cells, but it is of a significant importance in histological studies, where a large FOV is required to visualize morphological features of the tissues. Despite these two drawbacks, sample preparation protocols of cryo-sections were relatively easy and fast, allowing for imaging within the same day of sectioning. Cryo-sections exhibited excellent results in terms of staining specificity and imaging. SIM images of ultra-thin cryo-sections acquired in the first phase of the project proved the ability of this technique to resolve structures within 120 nm separation. In addition, SIM images exhibited better contrast than diffraction-limited DV images, which allowed for better contrast of cellular ultrastructures. Lastly, SIM suggested the possibility of generating three-dimensional animations from the z-stack of thick cryo-sections (>1000 nm).

Different knowledge was gained from FFPE tissue sections. To start with, sample preparation required far more iteration steps for optimization. Maybe the most challenging are the autofluorescence artifacts, observed both in diffraction-limited DV and super resolution SIM images. This is partially attributed to autofluorescent structures in the tissues, and partially to fixation-induced autofluorescence. A bleaching solution (glycine) was tested in the study but proved to be insufficient to reduce the autofluorescence signal from the samples. Contribution of autofluorescent signal resulted in imaging artifacts that hampered the imaging capabilities of the instrument, more prominently in the DV mode. Post-processing algorithm of SIM technique helped to reduce the autofluorescent signal, allowing for enhanced image contrast as compared to the DV images, but out-of-focus contribution of the sample led to reconstruction artifacts (e.g. haloing, honeycomb, hammerstroke) that limited the resolution capabilities of this technique. Hence, no sub-diffraction limit resolution was reported in this type of sample using the SIM mode. An autofluorescence characterization study of FFPE tissue sections revealed that great amount of autofluorescent signal came from red blood cells, with maximum emission response to 488 nm excitation source. On the positive side, FFPE samples well preserved their morphology after sectioning, allowing for large FOV imaging on the OMX and the chip. On the contrary, the possibility to acquire large FOV images on cryo-sections was sample-dependent, with usual limitations of 300 × 300 μm due to frequent structural damage and folds.

A common challenge encountered on both cryo-preserved and FFPE samples was oil matching. For optimal imaging results, the OMX requires refractive index matching between coverslip and objective lens. This task is normally achieved when the PSF of single emitters show symmetrical shape in the orthogonal views of DV z-stack images. Dyes used in this study complicated the visualization of single emitters, as they stained large amount of molecules present in the samples (e.g. membranes and nuclei). The problem was solved by an iterative oil immersion change process until symmetrical PSFs were obtained. In few FFPE samples the problem was solved by using fluorescent beads in the vicinity of the tissue sections at the last step of sample preparation. Beads were used as single emitters to perform oil matching. However, this method should be used with care, as the fluorescent signal of the beads could induce false positive results interpretation.

A tile-mosaic stitching technique was applied to obtain large FOV tissue section images on the OMX. In practice, the tissue samples were sequentially scanned in snake-like pattern, and the projected images were then computationally stitched in FIJI. Focus drift artifacts were observable on tile mosaic images of ultrathin cryo-sections mounted on microscope glass slides and coverslips. The chip proved to be an optimal substrate for these samples, having the advantages of providing: (a) an almost perfect surface flatness, and (b) a reflective surface that increased the effective intensity of the excitation source, allowing for additional collection of fluorescent signal as compared to transparent substrates. This was a highlight in the study. Using the chip as substrate for cryo-sections helped to visualize subcellular features in SIM images that were otherwise not observable on SIM images of samples laying on other substrates.

The experience and knowledge acquired on the first phase of the project was applied in the second phase. Sample preparation of FFPE and cryo-sections on chip was conducted in a similar way as for imaging on the OMX. Additional care was taken with the preparation of the chip, which required a thorough cleaning process and fine polishing of the input facet to ensure optimal excitation light coupling. Imaging tissue sections on the chip-based microscope setup also proved to be challenging. It was found out that, for uncladded chip topologies, light losses occur in a short distance (<10 mm) after the input facet, as a consequence of the light absorption by the sample and staining residues. The phenomenon was more prominent on FFPE samples than on cryo-sections. To overcome this problem, excitation power was increased, which led to moderate bleed-through effect on the edges of the waveguide. Diffraction-limited images acquired on this phase of the study proved, for first time, the feasibility of using the photonic chip as illumination platform for TIRF imaging of organ tissues.

Moreover, the correlative DV-TIRF study showed the benefit of using chip-based microscopy platform on tissues: it provides the possibility of de-coupling excitation and emission light paths, allowing for high-contrast TIRF imaging with low magnification/wide FOV objectives.

4.2 Future perspectives

Preliminary findings of this master project open the perspectives for direct application in studies that otherwise required the use of expensive electron microscopy which is time demanding and has low FOV throughput. Current studies using our imaging platform include SIM imaging of autophagosomes in cardiac tissue, cell-cell interactions and extracellular matrix deposition in healthy and diseased human liver, and marker expression for pre-eclamptic placenta diagnosis. Collaborations in the pipeline include the use of SIM in combination with machine learning algorithms for segmentation of histological features in routine pathology diagnosis.

Further optimization is required to reduce autofluorescence signal of FFPE tissue sections imaged on the OMX. In the meantime, it is advised not to include the 488 nm excitation source in the experimental plan for imaging of FFPE human liver and placental tissues, or if so, to be aware of the specificity limitations of imaging in this channel. Alternatively, autofluorescence or organ tissues could be exploited in SRM studies as proposed in recent works [47, 48]. Future experiments on FFPE samples may benefit of clearing techniques to reduce the out-of-focus contribution and allow sub-diffraction resolution of this type of samples in SIM.

The feasibility of diffraction-limited TIRF imaging of tissue sections on the chip indicates that super-resolution techniques can be employed in this platform. Current studies are also focused on obtaining data to use MUSICAL [23] algorithm as an SRM technique on chip, as well as including the *d*STORM technique. The use of cladded chip configurations will be explored to avoid light absorption at the coupling input of the chip and improve propagation of light inside the waveguide.

References

[1] S. Weisenburger and V. Sandoghdar, "Light microscopy: an ongoing contemporary revolution," *Contemporary Physics*, vol. 56, no. 2, pp. 123-143, 2015/04/03 2015.

[2] P. C. Montgomery and A. Leong-Hoi, "Emerging optical nanoscopy techniques," *Nanotechnology, science and applications*, vol. 8, p. 31, 2015.

[3] R. Diekmann *et al.*, "Chip-based wide field-of-view nanoscopy," *NATURE PHOTONICS*, vol. 11, no. 5, pp. 322–328, 2017.

[4] C. I. Øie *et al.*, "New ways of looking at very small holes–using optical nanoscopy to visualize liver sinusoidal endothelial cell fenestrations," *Nanophotonics*, vol. 7, no. 3, pp. 575-596, 2018.

[5] Ø. I. Helle, C. I. Øie, P. McCourt, and B. S. Ahluwalia, "Chip-based optical microscopy for imaging membrane sieve plates of liver scavenger cells," in *SPIE Nanoscience + Engineering*, 2015, vol. 9554, p. 5: SPIE.

[6] G. McNerney *et al.*, "Structured illumination microscopy applications towards liver sinusoidal endothelial cell fenestrations and HIV-1 cell-to-cell transmission," in *Communications and Photonics Conference and Exhibition (ACP), 2010 Asia*, 2010, pp. 373-374: IEEE.

[7] R. W. Cahn and E. M. Lifshitz, *Concise Encyclopedia of Materials Characterization*. Elsevier Science, 2016, p. 286.

[8] C. Huygens, *Treatise on Light*. CreateSpace Independent Publishing Platform, 2017.

[9] G. Stark, "Thin-film interference," ed: Encyclopaedia Britannica Inc., 2016.

[10] Rayleigh, "XXXI. Investigations in optics, with special reference to the spectroscope," *The London, Edinburgh, and Dublin Philosophical Magazine and Journal of Science*, vol. 8, no. 49, pp. 261-274, 1879/10/01 1879.

[11] E. Abbe, "Beiträge zur Theorie des Mikroskops und der mikroskopischen Wahrnehmung," *Archiv für mikroskopische Anatomie*, journal article vol. 9, no. 1, pp. 413-418, December 01 1873.

[12] M. Abramowitz and M. W. Davidson. (April 5, 2018). *Numerical Aperture and Resolution*. Available: https://www.olympus-lifescience.com/en/microscope-resource/primer/anatomy/numaperture/

[13] R. Hoffman and M. W. Davidson. (1995-2017, April 05, 2018). *Contrast in Optical Microscopy*. Available: https://micro.magnet.fsu.edu/primer/techniques/contrast.html

[14] "Liver," ed: National Taiwan University, College of Medicine.

[15] B. E. A. Saleh and M. C. Teich, *Fundamentals of Photonics*. Wiley, 2007.

[16] D. Lleres, S. Swift , and A. I. Lamond, "Detecting Protein-Protein Interactions In Vivo with FRET using Multiphoton Fluorescence Lifetime Imaging Microscopy (FLIM)," *Current Protocols in Cytometry*, 2007.

[17] Regaladys. (2010, April 18). *Properties of the 2D Fourier Transform*. Available: https://regaladys.wordpress.com/2010/09/23/7-properties-of-the-2d-fourier-transform/

[18] B.-J. Chang, L.-J. Chou, Y.-C. Chang, and S.-Y. Chiang, "Isotropic image in structured illumination microscopy patterned with a spatial light modulator," *Optics Express*, vol. 17, no. 17, pp. 14710-14721, 2009/08/17 2009.

[19] andor.com. (April 08). *Super-Resolution Imaging - Structured Illumination Microscopy*. Available: http://www.andor.com/learning-academy/super-resolution-imaging-structured-illumination-microscopy-application-note

[20] A. Stemmer, M. Beck, and R. Fiolka, "Widefield fluorescence microscopy with extended resolution," *Histochem Cell Biol*, no. 130, pp. 807–817, 2008.

[21] I. Simphotek. (2010-2015, April 09). *SimphoSOFT*. Available: http://simphotek.net/appnote-STED.html

[22] N. University. (2007-2011, April 09). *Single Molecule Localization Microscopy*. Available: https://cam.facilities.northwestern.edu/588-2/single-molecule-localization-microscopy/

[23] K. Agarwal and R. Macháň, "Multiple signal classification algorithm for super-resolution fluorescence microscopy," *Nature Communications*, vol. 7, p. 13752, 2016.

[24] J.-C. Tinguely, Ø. I. Helle, and B. S. Ahluwalia, "Silicon nitride waveguide platform for fluorescence microscopy of living cells," *Optics Express*, vol. 25, no. 22, pp. 27678-27690, 2017/10/30 2017.

[25] I. Arganda‐Carreras, R. Fernández‐González, A. Muñoz‐Barrutia, and C. Ortiz‐De‐Solorzano, "3D reconstruction of histological sections: application to mammary gland tissue," *Microscopy research and technique*, vol. 73, no. 11, pp. 1019-1029, 2010.

[26] P. Education, "Animal cell," ed: Benjamin Cummings, 2003.

[27] R. Milo and R. Phillips, *Cell Biology by the Numbers*. Taylor & Francis Group, 2015.

[28] T. E. o. E. Britannica. (2017, April 04, 2018). *Human body*. Available: https://www.britannica.com/science/human-body

[29] W. K. Purves, D. Sadava, G. H. Orians, and H. C. Heller, *Life: the science of biology*, 7th ed. W. H. Freeman & Co, 2004.

[30] T. C. Schlichenmeyer, M. Wang, K. N. Elfer, and J. Q. Brown, "Video-rate structured illumination microscopy for high-throughput imaging of large tissue areas," *Biomedical Optics Express*, vol. 5, no. 2, pp. 366-377, 2014.

[31] D. A. Coucheron, Ø. I. Helle, C. I. Øie, F. T. Dullo, and B. S. Ahluwalia, "Chip-based nanoscopy: towards integration and high-throughput imaging," in *SPIE Nanoscience + Engineering*, 2017, vol. 10350, p. 7: SPIE.

[32] M. Oheim, "High-throughput microscopy must re-invent the microscope rather than speed up its functions," *British Journal of Pharmacology*, vol. 152, no. 1, pp. 1-4, 2007.

[33] H. L. Fu *et al.*, "Optimization of a Widefield Structured Illumination Microscope for Non-Destructive Assessment and Quantification of Nuclear Features in Tumor Margins of a Primary Mouse Model of Sarcoma," *PLoS ONE*, vol. 8, no. 7, p. e68868, 2013.

[34] M. Wang *et al.*, "High-resolution rapid diagnostic imaging of whole prostate biopsies using video-rate fluorescence structured illumination microscopy," *Cancer research*, vol. 75, no. 19, pp. 4032-4041, 08/17 2015.

[35] T. Taylor. (2012, April 03). *Liver*. Available: http://www.innerbody.com/image_digeov/card10-new2.html

[36] M. Gordillo, T. Evans, and V. Gouon-Evans, "Orchestrating liver development," *Development*, vol. 142, pp. 2094-2108, 2015-06-15 00:00:00 2015.

[37] V. B Zeldovich, J. Robbins, M. Kapidzic, P. Lauer, and A. Bakardjiev, *Invasive Extravillous Trophoblasts Restrict Intracellular Growth and Spread of Listeria monocytogenes*. 2011, p. e1002005.

[38] M. F. Oliver, M. L. Entman, S. W. Jacob, and T. E. o. E. Britannica. (2017, April 04, 2018). *Human cardiovascular system*. Available: https://www.britannica.com/science/human-cardiovascular-system/Wall-of-the-heart

[39] G. Rolls. (April 13). *An Introduction to Specimen Preparation*. Available: https://www.leicabiosystems.com/pathologyleaders/an-introduction-to-specimen-preparation/

[40] M. K. Creech, J. Wang, X. Nan, and S. L. Gibbs, "Superresolution Imaging of Clinical Formalin Fixed Paraffin Embedded Breast Cancer with Single Molecule Localization Microscopy," *Scientific Reports*, Article vol. 7, p. 40766, 01/18/online 2017.

[41] U. Schnell, F. Dijk, K. A. Sjollema, and B. N. Giepmans, "Immunolabeling artifacts and the need for live-cell imaging," *Nature methods*, vol. 9, no. 2, p. 152, 2012.

[42] Abcam. (1998-2018, April 07). *Direct vs indirect immunofluorescence*. Available: http://www.abcam.com/secondary-antibodies/direct-vs-indirect-immunofluorescence

[43] E. C. Jensen, "Use of fluorescent probes: their effect on cell biology and limitations," *The Anatomical Record*, vol. 295, no. 12, pp. 2031-2036, 2012.

[44] Abcam. (1998-2018, April 15). *IHC antigen retrieval protocol*. Available: http://www.abcam.com/protocols/ihc-antigen-retrieval-protocol

[45] N. Diagnostics. (2011, April 18). *Mounting Tissue Sections*. Available: https://www.nationaldiagnostics.com/histology/article/mounting-tissue-sections

[46] R. D. Systems. (2018, April 15). *Protocol for the Preparation and Fluorescent IHC Staining of Frozen Tissue Sections*. Available: https://www.rndsystems.com/resources/protocols/protocol-preparation-and-fluorescent-ihc-staining-frozen-tissue-sections

[47] G. Best *et al.*, "Structured illumination microscopy of autofluorescent aggregations in human tissue," *Micron*, vol. 42, no. 4, pp. 330-335, 2011.

[48] S. Rossberger, T. Ach, G. Best, C. Cremer, R. Heintzmann, and S. Dithmar, "High-resolution imaging of autofluorescent particles within drusen using structured illumination microscopy," *British Journal of Ophthalmology*, vol. 97, no. 4, pp. 518-523, 2013.

[49] J. M. Pullman, J. Nylk, E. C. Campbell, F. J. Gunn-Moore, M. B. Prystowsky, and K. Dholakia, "Visualization of podocyte substructure with structured illumination microscopy (SIM): a new approach to nephrotic disease," *Biomedical Optics Express*, vol. 7, no. 2, pp. 302-311, 2016.

[50] F. Siegerist *et al.*, "Structured illumination microscopy and automatized image processing as a rapid diagnostic tool for podocyte effacement," *Scientific reports*, vol. 7, no. 1, p. 11473, 2017.

[51] J. Kuo, *Electron Microscopy: Methods and Protocols*. Humana Press, 2016.

[52] C. I. Øie, I. Snapkov, K. Elvevold, B. Sveinbjørnsson, and B. Smedsrød, "FITC Conjugation Markedly Enhances Hepatic Clearance of N-Formyl Peptides," *PLOS ONE*, vol. 11, no. 8, p. e0160602, 2016.

[53] J. B. Sibarita, "Deconvolution microscopy," (in eng), *Adv Biochem Eng Biotechnol*, vol. 95, pp. 201-43, 2005.

[54] J. Demmerle *et al.*, "Strategic and practical guidelines for successful structured illumination microscopy," *nature protocols*, vol. 12, no. 5, p. 988, 2017.

[55] É. P. F. D. Lausanne. (2017, April 24). *3D Deconvolution Microscopy*. Available: http://bigwww.epfl.ch/deconvolution/bars/

[56] J. Schindelin *et al.*, "Fiji: an open-source platform for biological-image analysis," *Nat Meth*, 10.1038/nmeth.2019 vol. 9, no. 7, pp. 676-682, 07//print 2012.

[57] S. Preibisch, S. Saalfeld, and P. Tomancak, "Globally optimal stitching of tiled 3D microscopic image acquisitions," *Bioinformatics*, vol. 25, no. 11, pp. 1463-1465, 2009.

[58] J. M. Mateos, B. Guhl, J. Doehner, G. Barmettler, A. Kaech, and U. Ziegler, "Topographic contrast of ultrathin cryo-sections for correlative super-resolution light and electron microscopy," *Scientific Reports*, Article vol. 6, p. 34062, 09/26/online 2016.

[59] M. Neumann and D. Gabel, "Simple Method for Reduction of Autofluorescence in Fluorescence Microscopy," *Journal of Histochemistry & Cytochemistry*, vol. 50, no. 3, pp. 437-439, 2002.

[60] N. Raghavachari, Y. P. Bao, G. Li, X. Xie, and U. R. Müller, "Reduction of autofluorescence on DNA microarrays and slide surfaces by treatment with sodium borohydride," *Analytical biochemistry*, vol. 312, no. 2, pp. 101-105, 2003.

[61] A. S. Davis *et al.*, "Characterizing and diminishing autofluorescence in formalin-fixed paraffin-embedded human respiratory tissue," *Journal of Histochemistry & Cytochemistry*, vol. 62, no. 6, pp. 405-423, 2014.

[62] J. Kiernan and M. Wessendorf, "Autofluorescence: Causes and cures," *Toronto Western Research Institute,[DirectLink]*, 2001.

[63] N. C. Whittington and S. Wray, "Suppression of Red Blood Cell Autofluorescence for Immunocytochemistry on Fixed Embryonic Mouse Tissue," *Current protocols in neuroscience*, vol. 81, no. 1, pp. 2.28. 1-2.28. 12, 2017.

[64] B. Gopalkrishnapillai, V. Nadanathangam, N. Karmakar, S. Anand, and A. Misra, "Evaluation of autofluorescent property of hemoglobin-advanced glycation end product as a long-term glycemic index of diabetes," *Diabetes*, vol. 52, no. 4, pp. 1041-1046, 2003.

[65] G. Ball, J. Demmerle, R. Kaufmann, I. Davis, I. M. Dobbie, and L. Schermelleh, "SIMcheck: a Toolbox for Successful Super-resolution Structured Illumination Microscopy," *Scientific Reports*, Article vol. 5, p. 15915, 11/03/online 2015.

Appendix A. General protocol for fluorescent staining on FFPE tissue sections

Samples:
Semi thin sections (4µm-5µm) of Formalin Fixed Paraffin Embedded (FFPE) tissue.

Substrate:
#1.5 cover slips (VWR, cat# 48393-151 or equivalent) - or photonics chip- coated with poly-L-lysine solution (Sigma-Aldrich, cat# 25988-63-0)

Handling tips:
When working on samples laying directly on the cover slips, it is convenient to place them in a cover slip rack, staining jar or similar, during the deparaffinization steps, and manipulate them with wide tip tweezers.

Reagents (fill in the information according to the experiment plan)

Primary antibody:

No	Name	Company	Cat no	Lot no	Stock concentration	Location

Secondary antibody:

No	Name	Company	Cat no	Lot no	Stock concentration	Location

Antibody working solutions:

Primary Abs	Stock Conc.	Dilution	Volume µl - total
Secondary Abs			

Available excitation wavelengths for fluorescence imaging on the OMX:
642 nm / 568 nm / 488 nm / 405 nm

Washing buffer TBST: TBS*+0.05% Tween 20 (pH 8.4) (2.5 ml 20% Tween 20 in 1L TBS)

TBS*:

10X **TBS** (0.5M Tris base, 9% 1.54M NaCl-pH8.4)
Trizma base, 61 g + NaCl, 90 g + Milli-Q water up to 1000 mL
Adjust pH to 8.4 using concentrated HCl

Blocking / Dilution buffer: **1% BSA in TBST** (1g BSA in 100 ml TBST).

Citrate buffer (pH 5.98):

Solution A: 10.5 g citric acid monohydrate in 500 ml Milli-Q water

Solution B: 29.4 sodium citrate in 1L Milli-Q water

Mix 18 ml solution A and 82 ml solution B, make up to 1L with Milli-Q water

Bleaching solution:

150 mM Glycine solution (Sigma-Aldrich, cat# G7126)

Procedure:

Do not let the samples dry out at any point of the protocol.

Deparaffinization and rehydration (change all the solutions every 2 weeks, fill up in between). After sectioning, leave the sections in 60°C overnight, then proceed with the following steps:

3 x 5 min: Xylene

2 x 10 min: 100 % Ethanol

2 x 10 min: 96% Ethanol

1 x 10 min: 70% Ethanol

1 x 30 min Bleaching solution

3 x 5 min: Milli-Q water

Antigen retrieval

Pre-warm citrate buffer to around 95°C, and place sections in beaker filled with hot buffer.

Microwave 2 x 5 min @50% power. Fill up with hot buffer in between if the level gets low.

Let sections cool down in the buffer for 20 min at RT.

Washing and blocking steps

wash sections 3 x 2 min with Milli-Q water and aspirate excess liquid from slides.

wash in TBST for 2 min

incubate in blocking buffer for 30 min at RT

Labeling with primary antibodies

Spin down all antibodies and dilute them in blocking buffer according to the recommended concentration. Make up to 100 - 150 µl / coverslip, depending on the size of the tissue section.

Place the slides in a wet chamber (e.g. petri dish with a moisturized paper or equivalent) and incubate the antibodies on slides according to the recommended incubation time (e.g. overnight incubation at 4°C).

Labeling with secondary antibodies

All steps from now on will be done under aluminum foil, to prevent photobleaching

Dilute secondary antibodies in blocking buffer according to the recommended concentration and incubate on slides for 1h at RT

Wash 3 x 5 min in TBST

Wash 2 x 5 min in PBS

Cell membrane staining (optional step)

Dilute Cell Mask Orange (ThermoFischer, cat # C10045) in PBS (1:2000) and incubate on slides for 10min.

Wash 2 x 5 min in PBS

Nuclear staining and mounting

Add nuclear staining on cover slips and incubate at RT for 5 min

Wash 2 x 5min in Milli-Q water

Aspirate excess liquid from sections, but not let them dry.

Mounting samples on coverslip

Apply mounting medium Prolong Gold (ThermoFisher, cat #P36930) in the center of the glass slide (see Figure A.1), and place the sample facing the mounting medium. Remove excess mounting medium with an absorbent paper. Remove visible air bubbles from sample by gently tapping the coverslip with a plastic tweezer.

Let the mounting medium to harden (approx. 30 min) and seal with nail polish.

Store the sample at 4°C and protect it from the light.

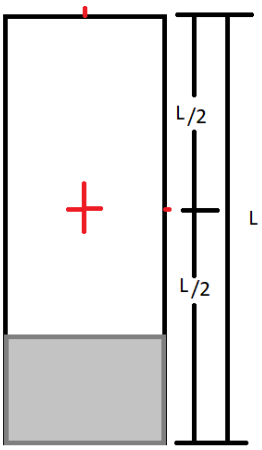

Figure A.1. Marking on microscope slide for positioning of coverslip with sample.

Mounting samples on chip

Apply PBS on top of the sample and cover with a #1.5 cover slip. Remove excess PBS with an absorbent paper. Remove visible air bubbles from sample by gently tapping the coverslip with a plastic tweezer.

Seal corners with picodent twinsil 22 (Picodent, cat# 1300 1000). See Figure A.2.

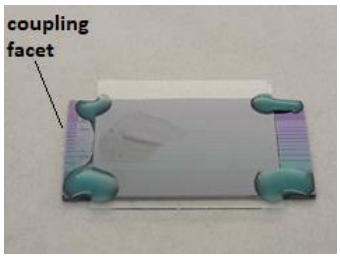

Figure A.2. Sealing with picodent.

Place the chip onto the center of a microscope slide and glue edges with picodent. See Figure A.3.

Figure A.3. Transferring chip to center of microscope slide.

Align the coupling facet of the chip with the edge of the microscope slide. Gently place a small weight (approx. 200 g) on top of the coverslip and let the picodent cure (15 min). See Figure A.4.

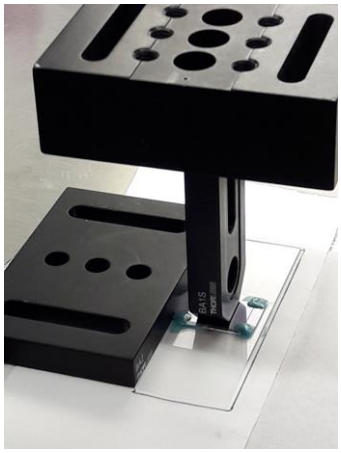

Figure A.4. Weight and alignment.

Store the sample at 4°C and protect it from the light.

Appendix B. General protocol for fluorescent staining on cryo-sections

Samples:

Ultra-thin cryo-sections (70 nm - 1000 nm) of cryo-preserved tissue, sectioned with ultra-microtome per Tokuyasu method.

Substrate:

#1.5 cover slips (VWR cat# 48393-151 or equivalent)- or photonics chip- coated with poly-L-lysine solution (SIGMA-ALDRICH cat# 25988-63-0)

Handling tips:

When working on samples laying directly on cover slips, it is convenient to manipulate them with wide tip tweezers, to avoid breaks.

Keep the samples in a cold environment (approx. 4°C) during preparation steps. It is recommended to use an ice bucket for transportation and further staining of the samples. See Figure B.1.

Figure B.1. Transportation and handling of cryo-sections.

Reagents (fill in the information according to the experiment plan)

Primary antibody:

No	Name	Company	Cat no	Lot no	Stock concentration	Location

Secondary antibody:

No	Name	Company	Cat no	Lot no	Stock concentration	Location

Antibody working solutions:

Primary Abs	Stock Conc.	Dilution	Volume µl - total
Secondary Abs			

Available excitation wavelengths for fluorescence imaging on the OMX:

642 nm / 568 nm / 488 nm / 405 nm

Imaging buffer for chip-based microscopy:

Mix 20µl of pre-made glucose stock (GS) with 2,5µl pre-made enzyme stock (ES) and 12,5µl glycerol in 12,5µl PBS.

Procedure:

Do not let the samples dry out at any point of the protocol.

Washing out the methyl cellulose:

Wash sections 3 x 7 min with PBS. Gently remove excess liquid from the coverslip with absorbent paper (see Figure B.1). Keep the samples at 4°C.

Fixation (optional step to follow in case the sample wasn't fixed before):

Fix the sample according to the recommended protocol (i.e. 4% PFA for 10 min)

Wash sections 3 x 7 min with PBS. Gently remove excess liquid from the coverslip with absorbent paper.

Blocking:

Incubate the samples in 1% BSA in PBS for 30min.

Wash 2 x 5 min in PBS. Gently remove excess liquid from the coverslip with absorbent paper.

Labeling with primary antibodies

Spin down all antibodies and dilute them in BSA/PBS according to the recommended concentration. Prepare a working solution of 100µl/coverslip, depending on the size of the tissue section.

Place the slides in a wet chamber (e.g. petri dish with a moisturized paper or equivalent) and incubate the antibodies on slides according to the recommended incubation time (e.g. overnight incubation at 4°C).

Labeling with secondary antibodies

Wash 2 x 5 min in PBS. Gently remove excess liquid from the coverslip with absorbent paper.

All steps from now on will be done under aluminum foil, to prevent photobleaching

Dilute secondary antibodies in BSA/PBS according to the recommended concentration and incubate for the appropriate time according to the labeling protocol.

Cell membrane staining (optional step)

Wash sections 3 x 7 min with PBS. Gently remove excess liquid from the coverslip with absorbent paper.

Dilute Cell Mask Orange (ThermoFischer, cat # C10045) in PBS (1:2000) and incubate on slides for 10min. Prepare a solution of 100µl/coverslip.

Incubate the samples 10min, protected from light.

Nuclear staining and mounting

Wash 2 x 5 min in PBS. Gently remove excess liquid from the coverslip with absorbent paper.

Add nuclear staining on cover slips and incubate at RT for 5 min

Wash 2 x 5min in Milli-Q water

Mounting samples on coverslip

Apply mounting medium Prolong Gold (ThermoFisher, cat #P36930) in the center of the glass slide (see Figure B.2), and place the sample facing the mounting medium. Remove excess mounting medium with an absorbent paper. Remove visible air bubbles from sample by gently tapping the coverslip with a plastic tweezer.

Let the mounting medium to harden (approx. 30 min) and seal with nail polish.

Store the sample at 4°C and protect it from the light.

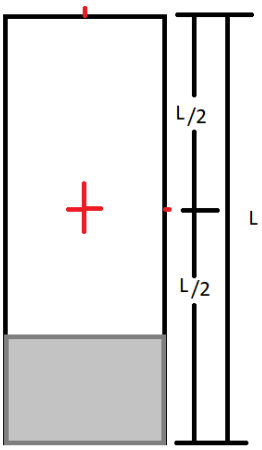

Figure B.2. Marking on microscope slide for positioning of coverslip with sample.

Mounting samples on chip

Add the imaging buffer on top of the sample. Cover with a #1.5 cover slip and remove excess with an absorbent paper. Remove visible air bubbles from sample by gently tapping the coverslip with a plastic tweezer.

Seal corners with picodent twinsil 22 (Picodent, cat# 1300 1000). Figure B.3.

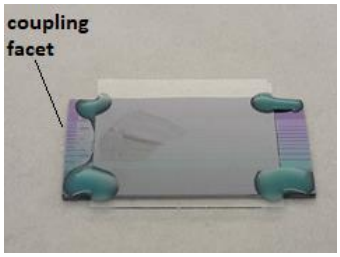

Figure B.3. Sealing with picodent.

Place the chip onto the center of a microscope slide and glue edges with picodent. See Figure B.4.

Figure B.4. Transferring chip to center of microscope slide.

Align the coupling facet of the chip with the edge of the microscope slide. Gently place a small weight (approx. 200 g) on top of the coverslip and let the picodent cure (15 min). See Figure B.5.

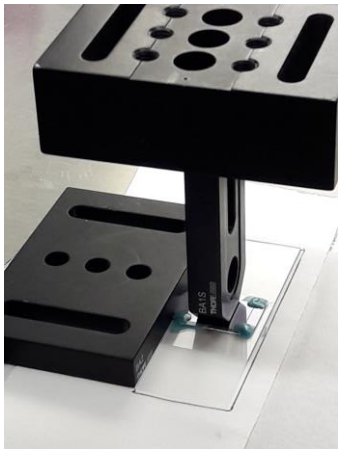

Figure B.5. Weight and alignment.

Store the sample at 4°C and protect it from the light.

Appendix C. SIM artifacts

The super-resolution capabilities of SIM are heavily dependent on computational post-processing of the collected images. Variations of acquisition of parameters such as refractive index, excitation intensity, exposure time, dye photo-stability, instrument calibration and temperature, among others, can introduce diverse reconstruction artifacts that might lead to misinterpretation of the image information and compromise the reliability of the experiments. The following subsections illustrate the most common SIM artifacts on tissue sections imaged with the OMX microscope.

Haloing

Perhaps the most common SIM artifact, the *haloing* consists of pseudo-structures with halo shape surrounding the real structures of the sample. This is due to the refractive index mismatch between the immersion oil and the coverslip on which the sample is imaged. This artifact can be removed by matching the refractive index of the immersion oil to that of the coverslip, by means of obtaining symmetrical PSF on the orthogonal views of single emitters on DV images. Thick tissue samples pose a challenge for this task, since no single emitters are normally found for PSF optimization. One way to overcome this challenge is by adding fluorescent beads near the tissue section during sample preparation and use them later as single emitters for oil matching. Figure 4.1 illustrates the haloing artifact.

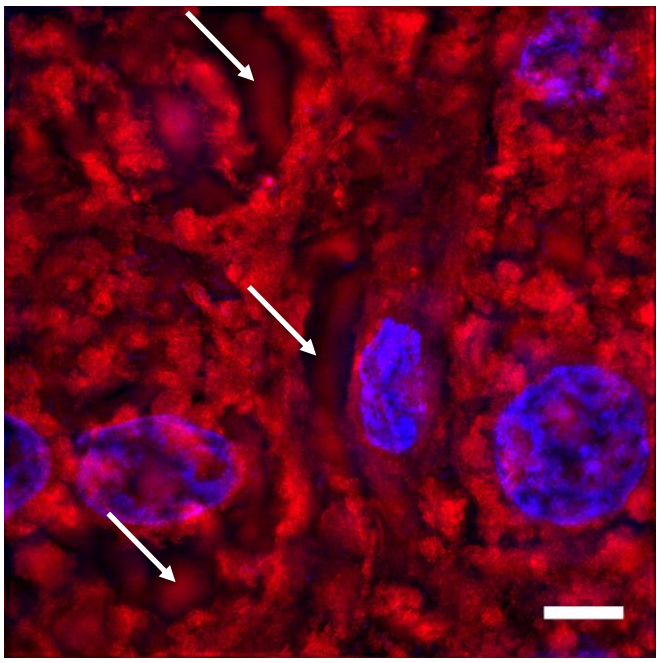

Figure 4.1. Haloing artifact on a 3D-SIM image. 3D-SIM image of human liver FFPE-section, 4 μm thick. Membranes (labeled with CMO) in red, nuclei (labeled with DAPI) in blue. White arrows show haloing artifacts on the image. Scale bar 5 μm.

Honeycomb

A common reconstruction artifact in SIM is the *honeycomb* artifact, which originates from low signal-to-noise ratio through the image acquisition, and produces pseudo-structures of hexagonal shape, analogous to a honeycomb structure.

Reconstructed SIM images of FFPE tissues imaged on the OMX exhibited honeycomb artifacts, consequence of increased out-of-focus signal present in thick sections. Possible ways to mitigate this artifact is by using TIRF illumination, thinner tissue sections or clearing agents such as VISIKOL®, to reduce the out-of-focus contribution in the reconstructed image. Figure 4.2 illustrates the honeycomb artifact.

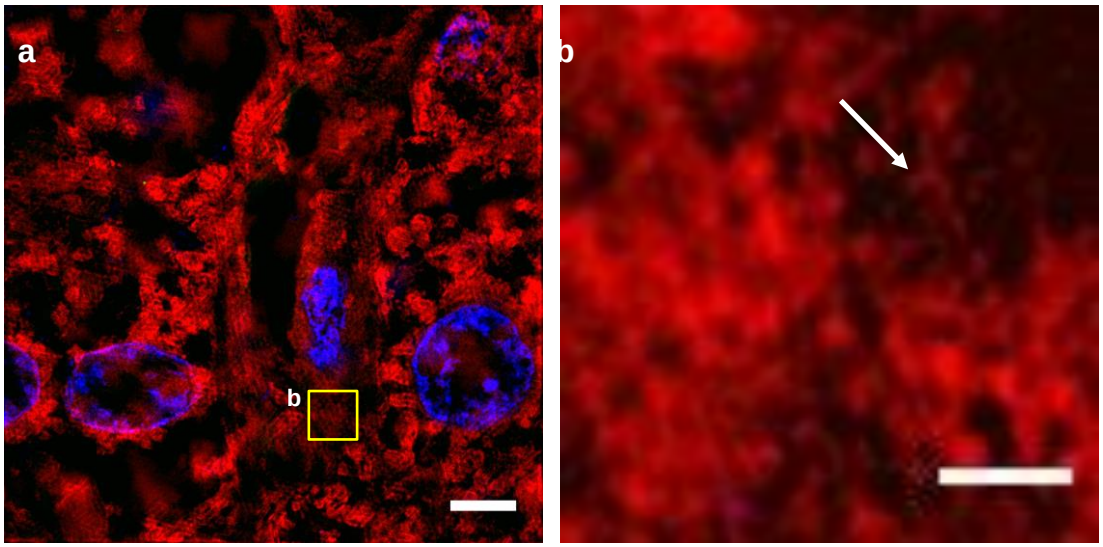

Figure 4.2. Honeycomb artifact on a SIM image. Human liver FFPE-section, 4 μm thick. Membranes (labeled with CMO) in red, nuclei (labeled with DAPI) in blue. (a) SIM image. (b) White arrow shows honeycomb pseudo-structures on the image. Scale bar (a) 5 μm, (b) 1 μm.

Hatching

A common reconstruction artifact in SIM is called *hatching*, which consists of striped extensions in one or more directions along the reconstructed image. This artifact is present when the parameters of the illumination pattern become offset in one or more of the projected angles through the image acquisition. An adequate equipment calibration and diagnose software (e.g. SIMcheck) can help to eliminate this artifact [65]. Figure 4.3 illustrates the hatching artifact.

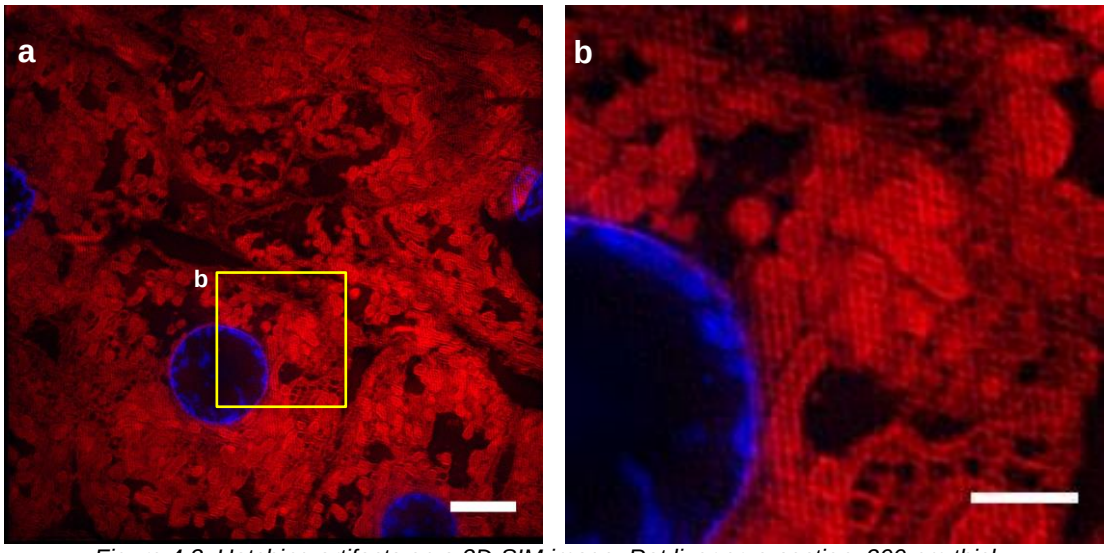

Figure 4.3. Hatching artifacts on a 3D-SIM image. Rat liver cryo-section, 300 nm thick. Membranes (labeled with CMO) in red, nuclei (labeled with DAPI) in blue. (a) 3D-SIM image. (b). Magnified view shows stripe pattern characteristic of hatching artifact. Scale bar (a) 5 μm, (b) 2 μm.

High-frequency noise (hammerstroke)

This artifact refers to pseudo-structures that appear in the reconstructed SIM images, which can be misinterpreted as biological features. This occurs when reconstructed background signal mixes up with poorly resolved structures in the sample, in regions with low signal-to-noise ratio. Specialized software (e.g. SIMcheck) can be used to identify areas of the image with this artifact. An optimal way to minimize it is by adjusting the parameters of the high-frequency noise filter (e.g. Wiener filter) included in the imaging software of the super-resolution microscope. Figure 4.3 illustrates the hammerstroke artifact.

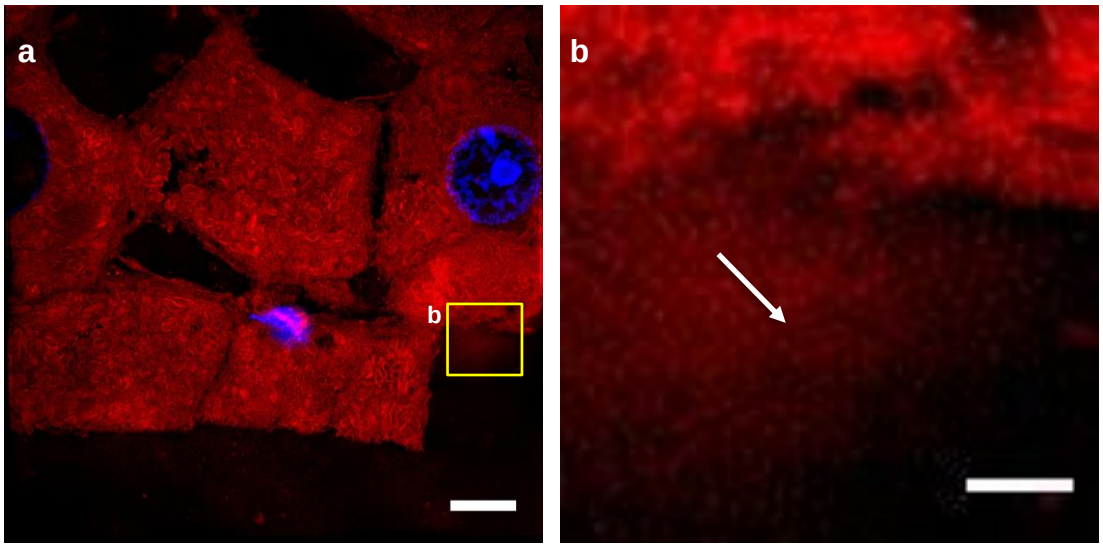

Figure 4.4. High-frequency noise 'hammerstroke' artifact on a 3D-SIM image. Rat liver cryo-section, 1000 nm thick. Membranes (labeled with CMO) in red, nuclei (labeled with DAPI) in blue. (a) 3D-SIM image. (b) White arrow shows pseudo-structures on the image, characteristic of hammerstroke artifact. Scale bar (a) 5 μm, (b) 1 μm.

Appendix D. List of publications

- **Poster in the Norwegian Electro-Optics Meeting, May 2018, Norway**
  Structured Illumination Microscopy of Biological Structures
  Deanna L. Wolfson, Luis Villegas, Ida S. Opstad, Åsa B. Birgisdottir, Cristina I. Øie, Balpreet S. Ahluwalia

- **Poster in the International Symposium on Experimental & Clinical Cardiovascular Medicine, May 2018, Greece**
  Monitoring autophagy in the pig heart during ischemia and reperfusion
  Åsa B. Birgisdottir, Trine B. Kalstad, Luis Villegas, Kenneth B. Larsen, Randi Olsen, Anders B. Kildal1, Balpreet Singh Ahluwalia, Terje Johansen and Truls Myrmel.

- **Poster in SPIE Optics + Photonics, August 2018, USA**
  High-speed, high resolution, multi-color imaging of living cells and tissues using MUSICAL
  Krishna Agarwal, Luis Villegas, Ida Sundvor Opstad, Mona Nystad, Åsa Birna Birgisdottir, Trine Karstad, Truls Myrmel, Cristina I. Øie, and Balpreet Singh Ahluwalia

Manuscripts in preparation

Two journal papers are currently under preparation on the following areas:

- **Imaging of tissues using optical waveguide platform.**
- **Tissue imaging using OMX.**

Appendix E. 3D animations

The following web link provides a 3D animation of a 1000 nm thick rat liver cryosection imaged on the OMX in SIM mode. The animation was created in FIJI from a z-stack containing 21 z-sections of the sample, imaged at incremental steps o 125 nm in the axial direction. Membranes in red, LSEC in green, nuclei in blue.

https://drive.google.com/file/d/1Ht6QhwYGtl15InB1Z5nlnygUYS-wEEhj/view?usp=sharing